Università
degli Studi
di Padova

Department of Industrial Engineering DII

Master of Science in Aerospace Engineering

A numerical study on the Shock Wave Boundary Layer Interaction

Candidate:
Ludovico Soldati

Thesis advisor:
prof. **Francesco Picano**

Thesis co-advisor:
eng. **Francesco de Vanna**

Academic Year 2019/2020

to my family
to my friends
to all my loved ones

Don't settle for mediocrity.
Long for great things,
not small things.

Sommario

In questa tesi viene affrontato lo studio della dinamica dell'interazione fra un'onda d'urto obliqua e lo strato limite di un flusso laminare che riveste una piastra investita da esso.
Lo studio è motivato dalla carenza di dati accurati in tale ambito, sia sperimentali che numerici, e dal fornire un punto di partenza per ulteriori studi maggiormente approfonditi nel regime turbolento.
La tesi inizia con un quadro generale del fenomeno, per poi descrivere le varie parti che compongono la simulazione volta a studiarlo, dopodichè viene presentata la sua validazione e infine si presentano varie analisi sull'interazione sia per diversi numeri di Mach fissato l'angolo del generatore dell'onda d'urto obliqua, sia fissando l'angolo dell'onda d'urto obliqua e variando il numero di Mach. In particolare si osserva l'andamento della pressione a parete, l'andamento del coefficiente d'attrito il quale è direttamente collegato allo sforzo di taglio viscoso, si osserva la dinamica del reflusso nello strato limite e infine si studia il comportamento termico associato al fenomeno.
Ciò che si nota dallo studio è che all'interno della zona di interazione si hanno due compressioni successive combinate ad un effetto dissipativo indotto dalla viscosità tanto maggiore quanto più alto è il numero di Mach. Contemporaneamente all'aumentare del numero di Mach si riduce l'intensità dell'onda d'urto, e con essa l'entità del fenomeno di ricircolo che prende atto nello strato limite, il che si traduce in una riduzione delle dimensioni della regione di distacco dello strato limite. Parallelamente si nota un aumento dello scambio termico verso l'esterno a parete prevalentemente in corrispondenza dei due gradienti avversi di pressione, il che significa un corrispondente aumento di temperatura del flusso seguendo lo stesso pattern. Localmente però si nota una leggera riduzione forzata della temperatura (non causata dallo scambio termico a parete bensì dal fenomeno di interazione stesso) nella regione dell'interazione compresa fra i due gradienti di pressione. Pertanto si ha un raffreddamento del flusso, inframezzato a due fenomeni di riscaldamento dello stesso.
Inoltre fissando l'angolo dell'onda d'urto e aumentando il numero di Mach si nota una crescente intensità dell'interazione che aumenta le dimensioni della bolla di ricircolo e l'entità del reflusso.

Abstract

This thesis deals with the study of the dynamics of the interaction between an oblique shock wave and the boundary layer of a laminar flow that covers a plate hit by it.
The study is motivated by the lack of accurate data in this area, both experimental and numerical, and by providing a starting point for further studies, more detailed, in the turbulent regime.
The thesis begins with a general picture of the phenomenon, then the various parts that make up the simulation aimed at studying it get described, after that its validation is presented and finally various analysis are carried out on the interaction both for different Mach numbers having fixed the oblique shock wave generator and by fixing the shock wave angle and varying the Mach number. In particular, the trend of the wall pressure is observed, the trend of the friction coefficient which is directly connected to the viscous shear stress, then the dynamics of the reflux in the boundary layer and finally the thermal behavior associated with the phenomenon get studied.
What can be seen from the study is that within the interaction zone there are two successive compressions combined with a dissipative effect induced by viscosity, the greater the higher the Mach number. Simultaneously with the increase in the Mach number, the intensity of the shock wave decreases, and with it the extent of the recirculation phenomenon that takes place in the boundary layer, which is translated into a reduction in the size of the detachment region of the boundary layer. In parallel, there is an increase in the heat exchange towards the outside on the wall mainly in correspondence of the two adverse pressure gradients, which means a corresponding increase in the temperature of the flow following the same pattern. Locally, however, there is a slight forced reduction in temperature (not caused by the heat exchange on the wall but by the phenomenon of interaction itself) in the region of the interaction between the two pressure gradients. Therefore there is a cooling of the flow, interspersed with two heating phenomena of the same.
Furthermore, fixing the shock wave angle and increasing the Mach number, the intensity of the interaction is observed to grow up leading to an increment of the recirculating bubble dimensions and of the reflux entity.

Nomenclature

Acronyms

[CSW] Crossing Shock Wave

[DSW] Downstream the Shock Wave

[ENO] Essentially Non-Oscillatory

[IBMs] Immersed Boundary Methods

[LODI] Local One Dimensional Inviscid

[NSCBC] Navier Stokes Characteristic Boundary Conditions

[SWBLI] Shock Wave Boundary Layer Interaction

[WENO] Weighted Essentially Non-Oscillatory

Variables

β	Oblique shock wave angle	$[^\circ]$
δ	Boundary layer thickness	$[m]$
$\delta_{i,j}$	Kronecker delta	$[-]$
μ	Dynamic viscosity	$[kg/m\ s]$
ν	Kinematic viscosity	$\left[m^2/s\right]$
$\overline{\overline{\Phi}}$	Viscosity tensor	$\left[N/m^2\right]$
$\overline{\overline{E}}$	Deformation tensor	$[1/s]$
$\overline{\overline{I}}$	Identity matrix	$[-]$
$\overline{\overline{T}}$	Tension tensor	$\left[N/m^2\right]$
∂V	Frontier of the control volume	$\left[m^2\right]$
ψ	Stream function	$[-]$
ρ	Density	$\left[kg/m^3\right]$
τ	Viscous shear stress	$\left[N/m^2\right]$
θ	Density gradient (in convective terms discretization)	$\left[kg/m^4\right]$
θ	Oblique shock wave generator (wedge) angle	$[^\circ]$
$\vec{\mathscr{L}}$	Vector of characteristic waves	$[-]$

$\vec{F_S}$	Surface forces	$\left[N/m^2\right]$
$\vec{F_V}$	Volume forces	$\left[N/m^3\right]$
$\vec{f}$	Superficial forces	$[N/kg]$
$\vec{F_i}$	Vector of convective fluxes	$[-]$
$\vec{F_{vi}}$	Vector of viscous fluxes	$[-]$
$\vec{S}$	Vector of source variables	$[-]$
$\vec{U}$	Vector of conservative variables	$[-]$
ξ, η	Similarity variables	$[-]$
C_f	Skin friction	$[-]$
e	Internal energy	$[J/kg\ s]$
E, ε	Total energy	$[J]$
f, f', f'', f'''	Blasius functions for momentum	$[-]$
f_0, f_1, f_2	Auxiliary functions for Blasius functions for momentum	$[-]$
g, g', g''	Blasius functions for energy	$[-]$
g_0, g_1	Auxiliary functions for Blasius functions for energy	$[-]$
H	Total enthalpy	$[J]$
h	Static enthalpy	$[J]$
k	Thermal conductivity	$[W/m\ K]$
M	Mach number	$[-]$
p	Pressure	$[Pa]$
Q	Specific heat per unit of volume	$\left[J/kg\ m^3\right]$
q	Specific heat per unit of area	$\left[J/kg\ m^2\right]$
Re_x	Abscissa Reynolds number	$[-]$
s	Entropy	$[J/K]$
u	Stream-wise component of the velocity	$[m/s]$
V	Control volume	$\left[m^3\right]$
v	Normal-wise component of the velocity	$[m/s]$
w	Work flux	$[J]$
x	Stream-wise coordinate	$[m]$
y	Normal-wise coordinate	$[m]$

Parameters

α	Boundary layer parameter	≈ 4.91
γ	adiabatic index	1.4
C	Chapman-Rubesin parameter	≈ 1
c_p	Specific heat at constant pressure	$[J/kg\ K]$
Pr	Prandtl number	0.72
S	Sutherland's law parameter (*effective temperature*)	110.4
T_0	Sutherland's law reference temperature	273.15 $[K]$

Subscripts

$(_\infty)$	Property of the undisturbed flow far from the plate
$(_{det})$	Boundary layer detachment location
$(_e)$	Variable of the external solution of the boundary layer
$(_i)$	Variable of the internal solution of the boundary layer
$(_{max})$	Maximum value
$(_{min})$	Minimum value
$(_{reatt})$	Boundary layer reattachment location
$(_R)$	Recovery value
$(_{sh})$	Nominal impingement location (inviscid case)
$(_{tr})$	Threshold value
$(_V)$	Property referred to the control volume
$(_W)$	Property defined on the wall

Superscripts

$(')$	Differentiation in respect to η (in boundary conditions)
$(')$	Property determined inside the boundary layer (in boundary layer equations)
$(^*)$	Non-dimensionalized variable
$\left(^0\right)$	Value on the surface of the plate
$\left(^{\partial V}\right)$	Property referred to the frontier of the control volume
$\left(^\top\right)$	Transpose of a vector
$\left(^{Cf_{min}}\right)$	Property referred to the section where the minimum skin friction is
$\left(^{global}\right)$	Value referred to the global domain
$\left(^{inv.}\right)$	Property referred to the inviscid case

Contents

1 Introduction

This thesis deals with the study of the dynamics of the boundary layer that covers a flat plate hit by a uniform supersonic flow when it is incised by an oblique shock wave. This phenomenon is usually called as Shock Wave Boundary Layer Interaction (SWBLI).
The work of this thesis has been carried out in collaboration with the group of research *CFD and Optimization METhods for Engineering and Science* (COMETES) at the Industrial Engineering department of the University of Padova, with the purpose of being a starting point for the study of wall flows in compressible conditions and supersonic boundary layer problems.
The research in this area is rather active since the relevance of this topic in situations involving systems interested by transonic and supersonic flows such as high-speed turbo-machinery, propulsion system nozzles, etc.
Acquiring awareness of the effects of this extremely complex phenomenon makes it possible to develop more accurate engineering models to study the behaviour of systems that are interested in it and also to provide a useful tool for forecasting and preventing the consequences that the onset of this phenomenon has on the aforementioned systems.
The effects of the interaction of a shock wave with the boundary layer manifest themselves in the thermal stress on the wall, in the loss of aerodynamic efficiency caused by the alteration, if not detachment, of the boundary layer and in the mechanical fatigue induced on the wall due to of turbulence.
The SWBLI dynamic in the case of a turbulent flow has a common background with the laminar one, since the major effects regard low frequencies, therefore the study in the present thesis starts with the laminar SWBLI case allowing future studies to exploit the results obtained in this one as tools for the protraction to the study of the turbulent case.
Moreover the turbulent case is rather chaotic, then numerical instabilities become quite difficult to be distinguished from the physical behaviour of the flow, therefore an accurate laminar model must be made up before it.
The lack of experimental data on this topic is due to the difficulty in recreating the phenomenon [16], keep in mind that the recreation of a laminar SWBLI is a rather delicate experiment that requires an almost-cryogenic flow. More than that come difficulties in extracting the informations of interest using an instrumentation which is relatively thick in comparison to the dimensions of the region in contact with the wall, where the data of interest are located, causing the perturbation of the field of motion. From the computational point of view, the non-absolute accuracy of experimental models and the complexity of analytical models forces the adoptions of simplifications which introduce approximations that induce the engineers to consider the results in a qualitative way. For example take into account a more realistic turbulent flow (e.g. [33], [26], [30], [14]), where the approximations of its mathematical models cause a greater separation from the exact solution due to the complexity of the problem, if for example comes the need to execute the modal analysis of the structure subjected to vibrations induced by pressure oscillations on the wall, the knowledge of frequencies involved must be as accurate as possible since these can provoke resonances that can be dangerous for the structure itself.
Therefore, in order to being able to better describe the physics of SWBLI dynamics using more accurate models, more research in fluid dynamics and in the mathematics associated to it are required.
When the simulation models are realized, a very important step is the validation of the parts that compound the model and the global model itself. This is due to the fact that small oversights can lead to more or less marked deviations that unknowingly distort the results obtained. Then the further analysis can be carried out.

Thus, the steps that make up a research in this topic can be summarized as:

- realization of the model;
- validation of the model;
- further analysis.

While the wall pressure and the skin friction are always present in the majority of the researches, one of the main aspects of the SWBLI that usually gets ignored by researchers is the description of its the thermal behaviour. Probably this is due to the fact that this target is rather delicate since approximations in the inlet conditions can lend to discrete differences in the thermal trend along the plate making comparisons between different models difficult.
Nevertheless, while keeping the awareness of the approximations made to the model, a macroscopic behaviour can still be described.

The present thesis is divided in five parts:

1. a first part regarding the presentation of the phenomenon (section 2);
2. a second part where the resolution model adopted gets described (sections 3 - 6);
3. a third part where the model gets validated (section 7);
4. a fourth part where analysis on the major aspects of the SWBLI for several Mach numbers having fixed the shock wave generator angle (section 8) and for several Mach numbers having fixed the shock wave angle (section 9) are made;
5. a fifth and last part concerning a summary of the results and tips on further studies (section 10).

2 Phenomenon presentation

Now the parts that make up the SWBLI get presented:

- boundary layer covering a flat plate (sec. 2.1);
- oblique shock wave (sec. 2.2);

and then follows up the explanation in a qualitative way of the dynamic of their interaction (sec. 2.3).

2.1 Boundary layer

Generally in a fluid-dynamic domain, at the borders of which there is the presence of a wall, the boundary conditions given there are those of *adherence* (tangential component of the flow speed is zero) and *impermeability*, (normal component of the flow speed is zero). On the contrary, the points of the flow far from the wall have their undisturbed velocity. This implies the existence of a region in which the flow velocity is affected by the presence of the wall and it starts from zero in contact with it and gradually recovers its undisturbed value moving far from it.
By *boundary layer* is intended the region in which the flow velocity is less than or equal to 99% of the undisturbed one.

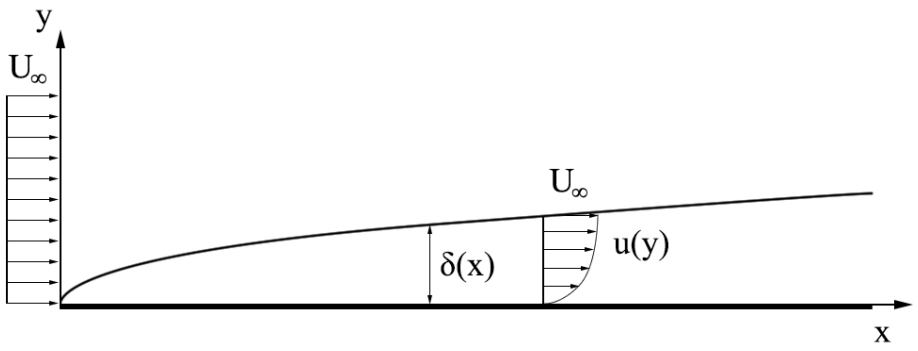

Figure 1: Boundary layer that covers a flat plate.

Let's consider the case of the flat plate, the boundary layer thickness δ depends on the distance between the considered point along x-axis and the leading-edge of the plate, in particular:

$$\frac{\delta(x)}{x} = \frac{\alpha}{\sqrt{Re_x}} \tag{2.1.1}$$

where α is a parameter that depends on the model assumed to describe the shape of the velocity profile $u(y)$ and Re_x represents the abscissa Reynolds Number,

$$Re_x = \frac{\rho U_\infty}{\mu} x \tag{2.1.2}$$

Generally can be assumed that the velocity profile respects the incompressible *Blasius solution* (sec. 2.1.1) for which $\alpha \approx 4.91$.
Substituting in (2.1.1) is obtained:

$$\delta(x) = \frac{4.91\ x}{\sqrt{Re_x}} = \frac{4.91\ x}{\sqrt{\frac{\rho U_\infty x}{\mu}}} = \frac{4.91\ \sqrt{x}}{\sqrt{\frac{U_\infty}{\nu}}} = 4.91\sqrt{\frac{\nu x}{U_\infty}} \tag{2.1.3}$$

in which can be noted that the boundary layer thickness is proportional to $\sqrt{x}$.

The incompressible boundary layer gets described by the *boundary layer equations* (B.0.5) (see appendix B):

However in the present thesis the flow is compressible, then let's consider the Navier-Stokes equations obtained in appendix A.

$$\begin{aligned}
&\frac{\partial(\rho u)}{\partial x} + \frac{\partial(\rho v)}{\partial y} = 0 \\
&\rho u\frac{\partial u}{\partial x} + \rho v\frac{\partial u}{\partial y} = -\frac{\partial p}{\partial x} + \frac{\partial \Phi_{ii}}{\partial x} + \frac{\partial \Phi_{ij}}{\partial y} \\
&\rho u\frac{\partial v}{\partial x} + \rho v\frac{\partial v}{\partial y} = -\frac{\partial p}{\partial y} + \frac{\partial \Phi_{ji}}{\partial x} + \frac{\partial \Phi_{jj}}{\partial y} \\
&\rho u\frac{\partial h}{\partial x} + \rho v\frac{\partial h}{\partial y} = u\frac{\partial p}{\partial x} + v\frac{\partial p}{\partial y} + \frac{\partial}{\partial x}\left(\frac{\mu}{Pr}\frac{\partial h}{\partial x}\right) + \frac{\partial}{\partial y}\left(\frac{\mu}{Pr}\frac{\partial h}{\partial y}\right) + \\
&\qquad + \Phi_{ii}\frac{\partial u}{\partial x} + \Phi_{ij}\frac{\partial u}{\partial y} + \Phi_{ji}\frac{\partial v}{\partial x} + \Phi_{jj}\frac{\partial v}{\partial y}
\end{aligned} \tag{2.1.4}$$

These equations describe the compressible flow of a continuum system. The procedure to obtain the compressible boundary layer equations is similar to the one for the incompressible case, i.e. introduction of coordinates transformation and neglect terms considering high Reynolds numbers. Then considering the boundary layer approximations, the equations found are:

$$\begin{aligned}
&\frac{\partial(\rho u)}{\partial x} + \frac{\partial(\rho v)}{\partial y} = 0 \\
&\rho u\frac{\partial u}{\partial x} + \rho v\frac{\partial u}{\partial y} = -\frac{\partial p}{\partial x} + \frac{\partial}{\partial y}\left(\mu\frac{\partial u}{\partial y}\right) \\
&\frac{\partial p}{\partial y} = 0 \\
&\rho u\frac{\partial h}{\partial x} + \rho v\frac{\partial h}{\partial y} = u\frac{\partial p}{\partial x} + \frac{\partial}{\partial y}\left(\frac{\mu}{Pr}\ \frac{\partial h}{\partial y}\right) + \mu\left(\frac{\partial u}{\partial y}\right)^2
\end{aligned} \tag{2.1.5}$$

where Pr is the adimensional *Prandtl number*

$$Pr = \frac{\mu\ c_p}{k} \tag{2.1.6}$$

which is a fundamental parameter related to properties of the fluid only.
Equations (2.1.5.b) and (2.1.5.c) are the momentum equations in x and y directions and equation (2.1.5.d) is the energy equation in terms of enthalpy.

2.1.1 Similarity solutions for compressible boundary layer

Consider equations (2.1.5) that describe a compressible steady flow.
These equations can be simplified by introducing transformations that convert the compressible boundary layer into an equivalent incompressible one [47], [45], [5].
A common transformation adopted is the Illingworth transformation that will be explained below.

Illingworth transformation This transformation consists in the introduction of a function called *stream function* $\psi(x,y)$ which for compressible flows is defined in order to solve the continuity equation, since the validity of Schwarz's theorem:

$$\frac{\partial \psi}{\partial y} = \rho u \qquad \frac{\partial \psi}{\partial x} = -\rho v \tag{2.1.7}$$

The idea is to introduce two similarity variables (ξ and η) and to check when the stream function ψ and the velocity profile u take the form:

$$\begin{aligned} \psi(\xi,\eta) &= \int \rho u \, \mathrm{d}y = G(\xi) f(\eta) \\ u(\xi,\eta) &= U_\infty(\xi) f'(\eta) \end{aligned} \tag{2.1.8}$$

Illingworth then assigned the viscosity effects in ξ and the density effects in η. This means that

$$\begin{aligned} \xi = \xi(x) &= \int_0^x \rho_\infty(x) U_\infty(x) \mu_\infty(x) \, \mathrm{d}x \\ \eta = \eta(x,y) &= \frac{U_\infty(x)}{\sqrt{2\xi}} \int_0^y \rho \mathrm{d}y \end{aligned} \tag{2.1.9}$$

where subscript ∞ indicates the value external to the boundary layer.
Substituting these definitions in (2.1.5.b) results in

$$(Cf'')' + ff'' + \frac{2\xi}{U_\infty}\frac{\mathrm{d}U_\infty}{\mathrm{d}\xi}\left(\frac{\rho_\infty}{\rho} - f'^2\right) = 0 \tag{2.1.10}$$

in which

$$C = \frac{\rho\mu}{\rho_\infty \mu_\infty} \sim C(\eta)$$

is the Chapman-Rubesin parameter [4], [5].
The apex ($'$) denotes differentiation in respect to η.
Let's consider the energy equation (2.1.5.d). The enthalpy can be divided into the product of a *magnitude* function and a *shape* function

$$h(x,y) = h_\infty(\xi) g(\eta) \tag{2.1.11}$$

which substituted in (2.1.5.d) and considering $H_\infty = h_\infty + U_\infty^2/2$ the total entalphy, results in

$$\left(\frac{C}{Pr} g'\right)' + fg' = \left(\frac{\xi}{H_\infty}\frac{\mathrm{d}H_\infty}{\mathrm{d}\xi}\right)\left(2g + \frac{U_\infty^2}{h_\infty} f'^2\right) f' - \frac{U_\infty^2}{h_\infty} C f''^2 \tag{2.1.12}$$

The target of similarity for equations (2.1.10) and (2.1.12) is obtained only under some conditions:

- $C = \text{const}$ or is function of f and g;
- $Pr = \text{const}$ or is function of f and g;
- ρ_∞/ρ is function of f and g;
- $(2\xi/U_\infty)\,\mathrm{d}U_\infty/\mathrm{d}\xi = \text{const}$;
- $U_\infty^2/h_\infty = \text{const}$ or negligible;
- $(2\xi/H_\infty)\,\mathrm{d}H_\infty/\mathrm{d}\xi = \text{const}$

The first three conditions are verified assuming the gas to be perfect. This means that assuming $c_p \approx const$

$$\frac{\rho_\infty}{\rho\,(y)} = \frac{T\,(y)}{T_\infty} \approx \frac{h\,(y)}{h_\infty}$$

for (B.0.3) the pressure is constant along y-coordinate, so

$$\frac{\rho_\infty}{\rho} \approx g\,(\eta)$$

$$\frac{h_\infty}{h}\frac{\mu}{\mu_\infty} \approx \left(\frac{h}{h_\infty}\right)^{-1}\left(\frac{T}{T_\infty}\right)^{n} = \left(\frac{h}{h_\infty}\right)^{n-1} = g\,(\eta)^{n-1} = C\,(\eta)$$

for air $n \approx 2/3$, that is

$$C = \frac{\rho\mu}{\rho_\infty\mu_\infty} \approx g^{n-1} \approx g^{-1/3} \tag{2.1.13}$$

and the Prandtl number is assumed constant for air $Pr = 0.72$. Considering adiabatic flow over a flat plate 4th to 6th conditions are satisfied since U_∞ and H_∞ are constant.
Using these conditions the (2.1.10) and (2.1.12) equations become

$$(Cf'')' + ff'' = \beta\left(f'^2 - g\right) \tag{2.1.14}$$

$$(Cg')' + Prfg' = -PrC\,(\gamma - 1)\,M_\infty^2 f''^2 \tag{2.1.15}$$

in which for a flat plate

$$\beta = \frac{2\xi}{M_\infty}\frac{\mathrm{d}M_\infty}{\mathrm{d}\xi} = 0$$

These equations are very similar to the incompressible solutions except for the C parameter that couples them.
In order to simplify considerably their resolution the C parameter can be approximated to ≈ 1 since $g^{-1/3}$ is rather small along y.
In this way they result in the *Blasius relations* for the compressible adiabatic flow over a flat plate

$$f''' + ff'' \approx 0 \tag{2.1.16}$$

$$g'' + Prfg' = -Pr\,(\gamma - 1)\,M_\infty^2 f''^2 \tag{2.1.17}$$

which can be solved in order to obtain the velocity, temperature and density profiles across the boundary layer.

2.2 Oblique shock wave

Consider an undisturbed supersonic flow and imagine to immerse a disturbing body into it. The only way for the flow to know about the presence of the body is through shock waves that deviate the flow in order to make it respect the just changed boundary conditions.

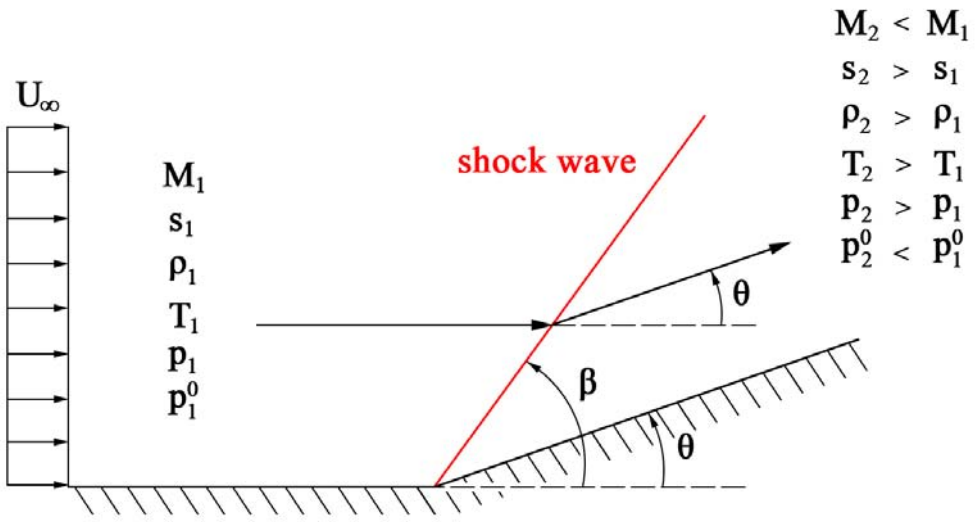

Figure 2: The direction of the flow gets deviated by the angle θ due to the formation of the β-angled shock wave in order to make the flow respect the change in boundary conditions caused by the sudden ramp on the bounding wall.

A shock wave is an highly thin region where the flow properties can change drastically due to an adiabatic compression phenomenon.
In the case of this thesis the undisturbed flow is the one bounded by the flat plate and the disturbing body is the oblique shock wave generator which consists in a wedge.
Consider the properties of the flow, i.e. velocity, Mach number[1], static pressure, total pressure, density, static temperature and entropy. In general across the shock wave the velocity, Mach number and total pressure decrease while static pressure, density, static temperature and entropy increase. Since the component of the velocity parallel to the shock wave stays unchanged, usually the Mach number downstream the oblique shock wave remains higher than 1, but still lower than the upstream one.
The properties variation across the shock wave is described by the *Rankine-Hugoniot equations* derived in appendix C, but in a more explicit way by equations (C.0.10)–(C.0.13).

[1]Mach number ahead of the shock wave must be higher than 1: let's take into account the relation between entropy variation and the upstream Mach

$$s_2 - s_1 \approx \frac{2}{3}\frac{\gamma R}{(\gamma+1)^2}\left(M_1^2 - 1\right)^3 \tag{2.2.1}$$

if $M_1 < 1$ the entropy would decrease across the shock wave which would violate the second principle of thermodynamics.

2.3 SWBLI

The interaction between the oblique shock wave and the boundary layer as said in the introduction is complex and rather common in transonic and supersonic applications [1].

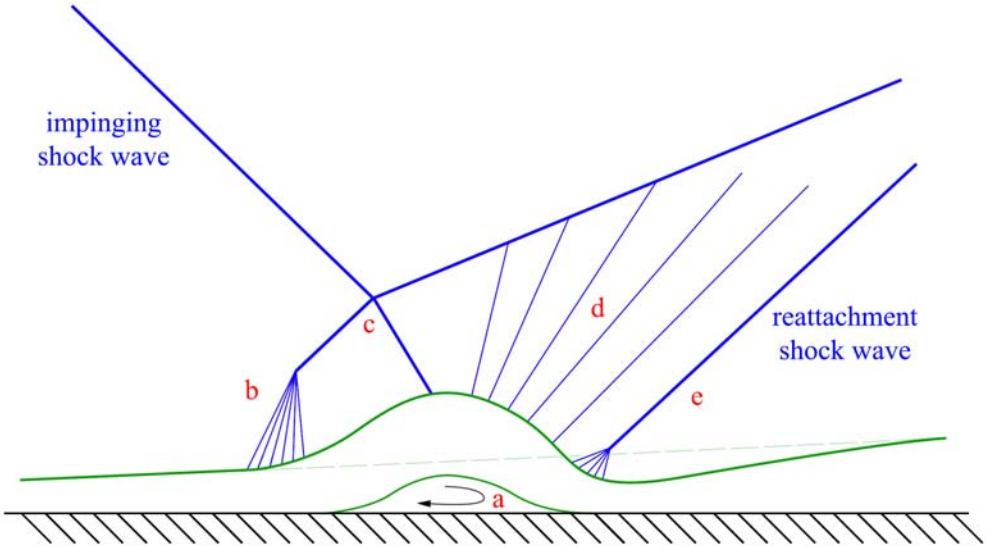

Figure 3: Dynamics of the shock wave boundary layer interaction.

Refer to figure 3. When the shock wave encounters the boundary layer a high adverse pressure gradient takes place, which separates the boundary layer causing a thickening of it. The flow in this region inverses its direction generating a recirculation bubble (a).
In order to respect the change in boundary conditions caused by the thickening of the boundary layer due to the separation, a series of infinitesimal shock waves (compression fan) takes place upstream the bubble (b) which generate a finite shock wave that interacts with the impingement one slightly deviating it (c).
The separated boundary layer then reattaches at some point behind the impingement. For the same reason of the compression fan, the flow that exceeds the recirculation bubble encounters an expansion fan that deviates the flow against the plate (d).

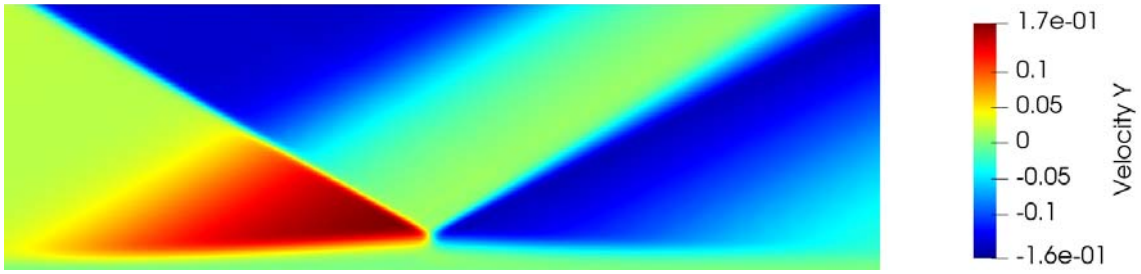

Figure 4: Field of vertical velocities showing the changes in direction of the flow around the SWBLI in order to respect the local boundary conditions.

Once the flow reaches the nearest region to the plate where the boundary layer become relatively thin, a *reattachment shock wave* takes place in order to make the flow respect the boundary conditions (e).
In this region there is a high aerodynamic heating that stresses the plate.
Mainly the SWBLI affects the pressure, shear stress and heat transfer distributions along the wall. Depending on factors such as the intensity of the shock wave and the viscosity of the boundary layer, the recirculation bubble gets bigger or smaller with different vorticities and their sizing, albeit in a qualitative way, it's important and it's the object of many researches in this topic.
By looking at this dynamic it is clear that its complexity is given by the fact that when the shock wave interacts with the boundary layer that consequently deforms itself, the boundary conditions get changed so that, in a way, the "new" boundary layer interacts with the impinging shock wave that deforms as well. That is, the phenomenon is given by the reciprocal interaction between the impinging shock wave and the boundary layer.

3 Solver model

In order to carry out this thesis work, Francesco de Vanna's PhD activity was took in advantage [10], which consists in the realization from scratch of a numerical solver *Unsteady Robust All-around Navier-StOkes Solver* (URANOS), with the purpose of the fluid simulation of compressible viscous flows capable of dealing with moving bodies at high-Mach numbers with high order accuracy and high resolution.
Whereupon, the work in this thesis focused on some parts of URANOS in order to set up the SWBLI model.
The latter is based on the resolution of the Navier-Stokes equations (A.3.20). As said in appendix A this system is made of 4 equations and 6 unknowns, so at least two more equations are needed to close the system.
Then the hyperbolic equations of Navier-Stokes are solved time-wise using the *3rd order explicit Runge-Kutta* integrating method that limits the amount of oscillations among time maintaining stability (see e.g. [15], [12]).
The main error sources are due to numerical approximations in calculations like integration and differentiation, analytical approximations in setting boundary conditions and numerical instabilities in the mathematical models used to solve the fluid domain [35].
In order to carry out the computation some assumptions must be done, which will be briefly summarized below.

3.1 Solving considerations

As said above the resolubility of the Navier-Stokes system of equations can be achieved by considering two more equations.
The two adopted are an equation of state for the fluid

$$\frac{p}{\rho} = RT \tag{3.1.1}$$

that is, the fluid obeys the ideal gas state law, and an equation for the internal energy

$$e = \frac{pR}{\gamma - 1} \tag{3.1.2}$$

where R is the universal gas constant and γ is the heat capacity ratio.
At this point the system is made of 7 equations and 7 unknowns, that means that the problem is closed.
The molecular viscosity μ depends on the temperature for Newtonian fluids, since it is strictly related to molecular interactions, and obeys the formula derived from the kinetic theory of Sutherland, which is the *Sutherland's Law* [47]:

$$\mu = \left(\frac{S + T_0}{S + T}\right) T^{3/2} \tag{3.1.3}$$

where T_0 is the reference value of $273.15K$ and S is the constant *effective temperature* that depends on the fluid involved. In the present thesis is assumed that $S = 110.4$ which is the value corresponding to air.
The analytical model equations are made non-dimensional to carry out the computation.
Since the non-dimensional groups are given, the reference variables can be set to an arbitrary value, and the most convenient choice is to put them unitary, i.e. $T_\infty = 1$, $p_\infty = 1$, $\rho_\infty = 1$.

4 Spatial discretization of the domain

The grid used to discretize the fluid domain has two dimensions: the stream-wise component (x) and the vertical one (y).
Along x-axis the grid is uniform so that the flow can be uniformly described and in the case of future works on turbulent flows it will be possible to easily capture the informations required to take into account the Kolmogorov scales of the flow along the entire stream. The number of nodes assigned along x must be high enough to represent the shock waves without having them to split and diverge due to the numerical instability caused by the discretization of a continuous domain.
The y-axis discretization consists in an hyperbolic distribution, thicker near the plate, in order to being able to describe as accurately as possible the dynamics occurring in the boundary layer, with particular attention to the region interested by the recirculation bubble.
The law that defines the hyperbolic distribution is [10]

$$x(\xi) = 1 + \frac{tanh[\alpha(\xi - 1)]}{tanh(\alpha)} \tag{4.0.1}$$

where α is a parameter that permits to manage the stretching of the distribution along y and ξ is a coordinate on the uniform grid where the properties of the flow get computed and then get converted into the non-uniform grid by coordinate transformation.
The number of nodes in the y dimension must respect a compromise: it must be high enough to describe sufficiently well the boundary layer, but it mustn't be too high since that means that cells near the wall become very small and for the Courant-Friedrichs-Lewy problem [7], the steps of the time discretization become highly thin causing an increment of the computation load.

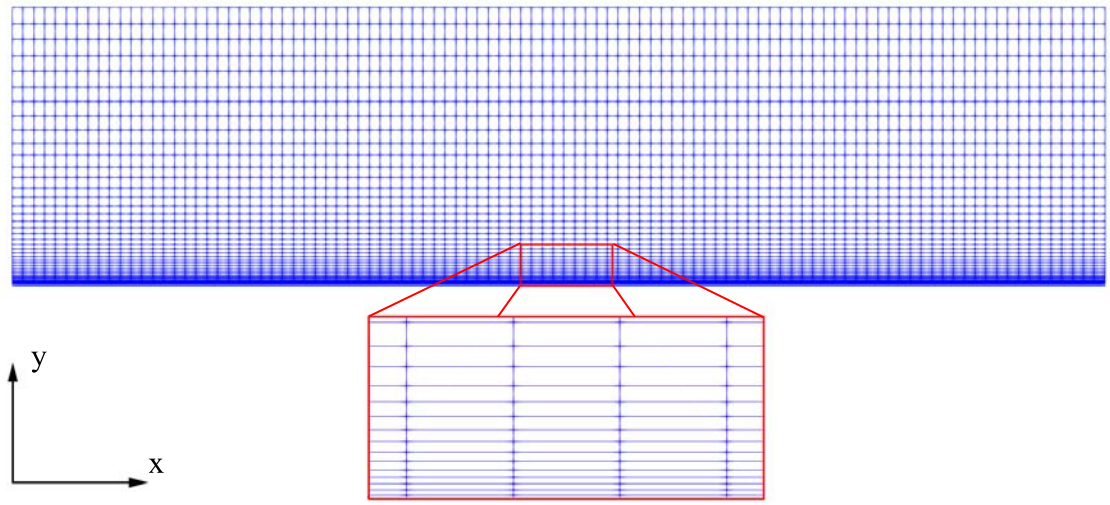

Figure 5: Grid discretization along x-axis and y-axis.

5 Discretization of terms regarding the spatial variation of the flow properties

Terms that consider the spatial variation of the properties of the flow, i.e. convective and viscous ones, can give numerical instabilities or inaccuracy if they are employed in a not appropriate way, for example the encounter of a sharp gradient as the one given by the shock wave could generate numerical oscillations around that region.
The objective of this section is to briefly present the shrewdnesses and solutions adopted to reduce numerical instabilities.
Firstly will be described the treatment of convective terms in section 5.1, then will follow the explanation of the treatment of viscous terms in section 5.2.

5.1 Discretization for convective terms

The discretization of convective terms requires particular attention since numerical instabilities are easy to be protracted in the resolution of the flow, especially when facing cases that involve particular behaviours of the flow as the one studied in this thesis.

5.1.1 WENO scheme

In the presence of sharp gradients of the flow variables, as in the case of shock waves, particular attention must be payed since these get translated into discontinuites by the discretization of continuous fields, and using an usual discretization one can occur in numerical fluctuations around them. This problem is well known as *Gibbs phenomenon*.
These fluctuations are taken into account by the solver and get propagated ending up perturbing the solution.
In order to avoid this problem an appropriate discretizing method must be adopted, which is based on Weighted Essentially Non-Oscillatory schemes (WENO) [3], [27].
The one used in the work of this thesis is called *WENO-Z*, which is a 5th order Weighted Essentially Non-Oscillatory scheme, and it consists in the definition of an high-order polynomial centred around the cell $j + 1/2$ through a non-linear weighted combination of other three support polynomials.
In this way when a shock wave sharp gradient is encountered, the solution gets propagated automatically with high accuracy and avoiding numerical fluctuations.
The WENO schemes are a subfamily of the older *Essentially Non-Oscillatory* schemes (ENO) which use only one stencil instead of n of them (3 in this case).

5.1.2 Central scheme

Where the WENO method is not needed, i.e. far from the sharp gradients, it is better to adopt a central scheme in order to save computational cost obtaining moreover an higher accuracy.
Convective terms contain the differentiation of the product of variables and when this operations get handled by the solver, a numerical error get introduced in the resolution: the *aliasing error*.
This problem is shared by all type of schemes and causes an artificial shift of the spectral energy content from low to high wave numbers, that is, there is a drop in energy at low wave numbers simultaneously with an increase in energy at high wave numbers.
It is clear that this problem is related to the mathematical form of the convective terms, therefore while different forms of them share the same physical meaning, the numerical results are different.
For this reason since the flow is compressible the low-dissipative, locally-conservative approximation

realized by a *6th-order central fully split approximation*[2] of convective terms gets adopted, so called *KGP6* since developed by Kennedy-Gruber-Pirozzoli [20] (see also [28], [38]), which is currently the most robust in literature for shock-free flows.
This scheme defines an expansion of convective terms in a local-conservative way in order to preserve the total mass, the momentum and the energy of non-viscosity flows at low Mach numbers.

$$\frac{\partial \rho u_j \psi}{\partial x_j} = \frac{1}{4}\frac{\partial \rho u_j \psi}{\partial x_j} + \frac{1}{4}\left(u_j \frac{\partial \rho \psi}{\partial x_j} + \rho \frac{\partial u_j \psi}{\partial x_j} + \psi \frac{\partial \rho u_j}{\partial x_j}\right) + \frac{1}{4}\left(\rho u_j \frac{\partial \psi}{\partial x_j} + \rho \psi \frac{\partial u_j}{\partial x_j} + u_j \psi \frac{\partial \rho}{\partial x_j}\right) \quad (5.1.1)$$

5.1.3 Hybrid scheme

Since this work involves the simulation of a fluid field of which only a minor portion is interested by the presence of the shock wave, the two methods presented above must be implemented jointly. That means that the spatial discretization is an hybrid that mutates as the shock wave(s) evolves into the domain. For this reason an automatized method must be used in order to automatically define where is appropriate to adopt the WENO scheme or the central one.
This methods are called *shock detection techniques* and consist in the determination of the regions where the shock waves will be located [10].
In order to detect the shock waves the density gradient gets computed

$$\theta = max\left(\frac{\partial \rho}{\partial x_j}\right)_{j=1,3} \quad (5.1.2)$$

Introducing a proper threshold value for θ the solver can distinguish where to implement the WENO scheme ($\theta > \theta_{tr}$) and where the central one ($\theta < \theta_{tr}$).

5.2 Discretization for viscous terms

Viscous terms are present in the momentum equation and in the energy equation through the viscosity tensor

$$\begin{aligned} \text{momentum:} \quad & \frac{\partial}{\partial x_i}\left(\mu_\infty \Phi_{ji}\right) \\ \text{energy:} \quad & \frac{\partial}{\partial x_i}\left(\mu_\infty \Phi_{ji} u_j + \frac{\mu_\infty}{Pr}\frac{\gamma}{\gamma - 1} k \frac{\partial T}{\partial x_j}\right) \end{aligned} \quad (5.2.1)$$

These terms are written in a form that introduces numerical errors due to the product of components that depend on the differentiation variable x_i.
The main purpose is to rewrite them avoiding these operations [38].
As can be seen in section A.2 of appendix A, the viscosity tensor Φ is defined as

$$\overline{\overline{\Phi}} = \mu\left[2\overline{\overline{E}} - \frac{2}{3}\left(\nabla \cdot \vec{v}\right)\overline{\overline{I}}\right] \quad (5.2.2)$$

where

$$\overline{\overline{E}} = \frac{1}{2}\left(\nabla \vec{v} + \nabla \vec{v}^{\top}\right) \quad (5.2.3)$$

[2] the accuracy order number is related to the number of terms considered in the Taylor series expansion to compute derivatives.

so that

$$\overline{\overline{\Phi}} = \mu \left[\left(\nabla \vec{v} + \nabla \vec{v}^{\top} \right) - \frac{2}{3} \left(\nabla \cdot \vec{v} \right) \overline{\overline{I}} \right] \tag{5.2.4}$$

thus, written in an indicial way

$$\Phi_{ji} = \mu \left(\frac{\partial u_i}{\partial x_j} + \frac{\partial u_j}{\partial x_i} - \frac{2}{3} \frac{\partial u_i}{\partial x_i} \delta_{ji} \right) \tag{5.2.5}$$

Taking into account only terms containing the viscosity tensor in (5.2.1) and substituting (5.2.5), results in

$$\begin{aligned} \text{momentum:} \quad & \mu_{\infty} \frac{\partial}{\partial x_i} \left[\mu \left(\frac{\partial u_i}{\partial x_j} + \frac{\partial u_j}{\partial x_i} - \frac{2}{3} \frac{\partial u_i}{\partial x_i} \delta_{ji} \right) \right] \\ \text{energy:} \quad & \mu_{\infty} \frac{\partial}{\partial x_i} \left[\mu \left(\frac{\partial u_i}{\partial x_j} + \frac{\partial u_j}{\partial x_i} - \frac{2}{3} \frac{\partial u_i}{\partial x_i} \delta_{ji} \right) u_j \right] \end{aligned} \tag{5.2.6}$$

where $\mu = \mu \left(x_i \right)$.
Here the differentiation of products that depend on x_i has been written explicitly. In order to avoid numerical instabilities these operations can be solved analytically by expanding the derivatives applying the following basic rules of differential mathematics

$$\frac{\partial}{\partial x} \left(a \cdot b \right) = a' \cdot b + a \cdot b' \tag{5.2.7}$$

$$\frac{\partial}{\partial x} \left(a \cdot b \cdot c \right) = a' \cdot b \cdot c + a \cdot b' \cdot c + a \cdot b \cdot c' \tag{5.2.8}$$

6 Boundary conditions

In this section the boundary conditions will be treated.

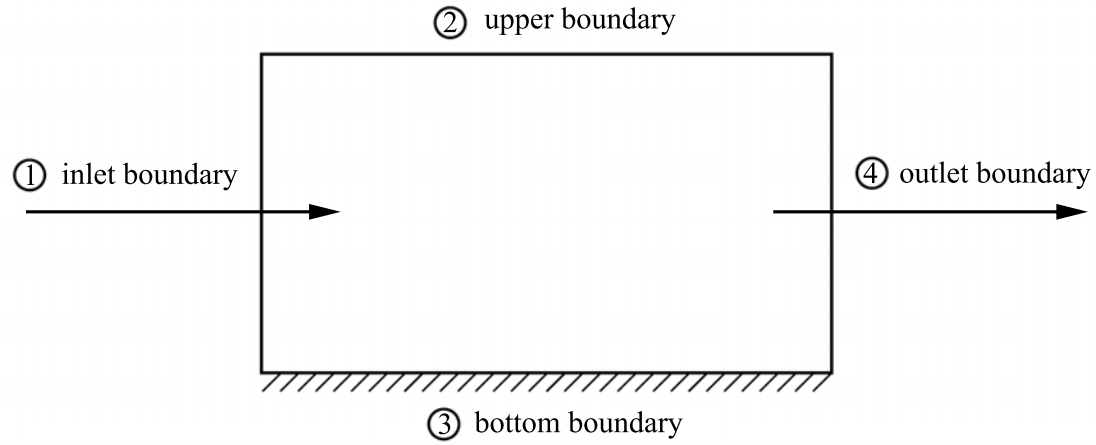

Figure 6: Boundaries of the simulation domain. Each of them requires conditions to be applied to.

Referring to figure 6, the domain has 4 interfaces with the outer ambient:

- the inlet on the left;
- the undisturbed stream on top;
- the flat plate on the bottom;
- the outlet on the right.

For each of these boundaries one or more conditions must be declared, conditions that have to be as faithful as possible to the dynamic of the phenomenon that wants to be represented in order to obtain the desired results within a sufficiently small error due to mathematical approximations.
This section will start by presenting the *inlet conditions* in sec. 6.1, then will follow the *upper conditions* in sec. 6.2, after that the *flat plate conditions* will be presented in sec. 6.3 concluding with the presentation of the outlet conditions in sec. 6.4.

6.1 Inlet conditions

The inlet conditions regard the velocity, temperature and density profiles of the flow.
Then the pressure profile gets determined by the state law of ideal gas, using the known density and temperature profiles. As described in appendix B (eq. B.0.3) this one should results constant along y-axis.
As can be seen in appendix 2.1.1 the equations describing the compressible flow inside the boundary layer can be solved separately, but the first one to be solved is the Blasius solution for the velocity profile derived from the momentum equation. Once f and f'' are known, one can proceed

to integrate the energy equation in order to obtain the temperature profile which leads to the knowledge of the density profile as well.
The numerical resolutions for the two equations are very similar and rather stable.

6.1.1 Velocity profile - Blasius solution

The velocity profile given in the inlet respects the Blasius solution (see sec. 2.1.1):

$$ff'' + f''' = 0 \tag{6.1.1}$$

which is a non-linear differential equation of the third order.
This equation is the incompressible solution for the stream-wise velocity, which is an approximation of the compressible case obtained with the assumptions made in section 2.1.1.
The velocity profile is described by f' : $f'(\eta) = u(\eta)/U_\infty$
In order to solve the equation to get the profiles of f, f' and f'' a numerical method is used based on the *Shooting method* algorithm coupled with Euler's integration [25].

Resolutive method The known conditions for the resolution of the Blasius solution are:

1. Adherence condition: $u|_{\eta=0} = 0 \;\Rightarrow\; U_\infty f'(0) = 0 \;\Rightarrow\; f'(0) = 0$
2. Impermeability condition: $v|_{\eta=0} = 0 \Rightarrow (-\partial\psi/\partial x)\,|_{\eta=0} = 0 \Rightarrow$
   $-U_\infty \dot{\delta}\,[f(0) - f'(0)\eta] = 0 \Rightarrow f(0) = 0$
3. Junction condition: $u|_{\eta\to\infty} = U_\infty \;\Rightarrow\; U_\infty f'|_{\eta\to\infty} = U_\infty \;\Rightarrow\; f'|_{\eta\to\infty} = 1$

For the resolution of the problem the first two initial conditions are used $f(0) = 0$ and $f'(0) = 0$, but another condition is missing, in particular the one on the $f''(0)$ which represents the derivative of the velocity profile near the wall.
The *Shooting method* algorithm consists on the assumption of the initial condition for the $f''(0)$, then the solution get integrated and lastly the junction condition get exploited in order to verify the correctness of the initial assumption made.

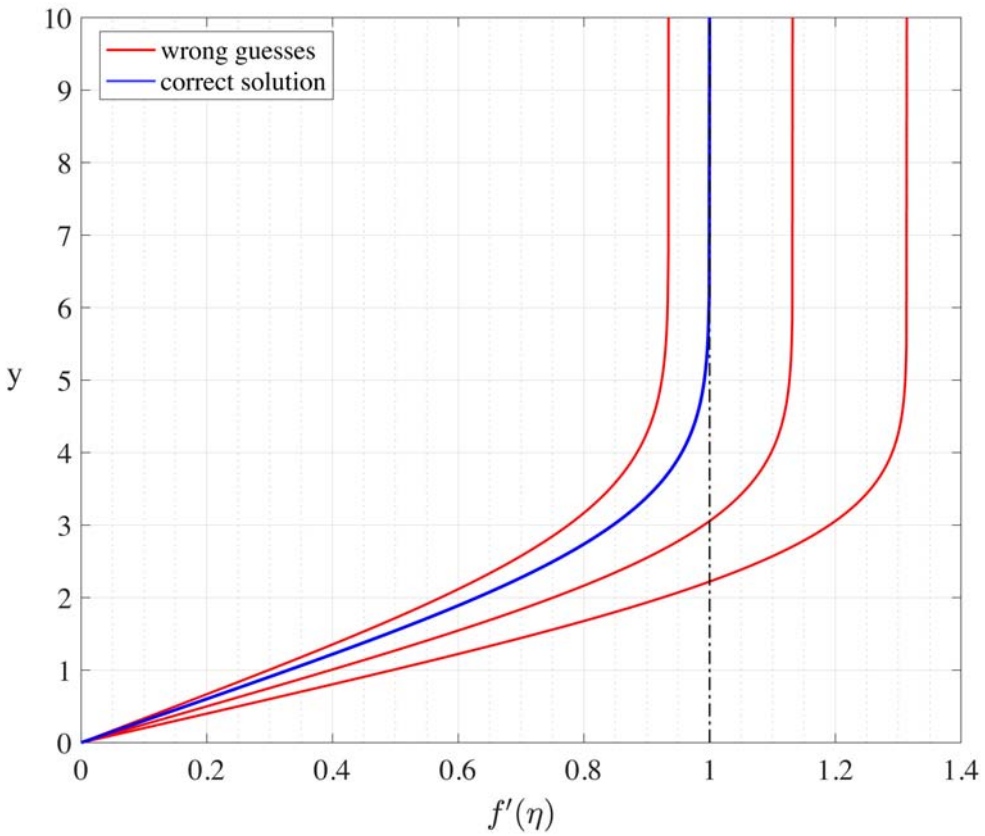

Figure 7: Application of the Shooting method to the Blasius solution: in red the wrong guesses, in blue the correct one.

In order to integrate the non-linear equation of the third order a simple system of the first order get constructed making use of three auxiliary variables:

$$f_0 = f \quad , \quad f_1 = f' \quad , \quad f_2 = f'' \tag{6.1.2}$$

so that

$$\begin{aligned} \frac{\partial}{\partial \eta}(f_0) &= f_1 \\ \frac{\partial}{\partial \eta}(f_1) &= f_2 \\ \frac{\partial^2}{\partial \eta^2}(f_2) &= -\frac{1}{2}\, f_0\, f_2 \end{aligned} \tag{6.1.3}$$

At this point the Euler's integration is implemented between $\eta = 0$ and $\eta \to \infty$, where this last value must be chosen in an appropriate way, otherwise the Blasius solution won't develop correctly (usually $\eta_\infty \geq 10$).

Generally:

$$\begin{aligned} f_0(j) &= f_0(j-1) + f_1(j-1)\cdot d\eta \\ f_1(j) &= f_1(j-1) + f_2(j-1)\cdot d\eta \\ f_2(j) &= f_2(j-1) - \frac{1}{2}\, f_0(j-1)\, f_2(j-1)\cdot d\eta \end{aligned} \tag{6.1.4}$$

from which $f_1(\eta \to \infty)$ is obtained and it get compared with the junction condition.
In order to find the correct assumption for the initial condition on f'' a numerical method can be used, such as bisection (alternatively the secant method can be used for a boost in the convergency speed which becomes super-linear of order $\frac{1+\sqrt{5}}{2} \sim 1.618$).
At last the correct value for f'' converges to ~ 0.3320547 which is the one of the blue curve in (fig.7).

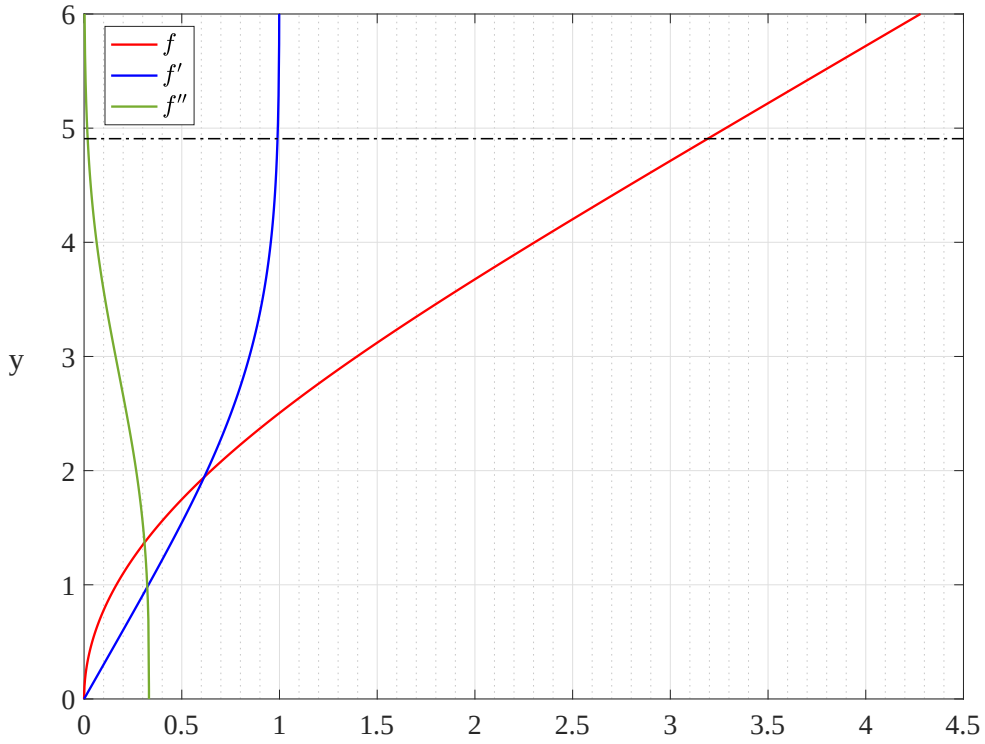

Figure 8: Blasius solutions for f, f' and f".

As can be seen in figure 8, f diverges to infinity, while f' and f'' converges asymptotically respectively to 1 and to 0. Note that f'' starts from ~ 0.332, and corresponding to ~ 4.91 (dash-dot line) the f' reaches the value of 0.99 which equals to the boundary layer thickness for the Blasius solution.

6.1.2 Vertical velocity profile

The inlet of the simulation domain is fixed at a certain distance from the leading-edge of the plate. This means that the inlet conditions that are given have to respect the flow of a developed boundary layer. Since the boundary layer thickens along the plate, a component of the velocity in the vertical direction has to be given.
In contrary of the turbulent regime though, in the laminar one this condition is very weak and does not affect the solution appreciably since its magnitude is negligible in respect to the one of the stream-wise component. It follows that after a short distance from the inlet, the flow corrects itself acquiring its vertical component of the velocity autonomously.
Then in order to slightly lighten the computation cost of the inlet conditions definition, it is decided to omit it.
Anyway, from the theoretical aspect, it is important to take it into account, therefore the obtaining of the analytical equation is explained below.

The solution for the vertical profile of the velocity is found by looking at the definition of *stream function* ψ (sec. 2.1.1)

$$v = -\frac{1}{\rho}\frac{\partial \psi}{\partial x} \tag{6.1.5}$$

The meaning of ψ can be found by integrating the velocity along y

$$\psi = \int_0^{y/\delta(\eta)} u \, \mathrm{d}y = \int_0^{y/\delta(\eta)} U_\infty \; g(\eta) \, \mathrm{d}y = \int_0^{\eta} u \; \delta \; g(\eta) \, \mathrm{d}y = U_\infty \; \delta \int_0^{\eta} g(\eta) \, \mathrm{d}\eta$$

where

$$g(\eta) = \frac{u}{U_\infty}$$

then the equation for the stream function becomes

$$\psi = U_\infty \; \delta \; f(\eta) \tag{6.1.6}$$

Let's consider the definition of the thickness of the boundary layer for the Blasius solution:

$$\delta = 4.91\sqrt{\frac{\nu x}{U_\infty}} \tag{6.1.7}$$

Then substituting (6.1.7) into (6.1.6) results in

$$\psi = 4,91\sqrt{x\nu U_\infty} \; f \tag{6.1.8}$$

differentiating (6.1.8) in respect to x results in

$$\frac{\partial \psi}{\partial x} = \frac{4.91}{2}\sqrt{\frac{\nu U_\infty}{x^3}} f + 4.91\sqrt{x\nu U_\infty} \; \frac{\partial f}{\partial \eta}\frac{\partial \eta}{\partial x} \tag{6.1.9}$$

now

$$\eta = \frac{y}{\delta} = \frac{y}{4.91\sqrt{\frac{x\nu}{U_\infty}}} = \sqrt{\frac{U_\infty}{x\nu}}\frac{y}{4.91} \tag{6.1.10}$$

so

$$\frac{\partial \eta}{\partial x} = -\sqrt{\frac{U_\infty}{\nu}}\frac{1}{2\sqrt{x}}\frac{y}{4.91} \tag{6.1.11}$$

which substituted into (6.1.9) leads to

$$\frac{\partial \psi}{\partial x} = \frac{4.91}{2}\sqrt{\frac{\nu U_\infty}{x}}\ f - 4.91\sqrt{x\nu U_\infty}\ f'\sqrt{\frac{U_\infty}{\nu x^3}}\ \frac{y}{2 \cdot 4.91} \tag{6.1.12}$$

Since $\rho/\mu = 1/\nu$, the definition (2.1.2) can be written as

$$Re_x = \frac{U_\infty}{\nu} x\ , \quad \frac{\nu}{x} = \frac{U_\infty}{Re_x}$$

this one can be substituted into (6.1.12) in order to explicit Reynolds numbers:

$$\frac{\partial \psi}{\partial x} = \frac{4.91}{2}\sqrt{\frac{U_\infty^2}{Re_x}}\ f - 4.91\frac{\sqrt{\nu U_\infty}}{x} f'\sqrt{\frac{U_\infty}{\nu}}\frac{y}{2 \cdot 4.91}$$

which can be simplified to obtain

$$\frac{\partial \psi}{\partial x} = \frac{1}{2} U_\infty \left(\frac{4.91}{\sqrt{Re_x}} f - \frac{y}{x} f' \right) \tag{6.1.13}$$

This last equation can be substituted into (6.1.5) to finally obtain

$$v = -\frac{1}{2\rho} U_\infty \left(\frac{4.91}{\sqrt{Re_x}} f - \frac{y}{x} f' \right) \tag{6.1.14}$$

From this final equation can be seen that the vertical profile of the velocity on a fixed coordinate x is given by the balance of two terms that diverge going to infinite, i.e. f (figure 8) and naturally the coordinate y, that means that from a numerical point of view particular attention must be given to the approximations done in the calculation of every term that makes up the equation, otherwise one term could exceed the other one leading to the divergence of the velocity profile.

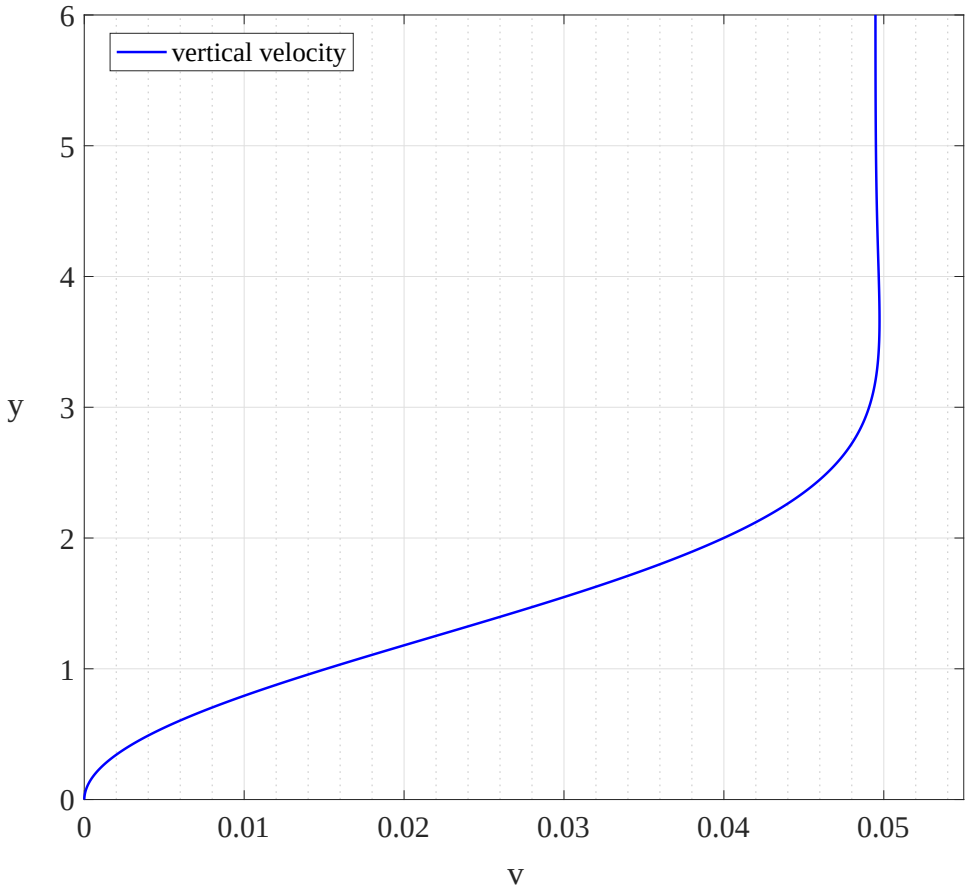

Figure 9: Vertical velocity profile.

6.1.3 Temperature profile

The temperature profile inside the boundary layer depends on the velocity profile which is found solving the Blasius solution of the momentum.
The relationship between the temperature and the velocity is given by several models. More or less all of them are basically derived from the energy equation adopting different assumptions.
In this thesis one of the most common of them gets explained, the solution found by Crocco-Busemann [40], [45], and then is presented the resolution of the exact solution of Blasius for the energy equation which is the one adopted in this work.

Crocco-Busemann profile This relation is valid even for $Pr \neq 1$ and $dp/dx \neq 0$, nevertheless it is obtained in the simplified case of $Pr = 1$ and $dp/dx = 0$.
When $Pr = 1$ the total enthalpy is constant everywhere, so the wall is adiabatic $\partial h/\partial y = 0$, $H = h + 1/2\ u^2$, where H is the total enthalpy.

In order to keep the total enthalpy constant there's a perfect balance between viscous dissipations and heat exchange (energy balance).
Let's consider the energy equation of the compressible boundary layer set of equations (2.1.5.d). When $Pr = 1$ the equations of the energy and momentum become very similar, apart from the dissipation term.
In order to solve this system of equations can be assumed

$$h = h(u) \tag{6.1.15}$$

With $Pr = 1$ the energy equation becomes

$$\frac{\mathrm{d}h}{\mathrm{d}u}\left[\rho u\frac{\partial u}{\partial x} + \rho v\frac{\partial u}{\partial y} - \frac{\partial}{\partial y}\left(\mu\frac{\partial u}{\partial y}\right)\right] = \left(1 + \frac{\mathrm{d}^2 h}{\mathrm{d}y^2}\right)\mu\left(\frac{\partial h}{\partial y}\right)^2 \tag{6.1.16}$$

with $\mathrm{d}p/\mathrm{d}x = 0$ the energy equation becomes

$$\frac{\mathrm{d}^2 h}{\mathrm{d}y^2} = -1 \tag{6.1.17}$$

which has for solution

$$h = -\frac{1}{2}u^2 + A\ u + B \tag{6.1.18}$$

In order to determine h, two boundary conditions are needed:

1. wall: $u = u_W = 0 \rightarrow B = h_W$
2. undisturbed flow: $u = u_\infty = U_\infty \rightarrow A = \left(h_\infty + \frac{1}{2}U_\infty^2 - h_W\right)U_\infty$

where subscripts $_W$ and $_\infty$ denote the values referred near the wall and in the undisturbed region. The boundary conditions above allow to obtain the total enthalpy

$$H = h + \frac{1}{2}u^2 = h_W + (H_\infty - h_W)\frac{u}{U_\infty} \tag{6.1.19}$$

with $C_P = cost$ the equation for the temperature is obtained

$$T = T_W + (T_R - T_W)\frac{u}{U_\infty} - \frac{\gamma - 1}{2}Pr\ M_\infty^2 T_\infty\left(\frac{u}{U_\infty}\right)^2 \tag{6.1.20}$$

where M_∞ and T_∞ are respectively the Mach Number and temperature in the undisturbed region and T_R is the *recovery temperature* that is the temperature on the wall in thermal equilibrium conditions:

$$T_R = T_\infty\left(1 + r\frac{\gamma - 1}{2}M_\infty^2\right) \tag{6.1.21}$$

r is called *recovery factor* and it is the ratio between the temperature increment due to wall friction and the one due to adiabatic compression. For common gases with $Pr \sim 1$ in a laminar flow it is very well approximated by $\sqrt{Pr}$, otherwise in turbulent flow it becomes approximated by $\sqrt[3]{Pr}$.
Substituting (6.1.21) into (6.1.20) the temperature equation can be written as

$$T = T_W + (T_R - T_W)\frac{u}{U_\infty} - (T_R - T_\infty)\left(\frac{u}{U_\infty}\right)^2 \tag{6.1.22}$$

which is the Crocco-Busemann relation between temperature and velocity inside the boundary layer.

Blasius solution - resolutive method Another method to determine the temperature profile inside the boundary layer is the Blasius solution for the energy equation.
Consider the equation derived in section 2.1.1

$$g'' + Prfg' = -Pr\,(\gamma - 1)\,M_\infty^2 f''^2 \tag{6.1.23}$$

This equation allows to determine the temperature profile through the boundary layer having solved the Blasius solution for the velocity in order to obtain f and f''.
As said in section 2.1.1 this equation is derived by an exact math but it is affected by an approximation which involves the uncoupling of the equation for the velocity and the equation for the temperature. This approximation consists in considering the *Chapman-Rubesin parameter C* constant and equal to 1, in other words is made the assumption that f and f'' do not depend on g anymore.
The Blasius solution in the case of the boundary layer over a flat plate is more accurate than the Crocco-Busemann relation, therefore it is the one adopted in this work.
Let's introduce a constant parameter to simplify the equation (6.1.23)

$$A = Pr\,(\gamma - 1)\,M_\infty^2 \tag{6.1.24}$$

so that it can be written as

$$g'' + Prfg' = -A\ f''^2 \tag{6.1.25}$$

The resolution procedure is strictly similar to the one for the velocity profile explained in section 6.1.1. The known boundary conditions are:

1. Adiabatic wall: $\frac{\partial T}{\partial \eta}|_{\eta=0} = 0 \Rightarrow g'(0) = 0$
2. Junction condition: $T|_{\eta\to\infty} = T_\infty \Rightarrow g|_{\eta\to\infty} = 1$

In order to solve this equation the Shooting method is implemented, coupling it with Euler's integration [25]. The boundary condition that is varied in the Shooting method is the value of the temperature on the wall which should be approximately equal to the recovery temperature (6.1.21).
Similarly to the velocity profile, a simple system of the first order is composed using two auxiliary variables:

$$g_0 = g \quad , \quad g_1 = g'$$

considering also the variables introduced for the velocity profile (6.1.2) the system is

$$\begin{aligned} \frac{\partial g_0}{\partial \eta} &= g_1 \\ \frac{\partial g_1}{\partial \eta} &= -Prf_0\ g_1 - A\ f_2^2 \end{aligned} \tag{6.1.26}$$

This system gets integrated along η implementing Euler's algorithm.
Generally:

$$\begin{aligned} g_0(j) &= g_0(j-1) + g_1(j-1)\cdot d\eta \\ g_1(j) &= g_1(j-1) - \left[Prf_0(j-1)\ g_1(j-1) + A\ f_2(j-1)^2\right]\cdot d\eta \end{aligned} \tag{6.1.27}$$

At the end the value of $g_0(\eta \to \infty)$ is found, which should be equal to 1 as stated by the junction condition.

In order to satisfy this condition a numerical method can be adopted, in this work the bisection method is used.

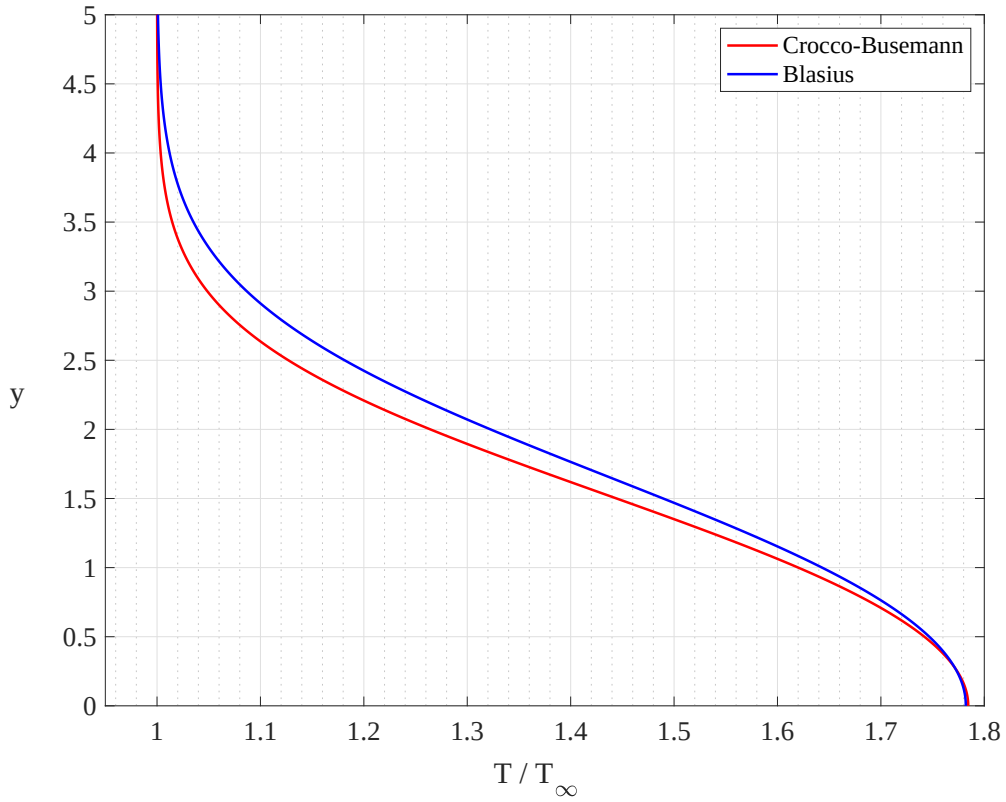

Figure 10: Temperature profiles based on Crocco-Busemann and Blasius solutions.

In figure 10 there are represented the Crocco-Busemann and Blasius models for the temperature profile and can be noticed the slightly difference between them. Nevertheless they both share the same trend of the temperature increment inside the boundary layer.

6.1.4 Density profile

Another condition to be defined at the inlet is the density profile. Once the temperature profile has been obtained, this property is way simpler to be determined than the others above.
Since the boundary layer is thickening along x the particles of the flow must follow his way upward, that means that the density near the plate decreases.
This can be seen in analytical way considering the state law for ideal gases

$$\frac{p}{\rho} = RT \tag{6.1.28}$$

for (B.0.3) along the boundary layer the pressure is constant, so

$$\rho \propto \frac{1}{T} \tag{6.1.29}$$

that is, the density decreases as the temperature increases.
The density profile obtained can be seen in figure 11.

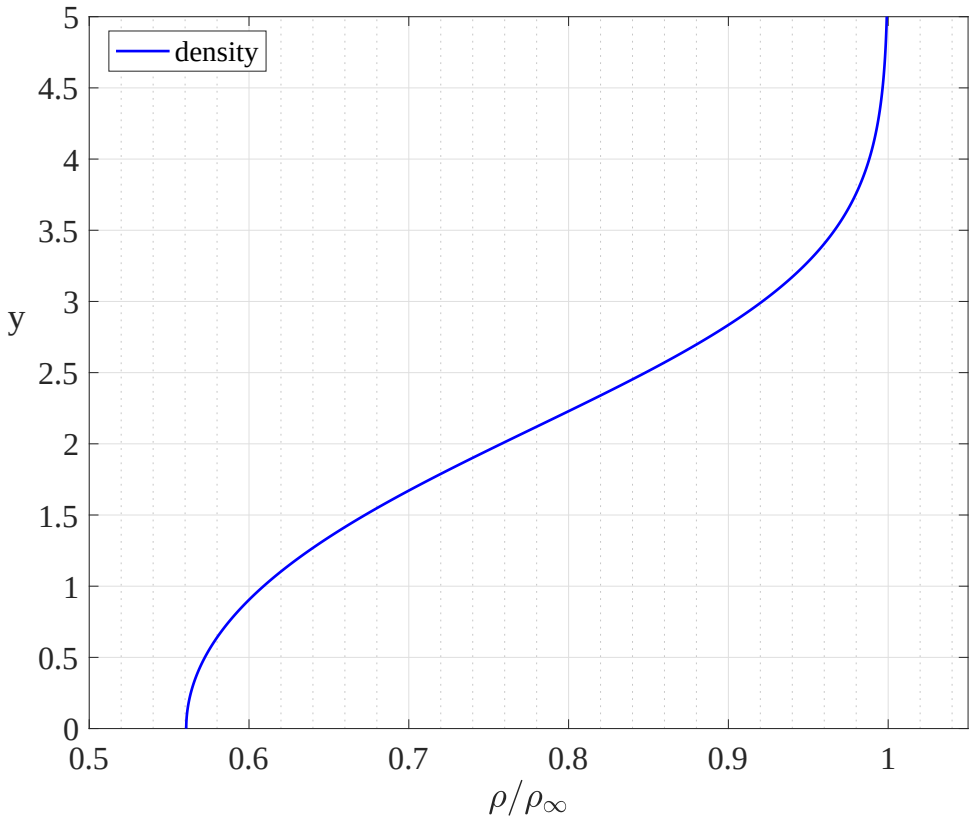

Figure 11: Density profile found having adopted the Blasius solution for temperature profile.

6.2 Upper conditions

The upper boundary of the simulation domain is in contact with the undisturbed flow. This boundary is also interested by the entrance of the shock wave into the domain. The upper boundary has to be split into two regions:

1. Crossing Shock Wave (CSW);
2. undisturbed region Downstream the Shock Wave (DSW).

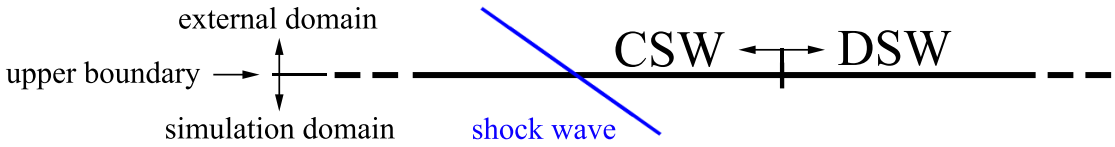

Figure 12: Division of the upper boundary of the simulation domain, the two regions can be distinguished.

Along the CSW the *Rankine-Hugoniot* equations (appendix C) are implemented in order to take into account the variation of the properties due to the jump of the flow across the shock wave. The separation between the two regions is based on the point where the shock wave entries into the domain. This point depends on the angle of the shock wave which is defined with the $\theta - \beta - M$ relation, that is, having fixed the impingement point on the plate and having obtained the β angle from eq.(C.1.1) (known the angle θ of the oblique shock wave generator and the inlet Mach number), the point on the upper domain where the shock wave entries gets defined. Then the location where the change in boundary conditions occurs is taken a little downstream of the shock wave in order to entirely include it.
Finally, in the DSW region the properties of the flow crossing the upper boundary get extrapolated from the domain copying them on the first *ghost node*[3] outside the simulation domain.

6.3 Flat plate conditions

For the lower bounder of the simulation domain, the adiabatic no-slip wall condition is assumed. That means that

$$\left(\frac{\partial T}{\partial y}\right)_{y=0} = 0 \tag{6.3.1}$$

as can be seen in figure 10.
The bottom boundary conditions are defined through the implementation of the *Navier-Stokes Characteristic Boundary Conditions* (NSCBC) which are introduced here below for the general case of a one dimension problem [35], [42].

[3]The ghost nodes are points outside the domain that are needed to execute derivatives on the borders or other calculations like the implementation of boundary conditions.

6.3.1 Navier-Stokes Characteristic Boundary Conditions

Considering a supersonic flow as the case of this work, the "physical" waves (known as ascendant characteristics) cannot ascend from the outlet to the inlet since their propagation velocity is the one of the sound and the flow descend faster, nevertheless the numerical waves, since they are not physical, can do it, going to influence the flow and the solution as well.
In order to minimize the numerical instabilities and the spurious reflections of the characteristics on the boundaries caused by the nature of the resolutive method, accurate boundary conditions must be defined, these conditions are the Navier-Stokes Characteristic Boundary Conditions.
The assumption made is to consider that, limited to the boundary condition, the flow has only the x component, that is

$$\frac{\partial \vec{U}}{\partial t} = -\frac{\partial \vec{F}(\vec{U})}{\partial x} \tag{6.3.2}$$

The system of hyperbolic equations (6.3.2) can be written in a primitive form

$$\frac{\partial \vec{U}}{\partial t} = -\vec{S}\,\frac{\partial \vec{U}}{\partial x} \tag{6.3.3}$$

where

$$\vec{S} = \vec{A}^{-1}\vec{E}\vec{A} \tag{6.3.4}$$

where the rows of $\vec{A}$ are the left eigenvectors of $\vec{S}$, the columns of $\vec{A}^{-1}$ are the right eigenvectors of $\vec{S}$ and $\vec{E}$ is a diagonalized matrix with $\vec{E}_{ii} = e_i$ eigenvalues of $\vec{S}$.
Thus

$$\frac{\partial \vec{U}}{\partial t} = -\vec{A}^{-1}\vec{E}\vec{A}\,\frac{\partial \vec{U}}{\partial x} \tag{6.3.5}$$

Now the outgoing waves (those having $e_i \leq 0$ at $x = x_{min}$ and $e_i \geq 0$ at $x = x_{max}$) are related to informations contained in the domain, so their numerical approximations are stable.
However the incoming waves (those having $e_i > 0$ at $x = x_{min}$ and $e_i < 0$ at $x = x_{max}$) are related to informations external to the domain, so their numerical approximations are unstable since not using external data.
Nevertheless, in common fluid-dynamic problems the flow behaviour at the outer locations is well known, so accurate approximations can be often used in order to minimize reflections of outgoing waves.
These approximations consist in a system of relations referred to an associated *Local One-Dimensional Inviscid* (LODI) problem whose study allows to establish the values of the amplitude variations of the waves crossing the boundary in the viscous multidimensional case.
Then defining the vector of characteristic waves

$$\vec{\mathscr{L}}(\vec{U}) = \vec{E}\vec{A}\,\frac{\partial \vec{U}}{\partial x} \tag{6.3.6}$$

the equation (6.3.5) becomes

$$\frac{\partial \vec{U}}{\partial t} = -\vec{A}^{-1}\vec{\mathscr{L}}(\vec{U}) \tag{6.3.7}$$

with

$$\begin{aligned}
\mathscr{L}_1 &= e_1 \left(\frac{\partial p}{\partial x} - \rho c \frac{\partial u}{\partial x} \right) \\
\mathscr{L}_2 &= e_2 \left(c^2 \frac{\partial \rho}{\partial x} - \frac{\partial p}{\partial x} \right) \\
\mathscr{L}_3 &= e_3 \frac{\partial v}{\partial x} \\
\mathscr{L}_4 &= e_4 \frac{\partial w}{\partial x} \\
\mathscr{L}_5 &= e_5 \left(\frac{\partial p}{\partial x} + \rho c \frac{\partial u}{\partial x} \right)
\end{aligned} \tag{6.3.8}$$

Depending on $\vec{U}$ the LODI system assumes different forms, in the case of this thesis it is

$$\begin{aligned}
\frac{\partial \rho}{\partial t} &= -d_1 \\
\frac{\partial \rho u}{\partial t} &= -u\, d_1 - \rho\, d_3 \\
\frac{\partial \rho v}{\partial t} &= -v\, d_1 - \rho\, d_4 \\
\frac{\partial \rho w}{\partial t} &= -w\, d_1 - \rho\, d_5 \\
\frac{\partial \rho E}{\partial t} &= -\frac{1}{2} \left(u^2 + v^2 + w^2 \right) d_1 - \frac{d_1}{\gamma - 1} - \rho \left(u\, d_3 + v\, d_4 + w\, d_5 \right)
\end{aligned} \tag{6.3.9}$$

where the presence of the amplitude variations of the waves (e_i) is explicated through the functions d_i

$$\begin{aligned}
d_1 &= \frac{1}{c^2} \left[\mathscr{L}_2 + \frac{1}{2} \left(\mathscr{L}_1 + \mathscr{L}_5 \right) \right] \\
d_2 &= \frac{1}{2} \left(\mathscr{L}_1 + \mathscr{L}_5 \right) \\
d_3 &= -\frac{1}{2\, \rho\, c} \left(\mathscr{L}_1 - \mathscr{L}_5 \right) \\
d_4 &= \mathscr{L}_3 \\
d_5 &= \mathscr{L}_4
\end{aligned} \tag{6.3.10}$$

in which $\mathscr{L}_i = \mathscr{L}_i(e_i)$.
Then the application of characteristic conditions to different cases is done by adapting the $\vec{\mathscr{L}}$ vector that describes characteristic waves.

In the case of the adiabatic no-slip wall the velocities on the plate are zeros and the heat flux is zero either, then eq.(6.3.9.b) gives $\rho\, d_3 = 0 \Rightarrow d_3 = 0$ so eq.(6.3.10.c) gives $\mathscr{L}_1 = \mathscr{L}_5$ also $\mathscr{L}_2 = \mathscr{L}_3 = \mathscr{L}_4 = 0$. By these results the density and the total energy can be obtained by integration.
Attention must be paid since the adiabatic condition is obtained by imposing the wall temperature to the one of *recovery* (equation (6.1.21)), thus for an undisturbed flow over the flat plate the adiabaticity is achieved, while in presence of an external disturbance that varies the temperature of the flow such as the SWBLI, a heat exchange occurs so as to keep the wall temperature equal to the recovery one.

6.4 Outlet conditions

For the outlet conditions the most common used is the Neumann one, which is a "weaker" condition than the one of Dirichlet. This last condition specifies the exact values of the properties on the boundaries of the domain, while the Neumann condition consists in the imposition of the derivative of the properties of the flow in respect to the stream-wise coordinate.
Usually the convective derivative normal to the boundary is set equal to zero which means that the transported properties follow the stream-wise direction to leave the domain.

$$\frac{\partial (\cdot)}{\partial x} = 0 \tag{6.4.1}$$

Another choice could be to adopt the Navier-Stokes characteristic boundary conditions described in sec.6.3.1 in order to reduce numerical instabilities.

7 Model validation

The program must be validated. A popular author for validations is G. Degrez *et alia* (1987) [11]. Usually validations in this topic regard the overlapping of specific graphs, that means that there are certain settings of the simulation that must coincide to those used by the reference one.
In particular:

- inlet Mach number: $M_\infty = 2.15$
- wedge angle: $\theta = 3.75°$
- impingement Reynolds number: $Re_{x_{sh}} = 10^5$

that's because the recirculating bubble dynamic strongly depends on the intensity of the shock wave and the viscosity of the flow in the impingement location.
In section 6.1 is said that the inlet conditions are functions that are obtained by integration in an unidimensional domain. This domain is arbitrary thus the results obtained are relative to a generic boundary layer thickness, i.e. $\delta \sim 4.91$ for the Blasius solution. In practical terms though, the latter increases along x as stated by equation 2.1.3 and also the abscissa Reynolds number do so as can be seen in equation 2.1.2. That means that in order to obtain a certain Reynolds number in correspondence of the impingement location and having set a certain distance of evolution of the boundary layer between the inlet and the impingement point $L = x_{sh} - x_{inlet}$, it is necessary to set a proper Reynolds number and a proper boundary layer thickness in correspondence of the inlet location. The latter, having set L, is not arbitrary since it depends on the scale factor of the system. Said that the solutions for the inlet conditions have to be interpolated on an adequate unidimensional domain.
As said the validation consists in the overlapping of some graphs, but both the physics of the recirculating bubble and the mathematics that describes it are rather delicate, i.e. little mathematical approximations are connected to appreciable physical differences. Once the boundary conditions are well posed and the numerical stabilities of the solver are achieved, the major factor that determines the shape of the recirculating bubble is the order of accuracy of the model adopted for the solver. In particular in Degrez *et al* a $1st$ order[4] central differences method is employed while in the present thesis a $6th$ order one is used. This foreshadows that the graphs won't be exactly overlapped in the region of the interaction, but the model will be considered validated if the trend obtained will be coherent with the trend expected for a higher order model. Then a second author is taken into account in the validation: A. Lerat *et alia* (2001) [22] that compared the results obtained from a $2nd$ order and a $3rd$ order model. In this way the correct behaviour of the interaction region can be predicted.

The properties that get compared are the wall pressure trend in section 7.1 and the skin friction in section 7.2.
Then in section 7.3 some velocity profiles will be pointed out in some sections of the domain corresponding to reference positions also cited by Degrez *et al.*

[4] the order of accuracy attributed to a model is the one adopted in the discretization of convective terms of the Navier Stokes equations. Nevertheless the WENO scheme and the discretization of dissipative terms use or may use different orders of accuracy, as for the case of Degrez which used a $4th$ order of accuracy for the discretization of dissipative terms.

7.1 Wall pressure

The first property taken into account is the pressure trend on the surface of the flat plate.
Its behaviour in the SWBLI phenomenon is characterized by an initial almost-plateau in the region upstream the interaction where the shock wave still doesn't show its effects, then there is an initial rise, i.e. an adverse pressure gradient, in the region where the compression fan takes place (b in figure 3) followed by a second rise downstream the *nominal* impingement location (the point where the shock wave would intersect the flat plate in the case of perfectly inviscid fluid). After that the pressure reaches a second almost-plateau where the interaction vanished and the pressure reaches the value corresponding to the one determined by Rankine-Hugoniot equations.
In the following figure the pressure trend is adimensionalized by the minimum pressure along x, which is the one just before the first rise of pressure.
Also the abscissa is adimensionalized in respect of x_{sh}, which is the point where the nominal impingement is.

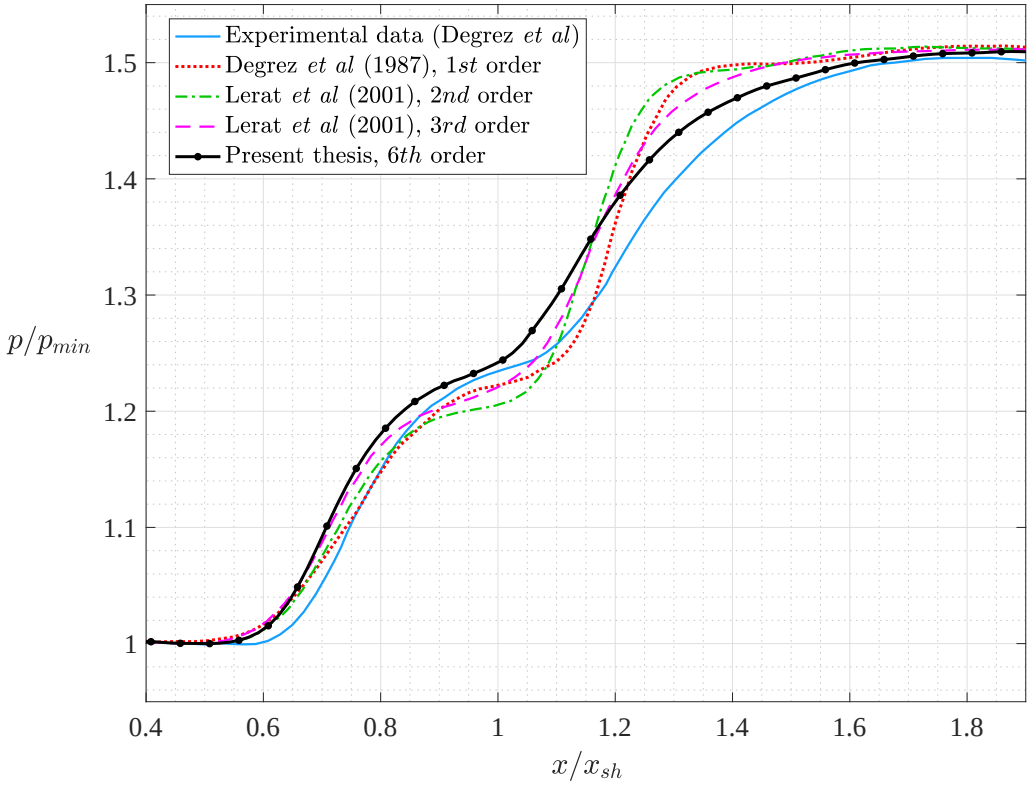

Figure 13: Wall pressure trend comparison between Degrez et al simulation and those of Lerat et al. In graph has been also reported the experimental data obtained by Degrez' experiment.

From figure 13 it can be seen that the pressure trend of the present $6th$ order model lays within an acceptable error band.

The setting of the wedge angle and the inlet Mach number determine the intensity of the shock wave, this fact has two intuitive influences in this graph: firstly on the dimensions of the interaction region in terms of width and secondly on the adiabatic compression factor, i.e. the pressure value reached downstream the interaction region. The first one is also influenced by the order of the resolution model, but the second one is almost-univocal since it is principally related to macroscopic effects and only partially on the behaviour of the SWBLI.
In figure 13 can be also noticed the trend of behaviours from low order models to high order models: in low orders the second rise of pressure produces an overshoot that is not found in high order models, the $6th$ order model presents a coherent behaviour of the flow in that region considering Lerat's simulations.

7.2 Skin friction

The second property compared is the skin friction along the plate. This property is very meaningful in this topic since it describes the dynamics of the flow in two aspects.
The first one is the mere representation of the skin friction giving informations on the viscous shear stress along the plate. The second one can be clearly seen by the analytical definition of the skin friction.
Let's consider the following relation

$$c_f = \frac{\tau_W}{\frac{1}{2}\,\rho\, U_\infty^2} \tag{7.2.1}$$

where τ_w is the viscous shear stress along the wall, thus the skin friction is proportional to the latter. For fluids the shear stress is a function of the *strain rate* $\mathrm{d}\xi/\mathrm{d}t$, in particular, for Newtonian fluids, through the *Newton's law*

$$\tau_W = \mu \frac{\mathrm{d}\xi}{\mathrm{d}t} \tag{7.2.2}$$

where μ is the *dynamic viscosity* which depends on the kind of fluid involved.
Equation (7.2.2) shows that the deformation of the fluid in its motion along the stream-wise direction causes a resulting tension on the plate which is proportional to the rate of deformation through the viscosity of the fluid itself.
The strain rate can be written as

$$\frac{\mathrm{d}\xi}{\mathrm{d}t} = \frac{u\,(y+\delta y) - u\,(y)}{\delta y} \tag{7.2.3}$$

which for small δy gives

$$\frac{\mathrm{d}\xi}{\mathrm{d}t} = \frac{\partial u\,(y)}{\partial y} \tag{7.2.4}$$

thus

$$\tau = \mu \frac{\partial u}{\partial y} \tag{7.2.5}$$

On the wall it can be written as

$$\tau_W = \mu \left(\frac{\partial u}{\partial y}\right)_{y=0} \tag{7.2.6}$$

which is a tension in the same direction of the flow, i.e. a *viscous shear force* per unit of area. Substituing (7.2.6) into (7.2.1) results in

$$c_f = \frac{2\,\mu}{\rho\,U_\infty^2}\left(\frac{\partial u}{\partial y}\right)_{y=0} \tag{7.2.7}$$

as can be seen in equation (7.2.7) the skin friction directly depends on the derivative of the velocity profile at the wall, this gives informations on the evolution of the velocity profiles in the stream-wise direction, which can be used to validate the model since the behaviour of the flow in the region outside the interaction one must be the one of the undisturbed flow over the flat plate, so it has to be overlapped to the one of reference, and it also clearly says where the recirculating bubble is located, i.e. the separation and reattachment points. The latter causes the skin friction to be a very handy tool for the analysis of the shape and behaviour of the recirculating bubble.

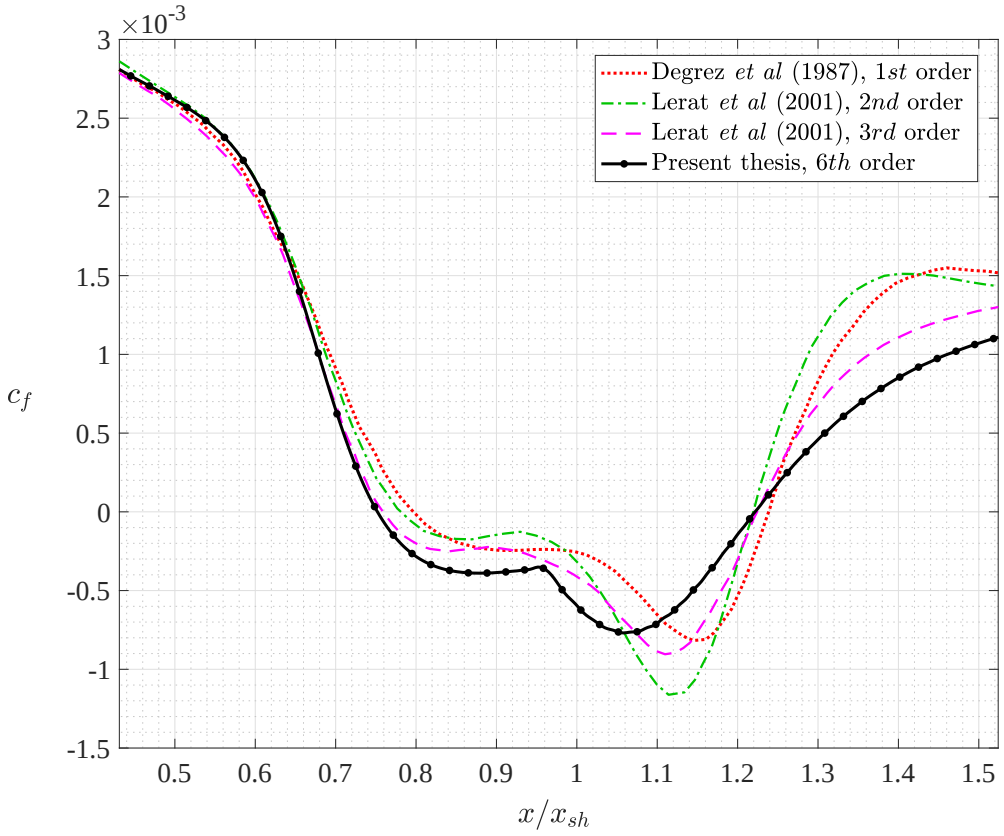

Figure 14: Skin friction on the wall along stream-wise direction.

In the skin friction graph (figure 14) results evident the strong dependency of the physical results from the order adopted in the mathematical model. As for the pressure, also for the skin friction, low order models see an overshoot of the property in correspondence of the junction with the undisturbed region downstream the SWBLI, which means that, referring at equation (7.2.7), the velocity profile near the wall is flatter, thus the boundary layer there is thinner. Moreover low

order models obtain a lower skin friction value downstream the nominal impingement, that means that the recirculation is stronger, i.e. the flow has a more negative component near the wall.
In the present thesis the separation point is situated at $x/x_{sh} = 0.7652$, while the reattachment point lays at $x/x_{sh} = 1.2349$, with a width of the separation region of $width = 0.4697$. The minimum value of the skin friction is $c_{f_{min}} = -7.3116E - 04$.
Figure 14 shows also that the SWBLI causes an inversion of the shear stress along the plate in the region of the recirculation with a fluctuation of its magnitude along the stream-wise direction.

7.3 Velocity profiles

Considering an undisturbed flow, as discussed in section 6.1.1 the shape of the velocity profile is determined by its derivative in $y = 0$. That means that the skin friction is strongly related to the behaviour of the velocity profiles.
In this section are reported velocity profiles corresponding to the three different sections of the flow in the stream-wise direction proposed by Degrez *et al*:

- $x/x_{sh} = 0.6$;
- $x/x_{sh} = 0.95$;
- $x/x_{sh} = 1.6$.

The choice to visualize the velocity profiles in these section is motivated by the fact that the first one is in a position upstream the SWBLI, the second one shows the recirculation and the third one is downstream the SWBLI.

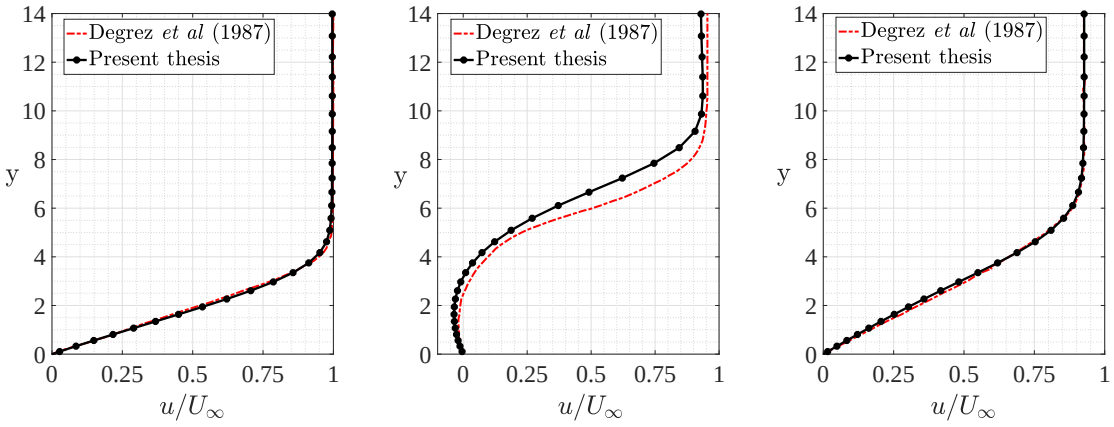

(a) $x/x_{sh} = 0.6$ *(b)* $x/x_{sh} = 0.95$ *(c)* $x/x_{sh} = 1.6$

Figure 15: Velocity profiles in different sections

By graphs 15a and 15c can be noticed that as expected the boundary layer thickens along x, while in correspondence of the recirculating bubble (figure 15b) the boundary layer gets even higher due to the interaction with the shock wave (see fig. 3).

8 Analysis of SWBLI behaviour

In practical cases SWBLIs take place in different situations with different boundary conditions regarding different fluids. For this reason specific studies of this topic have to be applied to the related case in order to obtain accurate results. The work pursued in this thesis wants to be as general as possible in order to give qualitative informations about the problem and to provide basic engineering tools to permit a further study on specific situations that may be of interest.
One of the most general analysis that can be carried out is the study of the SWBLI behaviour for different Mach numbers. This condition can be verified not only in different systems, but also within the same one, for example the blades of a transonic turbo-machinery that increases its rotational speed are interested by a relative Mach number that increases along time, leading to different SWBLIs.
The Mach number required for the validation (section 7) is $M = 2.15$. Additional Mach numbers valued are $M = 2.50$, $M = 2.75$, $M = 3.00$, $M = 3.50$. In this way a qualitative dependence of the SWBLI phenomenon in respect to the Mach number can be observed. This dependence is related to the distinct intensities of the oblique shock waves generated by different Mach numbers.

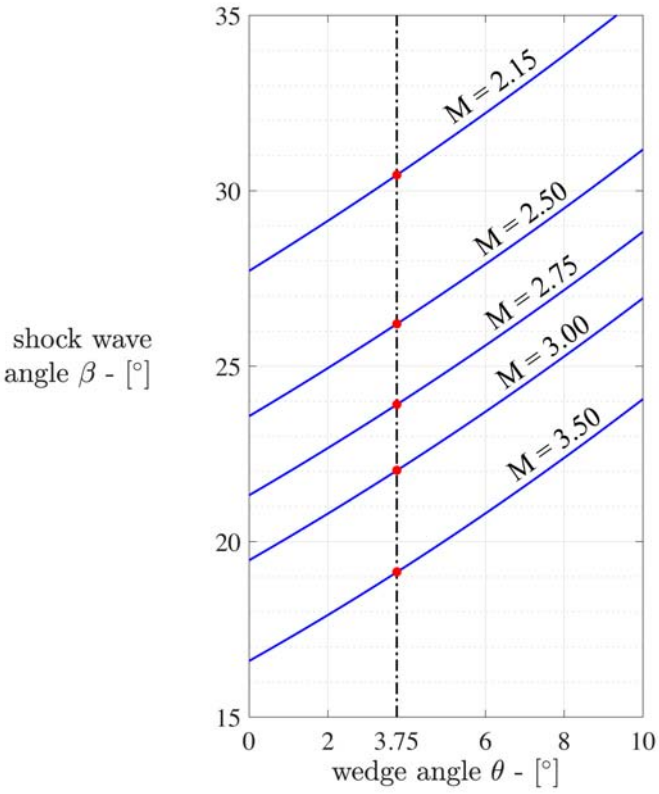

Figure 16: Portion of the $\theta - \beta - M$ graph (appendix C.1) representing oblique shock wave angles corresponding to Mach numbers under study (blue lines) having fixed the wedge angle at 3.75 degrees.

As can be seen in figure 16, higher Mach numbers generate shock waves having lower angles in respect to the stream direction (β) leading to weaker shock waves (see appendix C.1).
In particular

Table 1: Oblique shock wave angle values associated to Mach numbers under study with fixed wedge angle.

M	θ	β
2.15	3.75°	30.75°
2.50	3.75°	26.41°
2.75	3.75°	24.07°
3.00	3.75°	22.16°
3.50	3.75°	19.23°

Firstly in this section are displayed some data fields (sec. 8.1).
Secondly, informations given in this section regard issues presented in the validation section (sec. 8.2-8.4), however the study on the velocities is focused on the recirculation region. Furthermore additional studies about the thermal behaviour of the boundary layer are carried out (sec. 8.5).

8.1 Data fields

In this section are shown several data fields for the different cases. This allows to visualize the macroscopic behaviour of the SWBLI as a function of the Mach number given at the inlet.
Firstly are reported the velocity fields (8.1.1), then the pressure (8.1.2), density (8.1.3) and temperature (8.1.4) fields are following.

8.1.1 Velocity fields

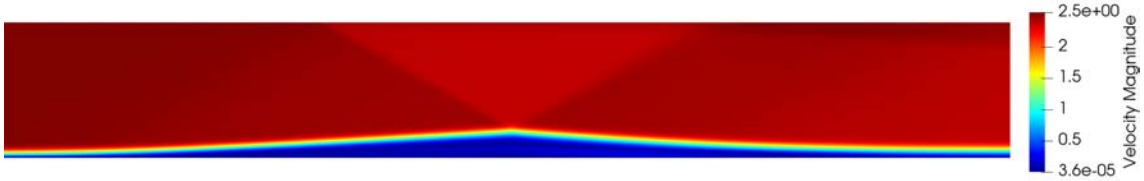

(a) $Mach = 2.15$

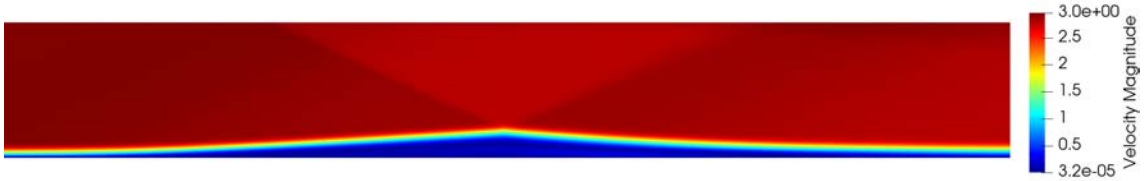

(b) $Mach = 2.50$

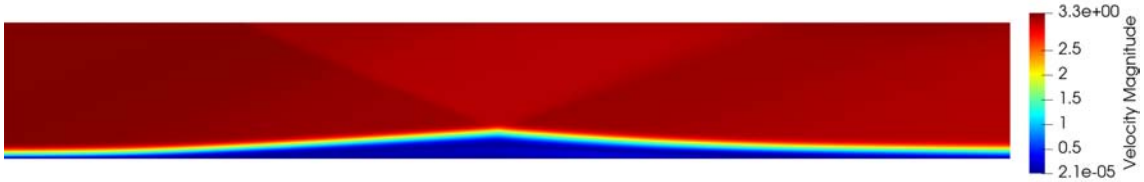

(c) $Mach = 2.75$

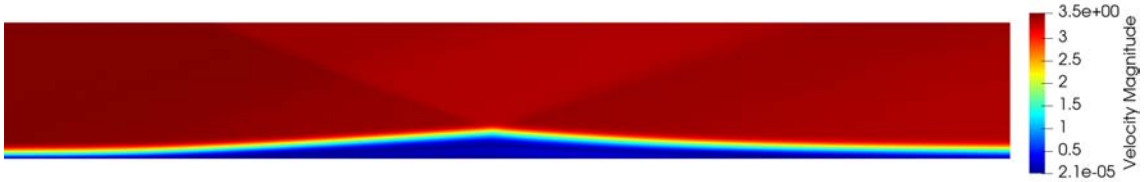

(d) $Mach = 3.00$

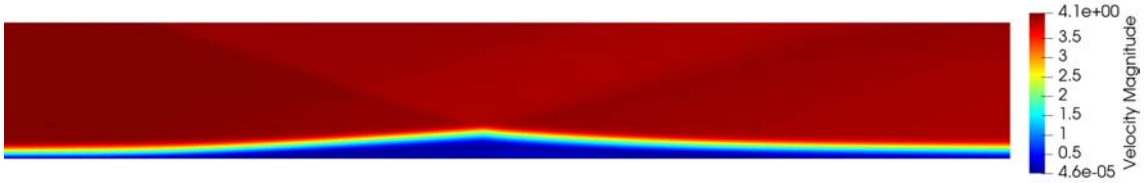

(e) $Mach = 3.50$

Figure 17: Velocity fields for different Mach numbers.

8.1.2 Pressure fields

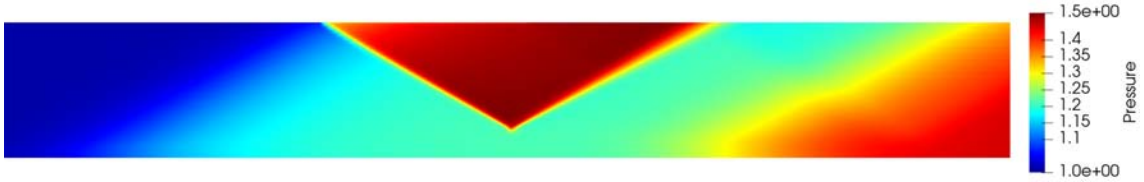

(a) $Mach = 2.15$

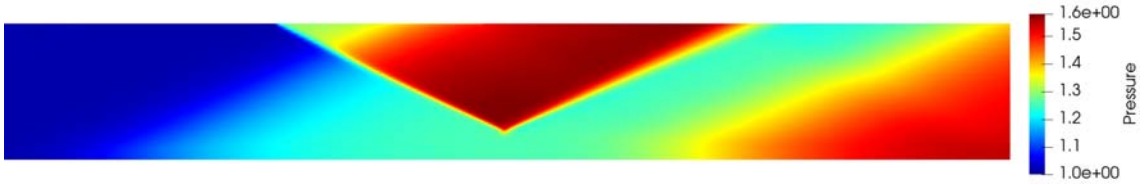

(b) $Mach = 2.50$

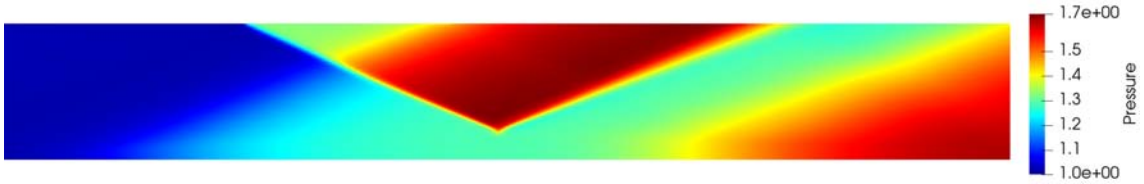

(c) $Mach = 2.75$

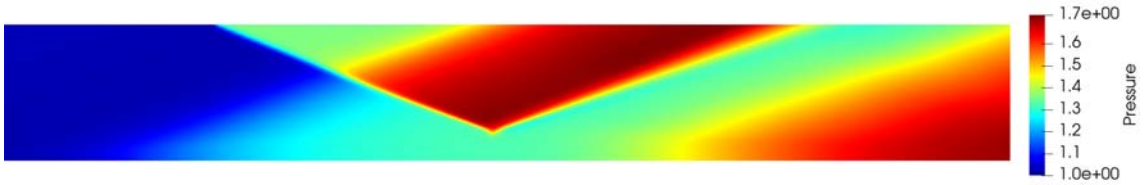

(d) $Mach = 3.00$

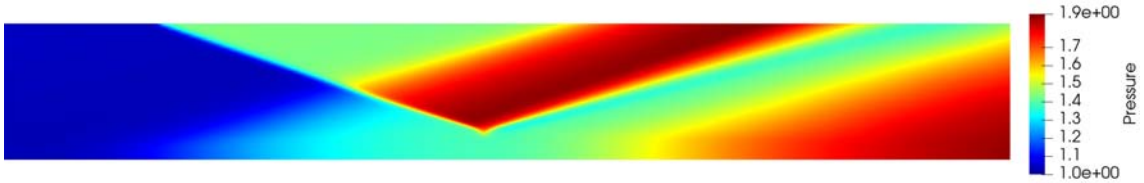

(e) $Mach = 3.50$

Figure 18: Pressure fields for different Mach numbers.

8.1.3 Density fields

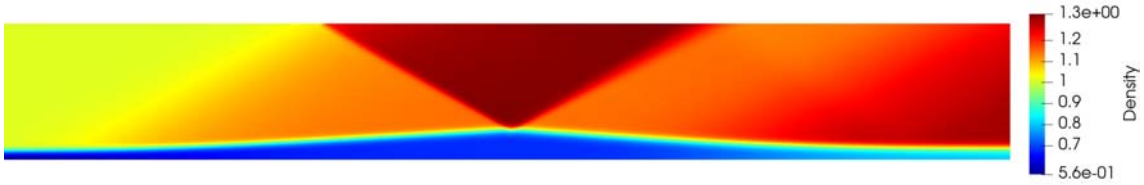

(a) $Mach = 2.15$

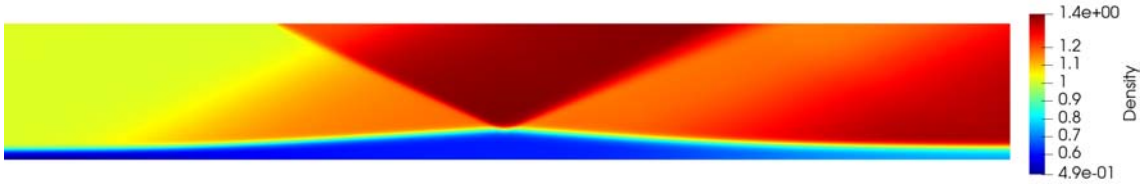

(b) $Mach = 2.50$

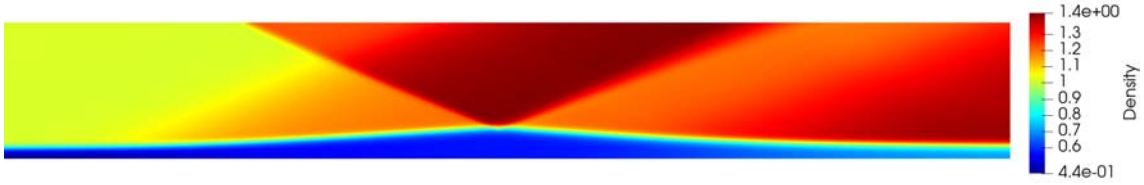

(c) $Mach = 2.75$

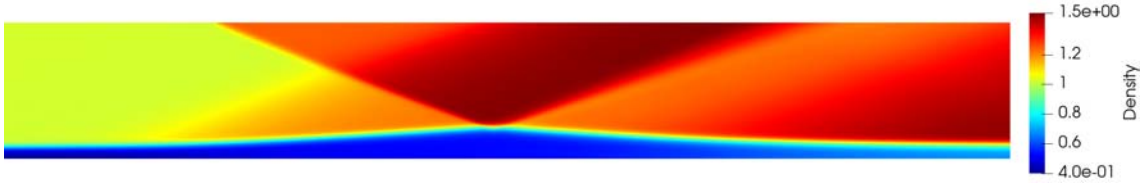

(d) $Mach = 3.00$

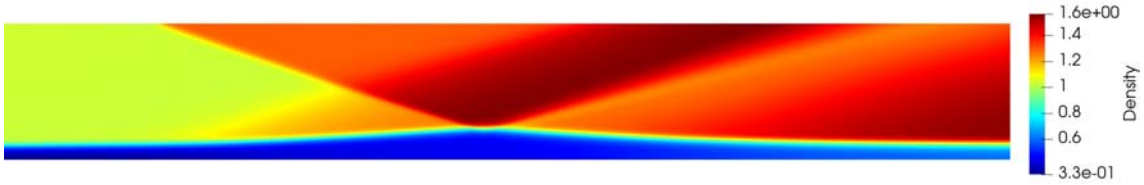

(e) $Mach = 3.50$

Figure 19: Density fields for different Mach numbers.

8.1.4 Temperature fields

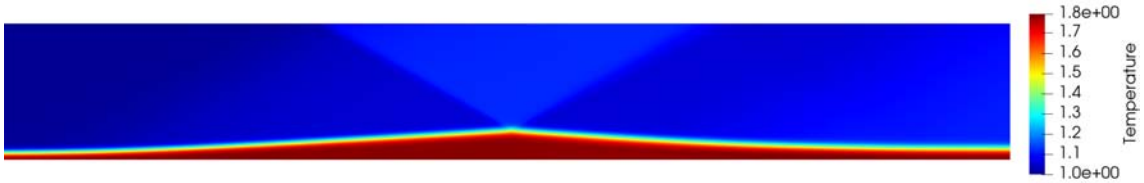

(a) $Mach = 2.15$

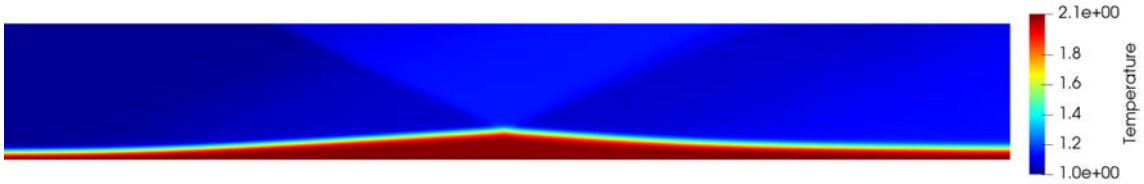

(b) $Mach = 2.50$

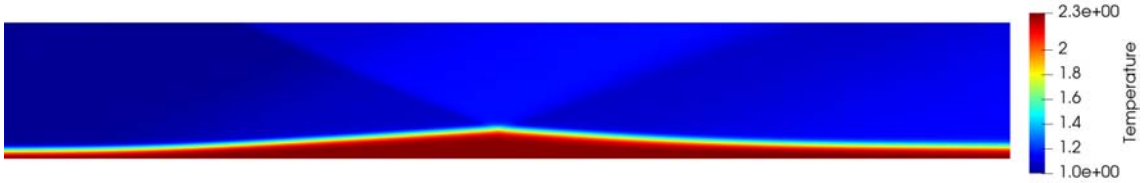

(c) $Mach = 2.75$

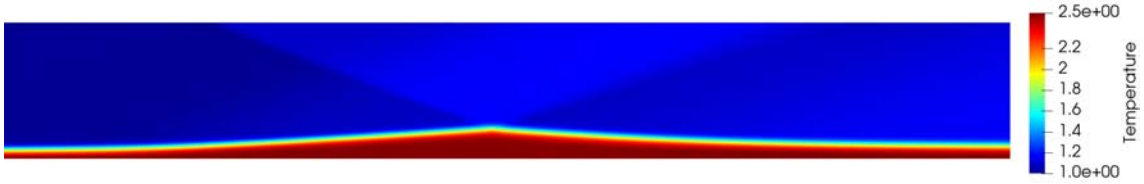

(d) $Mach = 3.00$

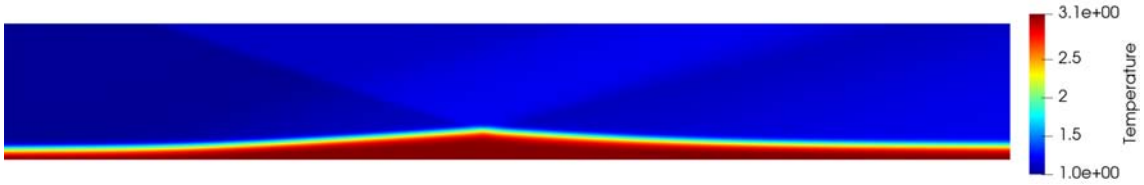

(e) $Mach = 3.50$

Figure 20: Temperature fields for different Mach numbers.

8.2 Wall pressure for several Mach numbers

As said in section 2.2 the static pressure across a shock wave gets increased. By looking at equation (C.0.11) the higher the upstream Mach number is, the more the static pressure gets increased.

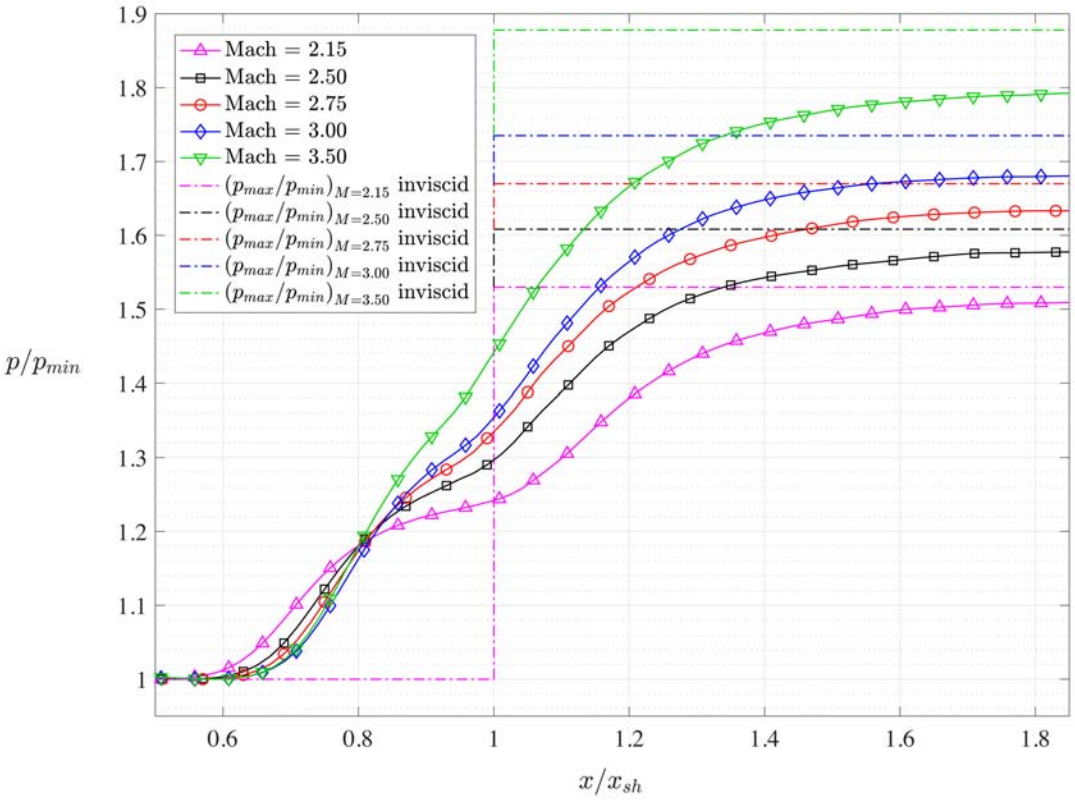

Figure 21: Wall pressure trends corresponding to different Mach numbers. The graph also shows the maximum pressures obtained in the perfectly inviscid case (absent boundary layer) which are the dash-dotted lines.

As can be noticed by looking at figure 21 the maximum values of the pressure downstream the SWBLI are lower than those obtained in the case without the presence of the boundary layer. This is due to the fact that the dissipative effect in the SWBLI is proportional to the Mach number. In particular this loss is caused by the presence of the compression fan upstream of the recirculating bubble that deviates the flow.

In the following table can be observed the reference values for the pressures

Table 2: Maximum values of pressure ratio along the plate for different Mach numbers. The last column contains ratios between the 2nd and 3rd columns.

M	p_{max}/p_{min}	$p^{inv.}_{max}/p^{inv.}_{min}$	$p_{max}/p^{inv.}_{max}$
2.15	1.5096	1.5300	0.9867
2.50	1.5778	1.6083	0.9812
2.75	1.6332	1.6699	0.9780
3.00	1.6805	1.7350	0.9686
3.50	1.7961	1.8778	0.9565

From table 2 can be confirmed that the attenuation of the compressive effect due to the presence of the viscosity is higher as the Mach number increases.

8.3 Skin friction for several Mach numbers

The skin friction highlights the dimensions of the recirculating bubble, thus it is very meaningful in the study of the dependence between the SWBLI and the Mach number.
By looking at table 1 it can be seen that in the region of weak shocks, the higher the Mach number, the weaker the shock wave is. That means that the recirculating bubble is expected to be narrower for high Mach numbers.

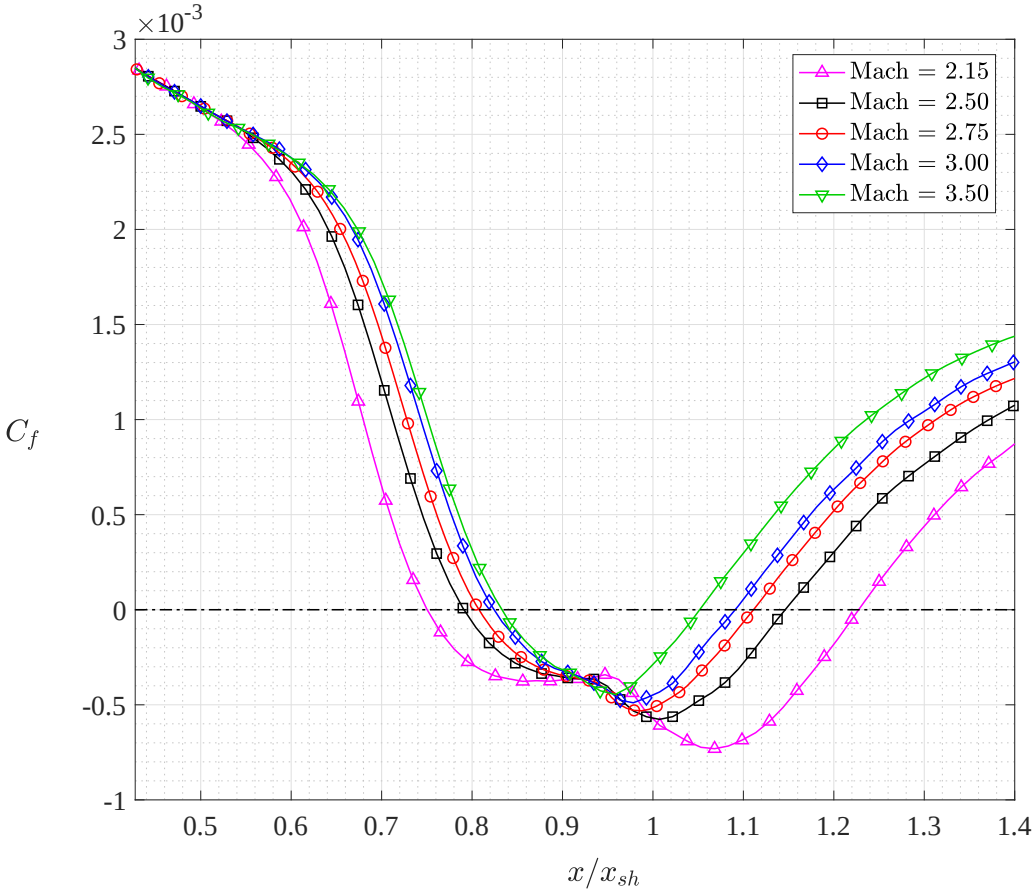

Figure 22: Skin friction trends along the plate for several Mach numbers.

As can be seen in figure 22 and in figure 23 the width of the SWBLI is strongly related to the Mach number, i.e. to the shock wave intensity.
Moreover the minimum value of the skin friction in the SWBLI depends on the Mach number.
Here below is reported a table containing values extracted of separation and reattachment points for each case. These points are identified where the skin friction changes in sign.

Table 3: Positions of detachment and reattachment points at various Mach

M	x_{det}/x_{sh}	x_{reatt}/x_{sh}
2.15	0.7652	1.2349
2.50	0.8043	1.1522
2.75	0.8125	1.1125
3.00	0.8333	1.0942
3.50	0.8417	1.0583

As said, the lower the Mach number, the further from $x/x_{sh} = 1.0$ the two points get. Thus the width of the recirculating bubble can be determined as a function of Mach. One must pay attention in not confusing the width of the recirculating bubble from the width of the SWBLI: the first one corresponds to the region where the velocity inside the boundary layer inverts its direction, and it is situated between the detachment and the reattachment points, the second one is the portion of boundary layer along the stream-wise direction affected by the presence of the shock wave.

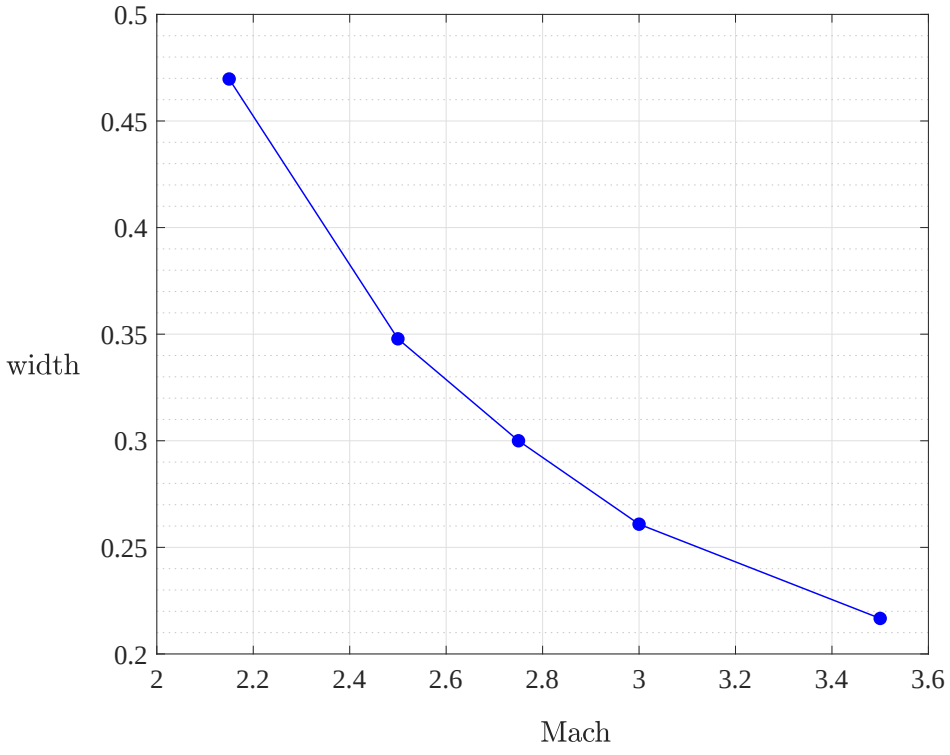

Figure 23: Width of the recirculating bubble for several Mach numbers.

Another important property of the SWBLI is the already-mentioned minimum value of the skin friction reached. This gives informations about the highest negative-derivative of the velocity profiles along the SWBLI, i.e. the entity of the recirculation.
In the following section (sec. 8.4) velocity profiles are presented, thus the relation between the Mach number and the recirculation can be seen.

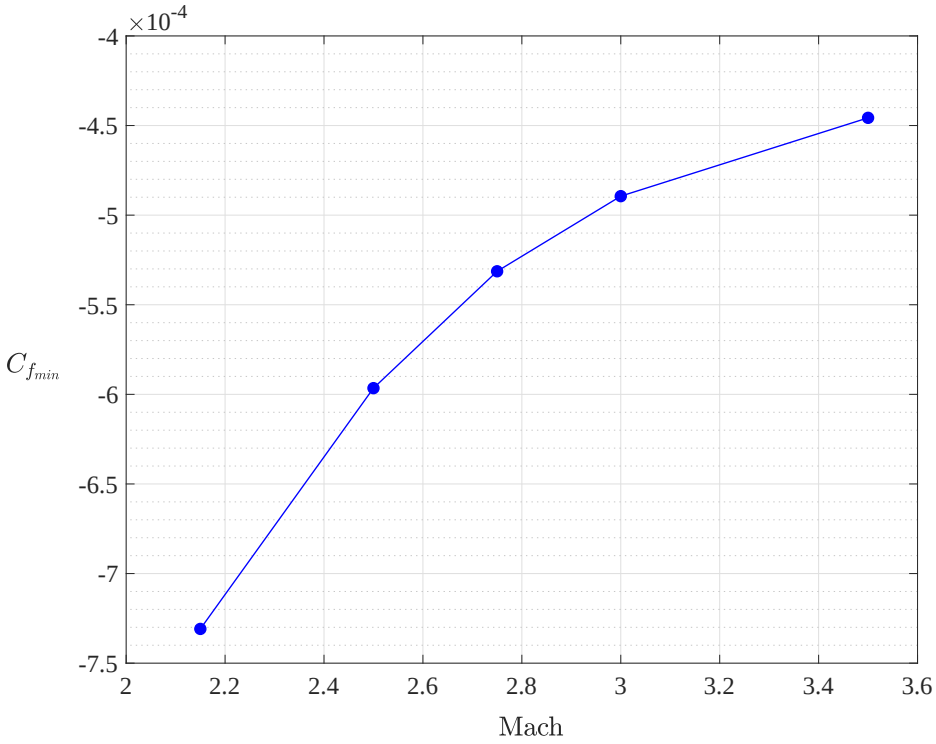

Figure 24: Lowest values of the skin friction along the SWBLI for several Mach numbers.

Figures 23 and 24 show that the width of the recirculating bubble and the $C_{f_{min}}$ have a stronger dependence on lower Mach numbers, this is due to the fact that, for low values of Mach, a little variation in these reserves a higher change of the shock wave angle and so of its intensity. That means that lower Mach numbers give a stronger and wider inversion of the shear stress along the SWBLI with consequently a higher fluctuation entity.

8.4 Recirculation for several Mach numbers

In the present section the velocity profiles in the location where the skin friction reaches its minimum value are compared between the different cases studied. These positions are meaningful since there the maximum shear stress on the plate occurs. Nevertheless the global minimum of the velocity do not correspond to these locations but it is situated in a section slightly upstream of the latter.
Furthermore the comparison between the global minimum values of the velocity and the local minimum velocity relatively to sections corresponding to the minimum skin friction will be presented, then velocity fields of the recirculation will be pointed out.

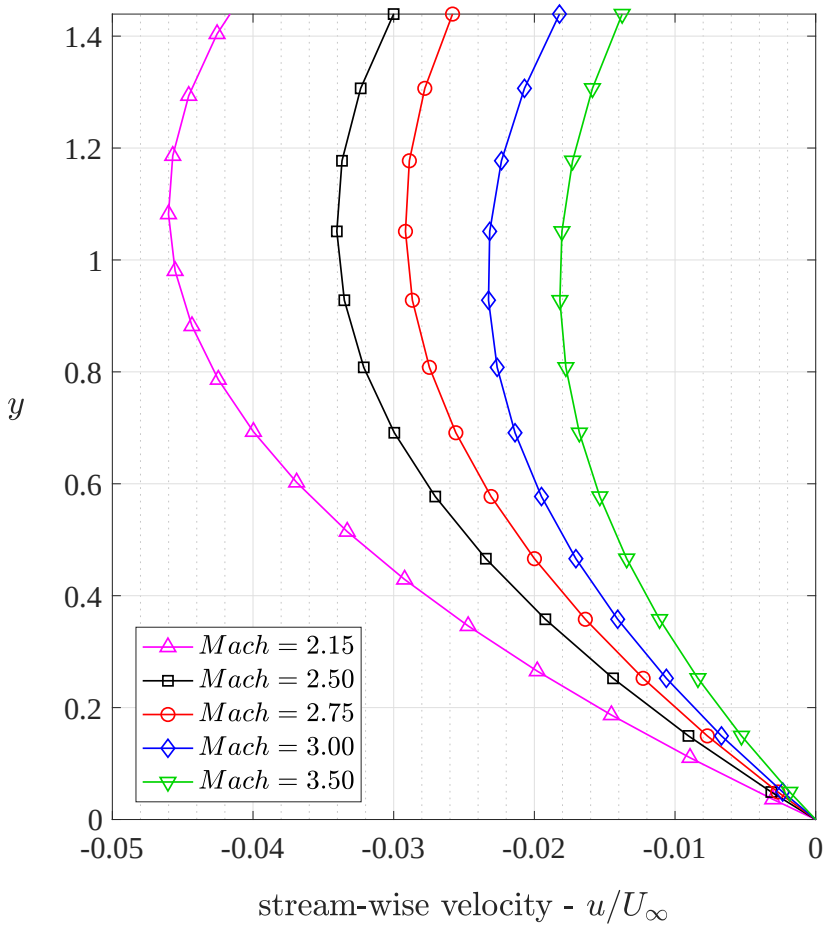

Figure 25: Region near the wall of velocity profiles for different Mach numbers of the flow in correspondence of the minimum skin friction location. These profiles are non-dimensionalized to the relative undisturbed upstream velocity.

In figure 25 are displayed the velocity profiles relatively to the corresponding upstream undisturbed velocity and it can be seen that the higher the Mach number, the lower the magnitude of the slope of the profile at the wall is.
This result is strictly related to the global minimum value of the velocity

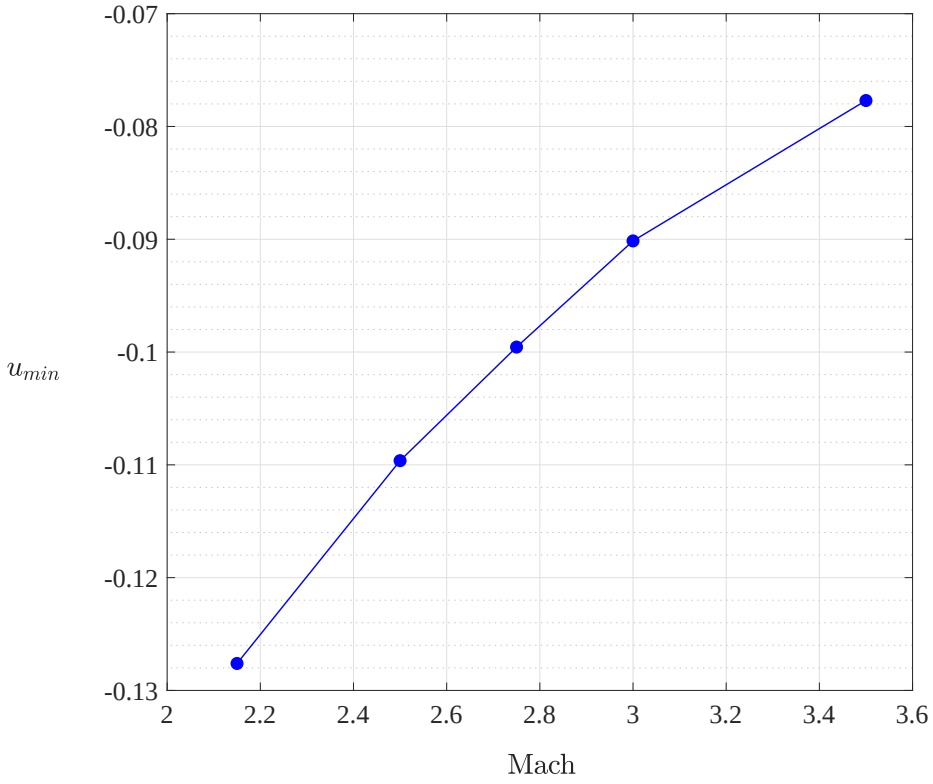

Figure 26: Minimum values of the stream-wise velocity along the SWBLI for different Mach numbers.

As can be noticed the figure above is rather similar to the one of the minimum skin friction (figure 24).

In the following table the numeric values of the global and local[5] minimum velocities are shown

Table 4: Minimum values of the stream-wise component of the velocity in the simulation domain.

M	u_{min}^{global}	$u_{min}^{C_{f_{min}}}$
2.15	-0.1276	-0.1170
2.50	-0.1096	-0.1006
2.75	-0.0996	-0.0918
3.00	-0.0911	-0.0827
3.50	-0.0777	-0.0754

In the table below are reported the dimensions in terms of height and width of the reflux regions of figure 27. The latter has been rescaled along the x coordinate in order to better visualize the reflux behaviour.

Table 5: Dimensions of the reflux regions of the different cases studied.

M	*width*	*height*
2.15	0.4697	0.0122
2.50	0.3478	0.0101
2.75	0.3	0.009
3.00	0.2609	0.0083
3.50	0.2167	0.0076

[5] in sections corresponding to the minimum skin friction.

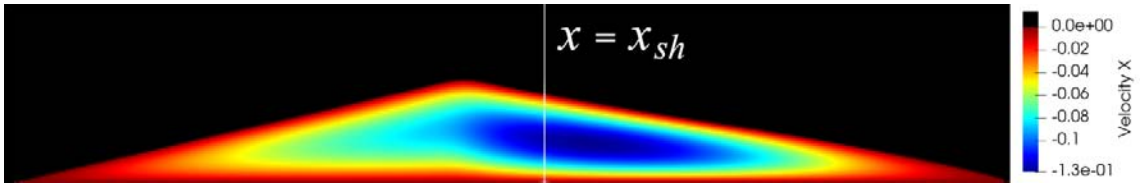

(a) $Mach = 2.15$

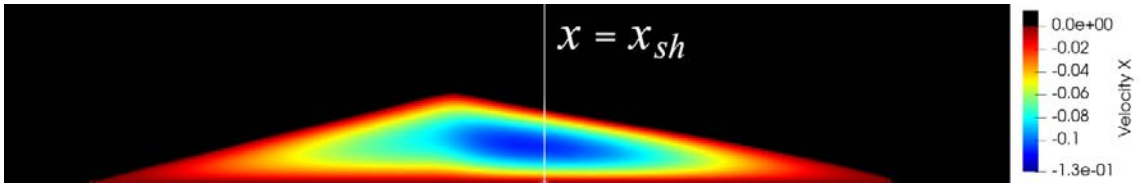

(b) $Mach = 2.50$

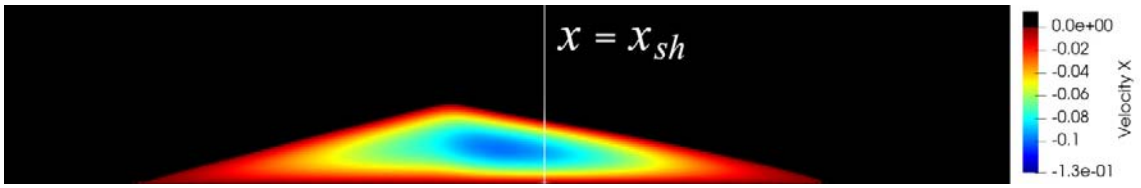

(c) $Mach = 2.75$

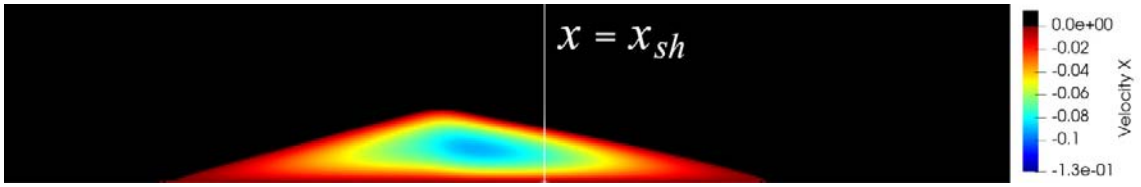

(d) $Mach = 3.00$

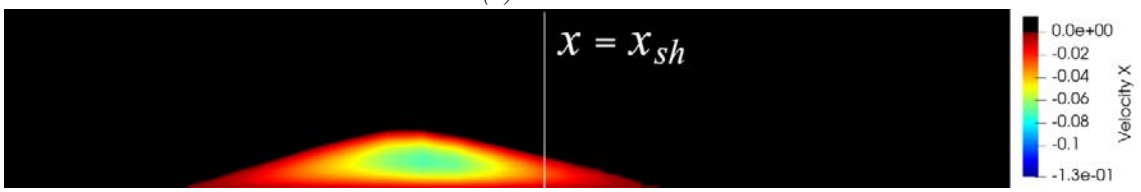

(e) $Mach = 3.50$

Figure 27: Fields of the regions of the domain where the stream-wise component of the velocity becomes negative for different Mach numbers. The images above are rescaled along x in order to better visualize the reflux behaviour.

From the figures above can be noticed that the regions inside of the recirculating bubbles where the stream-wise velocity reaches its minimum values (blue zones) are developed obliquely from north-west to south-east with the global minimum value situated in the center of them, and since the sections where the minimum value of the skin friction are where these regions are the nearest to the plate, the global minimum of the velocity is upstream of the latter sections.

8.5 Heat transfer for several Mach numbers

Another important result of the SWBLI is the heating of the flow near the plate. This is represented by the conversion of kinetic energy into thermal caused by the dynamics of the shock waves that interact with the boundary layer, i.e. by the adiabatic compressions.
As said in section 6.3, the boundary condition set is the temperature of the plate which is the one that guarantees the adiabaticity of the undisturbed flow over the flat plate, i.e. the recovery temperature.
However immediately downstream of the inlet, an acoustic discontinuity deviates the temperature from the recovery one. The presence of this discontinuity is due to the mathematical approximations assumed in the implementation of the physical model, in order to adapt the flow to be coherent with the correct compressible one. That means that a little background heat transfer will be present along the plate.
Said that, the SWBLI heathens the boundary layer in the impingement location causing little gradients of the temperature profile near the wall, i.e. heat transfer with the plate.
When the temperature of the flow increases, the heat gets outside of the system, so it will be considered negative.
In order to obtain informations about the heathen of the flow along the plate, the heat transfer is displayed stream-wise for $y = 0$.
The latter is given by the *Fourier law*

$$q = -k \left(\frac{\partial T}{\partial y} \right)_{y=0} \tag{8.5.1}$$

where k is the thermal conductivity of the flow in correspondence of $y = 0$.
This property of the flow depends on the local viscosity which depends on the temperature trend. However on the plate the constant recovery temperature is imposed, so the viscosity and the thermal conductivity are constants along x.

$$k = \frac{\mu \; c_p}{Pr} \tag{8.5.2}$$

so that equation (8.5.1) becomes

$$q = -\frac{\mu \; c_p}{Pr} \left(\frac{\partial T}{\partial y} \right)_{y=0} \tag{8.5.3}$$

Below is reported the graph regarding the interaction region

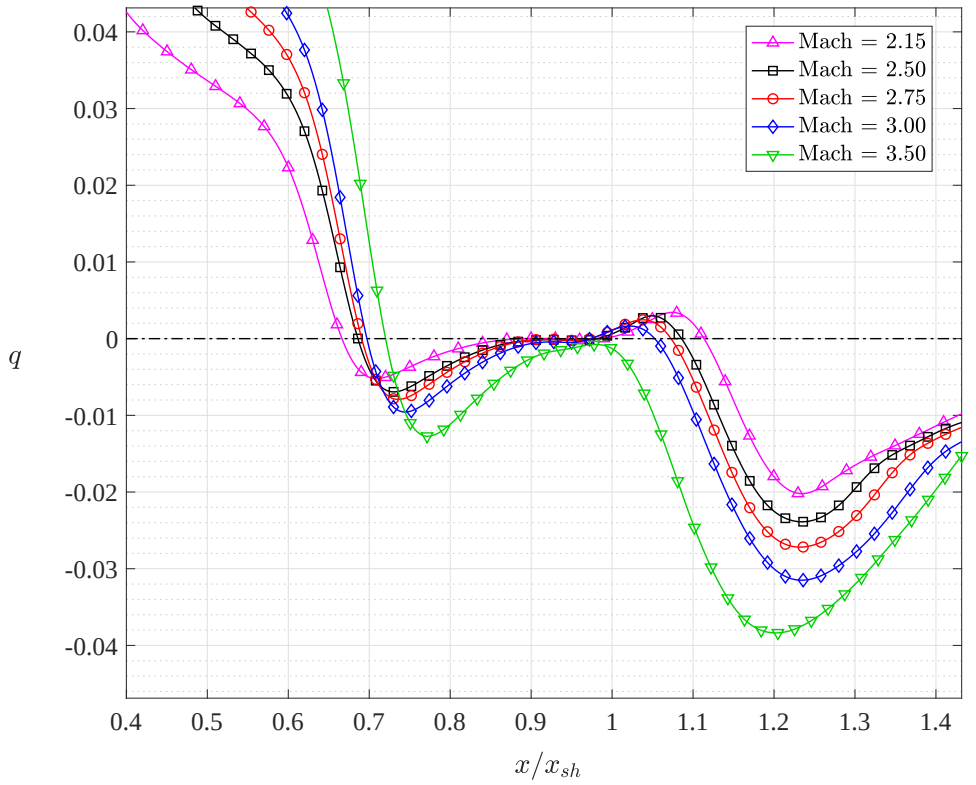

Figure 28: Heat transfer trend in the SWBLI region for different Mach numbers.

As can be seen in figure 28 the trend of the heat transfer is given by the sum of two effects: the first one is the increase of temperature of the flow due to the SWBLI and the second one is the natural reduction of the magnitude of q due to the continuous tendency of the temperature to the one of recovery causing a sort of dumping effect on the heat transfer which influence can be better visualized in the region between $x/x_{sh} \sim 0.8 \div \sim 1.1$.
As said before by this graph can be understood the entity of the increment in temperature along the plate due to the SWBLI.
The latter consists in a first heathen, caused by the first compression fan, which has a (local) maximum that increases and moves downstream as the Mach number increases, moreover there is a second (global) maximum that increases with Mach number and moves upstream the plate.
Another important consideration about the figure above is the fact that in correspondence of $x/x_{sh} \sim 0.95$ the heat transfer for some curves becomes positive. This means that downstream of the first heathen of the flow, the SWBLI causes a forced reduction in temperature and consequently the plate, which is at the temperature of recovery, returns heat to flow. In the case for $Mach = 3.5$ the cooling is not enough relatively to the first heathen to reverse the direction of the heat transfer.
Contrary to the skin friction, the effect of the SWBLI in the heat transfer is directly proportional to the Mach number since the viscosity and the energy content are also proportional to it.

9 Analysis for different wedge angles θ and fixed shock wave angle β

Another analysis that is carried out in this thesis regards the study of the different behaviours of the SWBLI having fixed the shock wave angle β and varying the inlet Mach and the wedge angle θ that generates the shock wave.
In particular $\beta = 24.07°$ is fixed which is the one corresponding to $M = 2.75$ in section 8 and then a $M = 3.00$ is chosen that implies a resulting wedge angle of $\theta = 6.167°$.

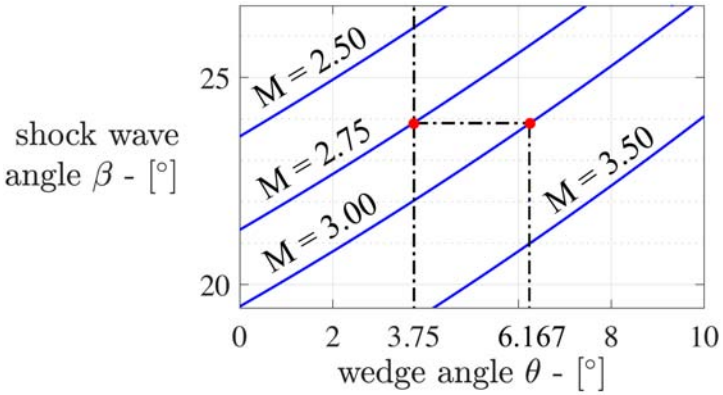

Figure 29: Portion of the $\theta - \beta - M$ graph (appendix C.1) highlighting the case studied.

The comparison in behaviour is conducted for the simulation having $M = 2.75$ of section 8 which has the β angle equal to the one assumed in this study, and the newly presented simulation having $M = 3.00$ (figure 29). Additionally the simulation having $M = 2.15$ of section 8 is taken into account since it is the one having the largest interaction region encountered so far.

Table 6: Cases taken into account in the following study.

M	wedge angle - θ	shock wave angle - β
2.15	3.75°	30.75°
2.75	3.75°	24.07°
3.00	6.167°	24.07°

Below are shown the density fields of the several cases under study in order to visualize and qualitatively compare their macroscopic behaviour. Since the normal component of the flow velocity in respect of the oblique shock wave is higher in the latter case, a more intense interaction between the shock wave and the boundary layer is expected.

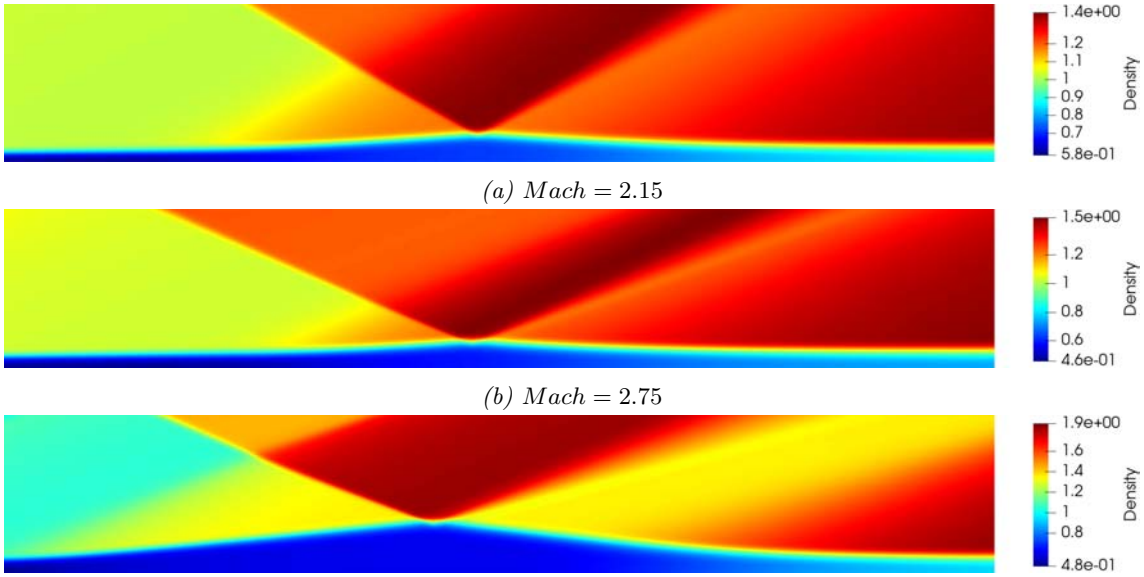

(a) $Mach = 2.15$

(b) $Mach = 2.75$

(c) $Mach = 3.00$ $(\beta_{M=2.75})$

Figure 30: Density fields for different Mach numbers.

As can be noticed the dimensions of the SWBLI in the new case (fig. 33.c) are rather larger than the other cases.
The properties studied are the pressure trend along the plate (sec. 9.1), the skin friction (sec. 9.2), the reflux field and the dimensions of the recirculation region (sec. 9.3).

9.1 Wall pressure analysis with fixed β

Here the pressure trend along the plate gets analysed.
As can be seen in figure 33 the width of the interaction region is larger than the other cases, then the first pressure rise is expected to come earlier along x.

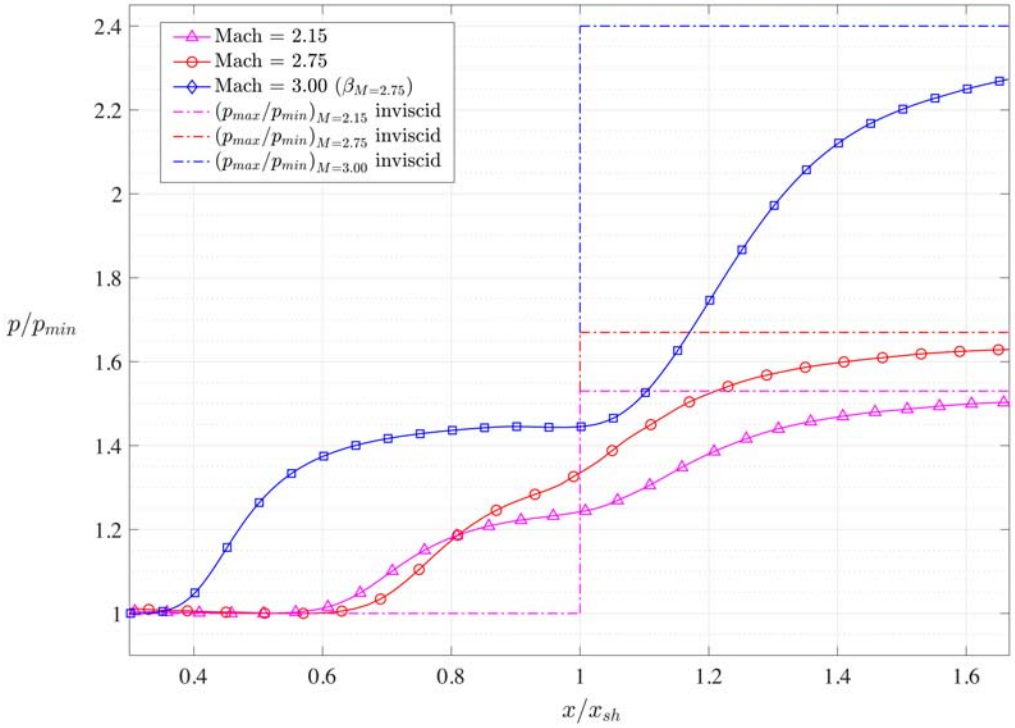

Figure 31: Wall pressure trends corresponding to different Mach numbers under study. The blue line is the one of the case added.

As can be seen in figure 31 the interaction region of the case under study (blue line) is much larger than the others, as expected.
The total rise of pressure expected by the inviscid theory of Rankine-Hugoniot (appendix C) is also higher due to the combination of a higher Mach number and a lower shock wave angle in respect of the case of fixed wedge angle of section 8.

9.2 Skin friction analysis with fixed β

In this section the skin friction trend is pointed out, leading to the knowledge of some important aspects of the SWBLI.

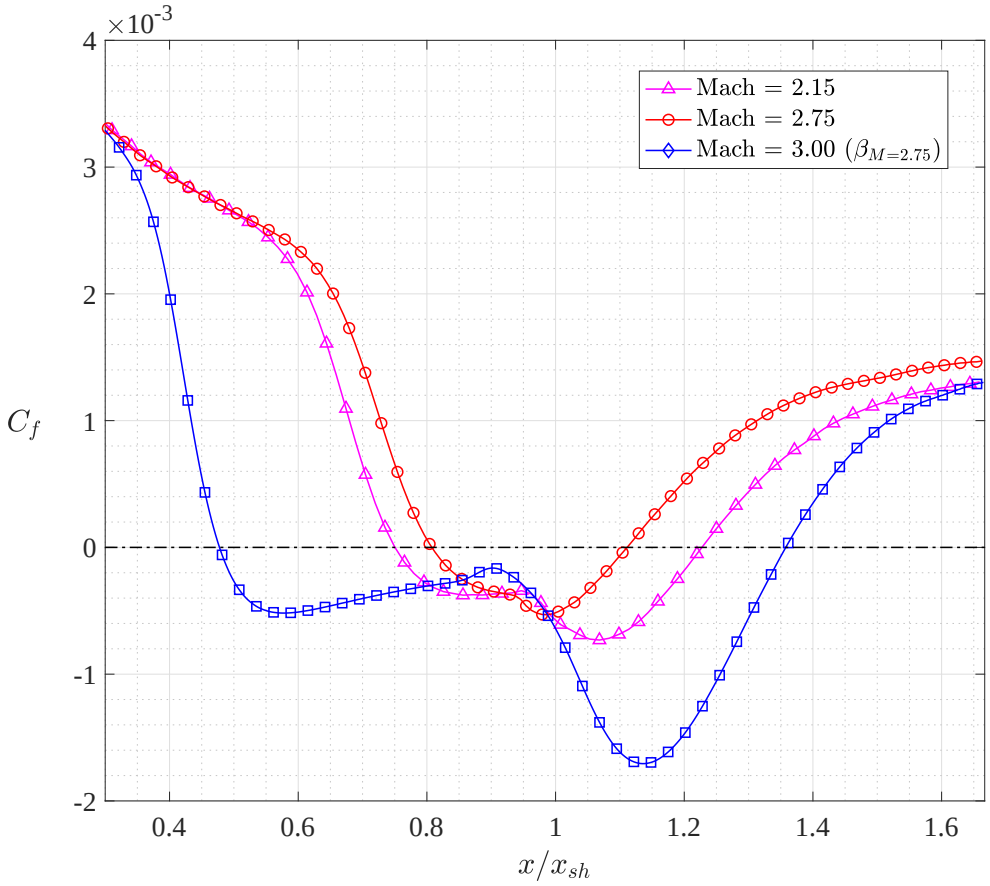

Figure 32: Skin friction trend for the cases taken into account in the present study. The blue line is the one of the case added.

As can be noticed in figure 32 the new curve corresponding to $M = 3.00$ has a recirculation region much larger and a minimum value of the skin friction way lower in line with the previsions. It can also be noticed that in the junction region downstream of the SWBLI (i.e. $x/x_{sh} >\sim 1.6$) the new case (blue line) presents a slight overshoot, that is, the boundary layer downstream of the SWBLI is thinner compared to the other cases.

In the tables below can be seen the comparison between the dimensions of the recirculating region and the minimum values of the skin friction for the different cases.

Table 7: Positions of detachment and reattachment points at various Mach numbers and width of the detached region.
(*) Mach number corresponding to $\beta_{M=2.75}$

M	x_{det}/x_{sh}	x_{reatt}/x_{sh}	$width$
2.15	0.7652	1.2349	0.4697
2.75	0.8125	1.1125	0.3
3.00*	0.4783	1.3583	0.88

Table 8: Minimum C_f *values at various Mach numbers.*
(*) Mach number corresponding to $\beta_{M=2.75}$

M	$C_{f_{min}}$
2.15	-7.3089E-04
2.75	-5.3133E-04
3.00*	-1.7058E-03

9.3 Recirculation analysis with fixed β

In this section a closer look to the recirculation region is taken.
Here the main aspects observed are the general behaviour of the reflux and the dimensions of the recirculation region.
Firstly the reflux fields are shown:

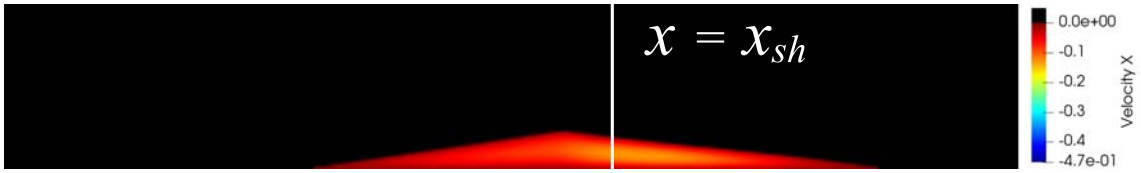

(a) $Mach = 2.15$

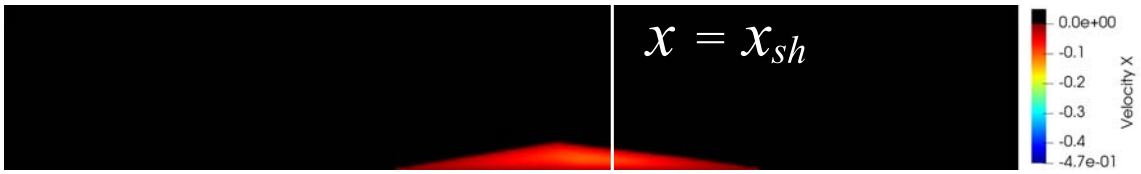

(b) $Mach = 2.75$

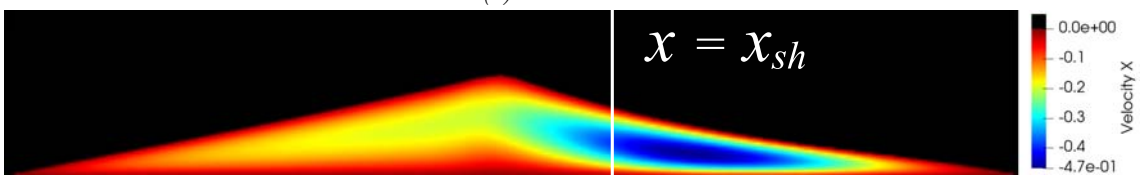

(c) $Mach = 3.00$ $(\beta_{M=2.75})$

Figure 33: Reflux fields for different Mach numbers.
In this image the fields are rescaled along x in order to better visualize the reflux behaviour.

Below are reported the dimensions of the latter recirculation regions

Table 9: Dimensions of the reflux regions of the different cases studied.
(*) Mach number corresponding to $\beta_{M=2.75}$

M	*width*	*height*
2.15	0.4697	0.0122
2.75	0.3	0.009
3.00*	0.88	0.0322

10 Summary and results

In the present thesis the study of a laminar Shock Wave Boundary Layer Interaction has been carried out.
The model used computes the adimensional Navier-Stokes equations adopting a 6th order accuracy hybrid scheme with a density gradient threshold.
Validations demonstrated that the results obtained by the solver laid within a sufficiently thin error band considering the different accuracy orders adopted in the validation models, therefore the further analysis protracted in this thesis could be considered valid.
The main aspects concerned were the pressure trend, the skin friction and the thermal stress along the wall.
The analysis of the pressure trend showed that an attenuation of the pressure of the flow reached downstream of the SWBLI occurred, caused by the upstream compression fan induced by the presence of the viscosity, and this effect was higher as the Mach number increased.
The analysis of the skin friction highlighted the effect of the intensity of the shock wave, i.e. the Mach number, in the SWBLI dimensions through the width and in the intensity of the recirculation through the $C_{f_{min}}$. That is, the SWBLI got thinner as the Mach number increased and the intensity of the recirculation got lower as well.
Further the velocity profiles of the maximum recirculation for different Mach numbers were shown in order to better compare the magnitude involved and they were coherent with the expectations given by the skin friction trend for different Mach numbers.
Then heat exchange along the SWBLI was computed. The simplifying assumptions made caused a shift of the temperature from the recovery value at the wall leading to a continuous heat transfer in background along the whole plate. Nevertheless the temperature behaviour could be appropriately described highlighting a fluctuation in the heat exchange along the SWBLI, i.e. in the temperature dynamics of the fluid, that is, a first heathen in correspondence of the compression fan occurred, followed by a cooling of the fluid across the separation, then a second heathen occurred in correspondence of the reattachment location.
The results above were obtained for a few Mach numbers: 2.15, 2.5, 2.75, 3 and 3.5. In the case of need of data for Mach numbers different than these, one can interpolate the results of this thesis in order to obtain the desired prediction of the behaviour.
At last the behaviour for a fixed shock wave angle was investigated, in particular was simulated an additional case having a $M = 3.00$ with the shock wave angle corresponding to the one with $M = 2.75$ in the previous study, i.e. the shock wave generator angle was varied from $3.75°$ to $6.167°$. This study shown an high increment in the intensity of the interaction with a larger detachment region, both in width and in height, and a stronger recirculation.

The work accomplished in this thesis allows the COMETES group of the Industrial Engineering department of the Univesity of Padova to protract the studies of the wall flows in compressible conditions, therefore further analysis regard the study of the effects on the SWBLI of a forced heathen or cooling of the flow by the plate. Besides studies on the dynamics involved by the roughness of the plate can be carried out.
Moreover the implementation of the turbulent model will be followed out, which requires the add at the inlet conditions of scattered values of the components of the properties to the mean ones, within a certain standard deviation. Since the results for the turbulent flow are rather chaotic, information about numerical instabilities cannot be distinguished from the physical solutions anymore, so an accurate laminar model must be firstly built in order to being able to determine whether the macroscopic results are established by physical behaviour or not.
Furthermore an interesting study regards the introduction of vortex generators upstream the

SWBLI, where its locations can be predicted, in order to stir some momentum into the separation region to help the reattachment of the boundary layer and to reduce the loss in efficiency. The implementations of these models are based on the *Immersed Boundary Methods* (IBMs) [10]. These methods are used to describe flows moving around complex objects allowing the employment of a Cartesian grid for the computation of the flow domain regardless the complexity of the objects involved. That means that they are simple to be realized.

A Appendix - Navier-Stokes equations

The Navier-Stokes equations are a system of equations that describe the physic of the fluids in the most general way.
This means that they find a large utility in a wide number of technological and scientific sectors, utility increased by the possibility of coupling them with the Maxwell equations allowing their application to the study of magnetohydrodynamics.
The Navier-Stokes equations are obtained by three conservation principles applied to continuum systems:

1. continuity principle (mass conservation)
2. second Newton's law (momentum conservation)
3. first law of the thermodynamics (energy conservation)

A.1 Mass conservation

Let's consider a material volume V and write the balance of mass

$$\frac{\mathrm{d}m}{\mathrm{d}t} = \frac{\mathrm{d}m_V}{\mathrm{d}t} + \phi_\rho^{\partial V} \tag{A.1.1}$$

where m is the mass enclosed in the material volume and ∂V is the frontier of the material volume. That is, the total variation of mass inside the volume is given by the sum of the variation of mass caused by the variation of the volume and the variation of mass caused by the flow of mass through the surface ∂V.
However the mass conservation principle says that

$$\frac{\mathrm{d}m}{\mathrm{d}t} = 0 \tag{A.1.2}$$

so

$$\frac{\mathrm{d}m_V}{\mathrm{d}t} = -\,\phi_\rho^{\partial V} = -\int_{\partial V} \rho\ \vec{V}\cdot\vec{n}\ \mathrm{d}S = \frac{\mathrm{d}}{\mathrm{d}t}\int_V \rho\ \mathrm{d}V \tag{A.1.3}$$

where $\vec{n}$ is the normal versor external to the volume. Let's take the last two members of (A.1.3)

$$\frac{\mathrm{d}}{\mathrm{d}t}\int_V \rho\ \mathrm{d}V = \int_{\partial V} \rho\ \vec{v}\cdot\vec{n}\ \mathrm{d}S \tag{A.1.4}$$

Since the material volume is arbitrary, it can be considered fixed in time, so the total derivative can be transported inside the integral transforming it into a partial derivative. Furthermore the Stokes' Theorem can be applied to the right side of the equation giving

$$\int_V \frac{\partial\rho}{\partial t}\ \mathrm{d}V = -\int_V \nabla\cdot(\rho\vec{v})\,\mathrm{d}V \tag{A.1.5}$$

$$\int_V \left[\frac{\partial\rho}{\partial t} + \nabla\cdot(\rho\vec{v})\right]\ \mathrm{d}V = 0 \tag{A.1.6}$$

and since V is arbitrary the integrand must be zero:

$$\frac{\partial\rho}{\partial t} + \nabla\cdot(\rho\vec{v}) = 0 \tag{A.1.7}$$

Which represents the conservative form of the continuity equation in Eulerian approach[6].

[6]The Eulerian approach consists in the observation of the particles passing through a fixed point

A.2 Momentum conservation

Let's consider the momentum balance applied to the material volume:

$$\frac{\mathrm{d}\vec{Q}}{\mathrm{d}t} = \frac{\mathrm{d}\vec{Q}_V}{\mathrm{d}t} + \phi_{\rho\vec{v}}^{\partial V} \tag{A.2.1}$$

where $\vec{Q}$ is the momentum.
That is, the total variation of momentum in the material volume V is given by the variation of momentum caused by the variation of volume summed by the variation of momentum caused by the flow of it through the frontier of the material volume ∂V.
Now

$$\frac{\mathrm{d}\vec{Q}_V}{\mathrm{d}t} = \frac{\mathrm{d}}{\mathrm{d}t}\int_V \rho\vec{v}\,\mathrm{d}V \tag{A.2.2}$$

$$\phi_{\rho\vec{v}}^{\partial V} = \int_{\partial V} \rho\vec{v}\cdot(\vec{v}\cdot\vec{n})\,\mathrm{d}S \tag{A.2.3}$$

and

$$\frac{\mathrm{d}\vec{Q}}{\mathrm{d}t} = \Sigma\vec{F} \tag{A.2.4}$$

where the resultant of forces is given by the contribute of volume forces and surface forces:

$$\Sigma\vec{F} = \int_V \mathrm{d}\vec{F}_V + \int_{\partial V} \mathrm{d}\vec{F}_S \tag{A.2.5}$$

The forces acting on the volume are:

$$\mathrm{d}\vec{F}_V = \rho\vec{f}\mathrm{d}V \tag{A.2.6}$$

where $\vec{f}$ are specific volume forces per unit of volume.
On the frontier of the material volume are acting surface forces, i.e. tensions:

$$\mathrm{d}\vec{F}_S = \vec{t}_n\mathrm{d}S \tag{A.2.7}$$

where $\vec{t}_n$ are surface forces per unit of area.
From Cauchy-Poisson's Theorem on continuum mechanics:

$$\vec{t}_n = \overline{\overline{T}}\cdot\vec{n} \tag{A.2.8}$$

where $\overline{\overline{T}}$ is the tensions tensor.
Inserting these definitions into (A.2.4) results in

$$\frac{\mathrm{d}\vec{Q}}{\mathrm{d}t} = \int_V \rho\vec{f}\,\mathrm{d}V + \int_{\partial V} \overline{\overline{T}}\cdot\vec{n}\,\mathrm{d}S \tag{A.2.9}$$

and substituting (A.2.2), (A.2.3) and (A.2.9) into (A.2.1) gives

$$\frac{\mathrm{d}}{\mathrm{d}t}\int_V \rho\vec{v}\,\mathrm{d}V = -\int_{\partial V} \rho\vec{v}\cdot(\vec{v}\cdot\vec{n})\,\mathrm{d}S + \int_V \rho\vec{f}\,\mathrm{d}V + \int_{\partial V} \overline{\overline{T}}\cdot\vec{n}\,\mathrm{d}S \tag{A.2.10}$$

As said before the material volume is arbitrary so it can be considered fixed in time and the time derivative can be put inside the integral becoming a partial derivative. Let's also apply Stokes' Theorem where possible

$$\int_V \frac{\partial(\rho\vec{v})}{\partial t}\,\mathrm{d}V = -\int_V \nabla\cdot(\rho\vec{v}\cdot\vec{v})\,\mathrm{d}V + \int_V \rho\vec{f}\,\mathrm{d}V + \int_V \nabla\cdot\overline{\overline{T}}\,\mathrm{d}V \tag{A.2.11}$$

$$\int_V \left[\frac{\partial (\rho \vec{v})}{\partial t} + \nabla \cdot (\rho \vec{v} \cdot \vec{v}) - \rho \vec{f} - \nabla \cdot \overline{\overline{T}} \right] \mathrm{d}V = 0 \tag{A.2.12}$$

For the arbitrariness of the volume the integrand must be zero:

$$\frac{\partial (\rho \vec{v})}{\partial t} + \nabla \cdot (\rho \vec{v} \cdot \vec{v}) - \rho \vec{f} - \nabla \cdot \overline{\overline{T}} = 0 \tag{A.2.13}$$

$$\frac{\partial (\rho \vec{v})}{\partial t} + \nabla \cdot (\rho \vec{v} \cdot \vec{v}) = \rho \vec{f} + \nabla \cdot \overline{\overline{T}} \tag{A.2.14}$$

which is the *motion equation of Cauchy* and represent the momentum balance.
Let's consider the case of a newtonian[7] behaviour of the fluid, the tension tensor can be expressed in terms of the type of fluid:

$$\overline{\overline{T}} = -p\overline{\overline{I}} + 2\mu\overline{\overline{E}} + \lambda (\nabla \cdot \vec{v})\, \overline{\overline{I}} \tag{A.2.15}$$

where p is the pressure, $\overline{\overline{I}}$ is the identity matrix, $\overline{\overline{E}}$ is the deformation tensor, μ is the dynamic viscosity and λ is the cinematic viscosity. That is, the tension tensor is composed by three terms: the pressure term, the dynamic viscosity term and the cinematic viscosity one. The last two of them can be collected according the Stokes' hypothesis $\lambda = -\frac{2}{3}\mu$:

$$\overline{\overline{T}} = -p\overline{\overline{I}} + \mu \left[2\overline{\overline{E}} - \frac{2}{3} (\nabla \cdot \vec{v})\, \overline{\overline{I}} \right] \tag{A.2.16}$$

in which the last term represents the *viscosity tensor* $\overline{\overline{\Phi}}$, and (A.2.16) can be written as:

$$\overline{\overline{T}} = -p\overline{\overline{I}} + \overline{\overline{\Phi}} \tag{A.2.17}$$

now substituting (A.2.17) into (A.2.14) results

$$\frac{\partial (\rho \vec{v})}{\partial t} + \nabla \cdot (\rho \vec{v} \cdot \vec{v}) = -\nabla p + \rho \vec{f} + \nabla \cdot \overline{\overline{\Phi}} \tag{A.2.18}$$

which is the conservative form of the momentum balance equation.

A.3 Energy conservation

Let's consider the balance of energy

$$\frac{\mathrm{d}\varepsilon}{\mathrm{d}t} = \frac{\mathrm{d}\varepsilon_V}{\mathrm{d}t} + \phi_\varepsilon^{\partial V} \tag{A.3.1}$$

that means that, similarly to the other balances, the variation of the total energy in the volume V is given by the variation of total energy due to the variation of volume plus the variation of total energy caused by the flow of it through the frontier of it.
Now

$$\frac{\mathrm{d}\varepsilon_V}{\mathrm{d}t} = \frac{\mathrm{d}}{\mathrm{d}t} \int_V \left(\rho e + \rho \frac{v^2}{2} \right) \mathrm{d}V \tag{A.3.2}$$

where ρe is the internal energy per unit of volume and $\rho \frac{v^2}{2}$ is the kinetic energy per unit of volume.

$$\phi_\varepsilon^{\partial V} = \int_{\partial V} \left(\rho e + \rho \frac{v^2}{2} \right) (\vec{v} \cdot \vec{n})\, \mathrm{d}S \tag{A.3.3}$$

[7] the tension which the fluid is subjected is proportional to its deformation velocity

In order to define the variation of total energy let's consider the first principle of the thermodynamics

$$\mathrm{d}\varepsilon = \mathrm{d}q + \mathrm{d}w \tag{A.3.4}$$

where ε is the total energy, q and w are respectively the heat and the work fluxes transferred by and to the system.
Since the point of interest of the Navier-Stokes equations is the dynamic of the fluid, the derivative of equation (A.3.4) is taken

$$\mathrm{d}\dot{\varepsilon} = \mathrm{d}\dot{q} + \mathrm{d}\dot{w} \tag{A.3.5}$$

Now the variation of heat exchanged is given by a volumetric contribute and a superficial one:

$$\mathrm{d}\dot{q} = \mathrm{d}\dot{q}_V + \mathrm{d}\dot{q}_S \tag{A.3.6}$$

$$\mathrm{d}\dot{q}_V = \rho\ Q\ \mathrm{d}V \tag{A.3.7}$$

where Q is the specific heat transferred per unit of volume

$$\mathrm{d}\dot{q}_S = -\vec{q}\cdot\vec{n}\ \mathrm{d}S \tag{A.3.8}$$

where $\vec{q}$ is the specific heat transferred per unit of area and it can be defined through the Fourier's law:

$$\vec{q} = -\ k\ \nabla T \tag{A.3.9}$$

where k is the thermal conductivity of the fluid which is related to the molecular viscosity by the relation

$$k = \frac{c_p \mu}{Pr} \tag{A.3.10}$$

Let's take into account the variation of forces. Similarly to the variation of heat, it is given by the sum of a volumetric term and a superficial one.

$$\mathrm{d}\dot{w}_V = \rho\ \vec{f}\cdot\vec{v}\ \mathrm{d}V \tag{A.3.11}$$

which is the power of the volume forces

$$\mathrm{d}\dot{w}_S = \vec{v}\cdot\vec{t}_n\ \mathrm{d}S = \vec{v}\cdot\overline{\overline{T}}\cdot\vec{n}\ \mathrm{d}S \tag{A.3.12}$$

That is, substituting (A.3.7), (A.3.8), (A.3.11) and (A.3.12) into (A.3.6) and inserting it into (A.3.1) together with (A.3.2) and (A.3.3) results

$$\begin{aligned}\frac{\mathrm{d}}{\mathrm{d}t}\int_V \left(\rho e + \rho\frac{v^2}{2}\right)\mathrm{d}V + \int_{\partial V}\left(\rho e + \rho\frac{v^2}{2}\right)(\vec{v}\cdot\vec{n})\,\mathrm{d}S = \\ = \int_V \rho\ Q\ \mathrm{d}V - \int_{\partial V}\vec{q}\cdot\vec{n}\ \mathrm{d}S + \int_V \rho\vec{f}\cdot\vec{n}\ \mathrm{d}V + \int_{\partial V}\vec{v}\cdot\overline{\overline{T}}\cdot\vec{n}\ \mathrm{d}S\end{aligned} \tag{A.3.13}$$

which is the integral form of the derivative of the first principle of thermodynamics that contains all of the contributes.
In order to obtaining the differential form let's apply the Stokes' theorem to surface integrals:

$$\int_V \left\{\frac{\partial}{\partial t}\left(\rho e + \rho\frac{v^2}{2}\right) + \nabla\cdot\left[\left(\rho e + \rho\frac{v^2}{2}\right)\cdot\vec{v}\right] - \rho\ Q + \nabla\cdot\vec{q} - \rho\vec{f}\cdot\vec{v} - \nabla\cdot\left(\vec{v}\cdot\overline{\overline{T}}\right)\right\}\mathrm{d}V = 0 \tag{A.3.14}$$

For the arbitrary of the material volume the integrand can be extracted

$$\frac{\partial}{\partial t}\left(\rho e+\rho\frac{v^2}{2}\right)+\nabla\cdot\left[\left(\rho e+\rho\frac{v^2}{2}\right)\cdot\vec{v}\right]=\rho\ Q-\nabla\cdot\vec{q}+\rho\vec{f}\cdot\vec{v}+\nabla\cdot\left(\vec{v}\cdot\overline{\overline{T}}\right) \tag{A.3.15}$$

which is the differential equation of the energy balance.
According to (A.2.17) let's explicit the tension tensor into the pressure and viscosity terms

$$\nabla\cdot\left(\vec{v}\cdot\overline{\overline{T}}\right)=\nabla\cdot\left[\vec{v}\cdot\left(-p\overline{\overline{I}}+\overline{\overline{\Phi}}\right)\right]=\nabla\cdot\left(-p\overline{\overline{I}}\cdot\vec{v}\right)+\nabla\cdot\left(\vec{v}\cdot\overline{\overline{\Phi}}\right)=-\nabla\cdot(p\vec{v})+\nabla\cdot\left(\vec{v}\cdot\overline{\overline{\Phi}}\right) \tag{A.3.16}$$

finally substituting (A.3.16) into (A.3.15) results

$$\frac{\partial}{\partial t}\left(\rho e+\rho\frac{v^2}{2}\right)+\nabla\cdot\left[\left(\rho e+\rho\frac{v^2}{2}\right)\cdot\vec{v}\right]=-\nabla\cdot(p\vec{v})+\rho\ Q-\nabla\cdot\vec{q}+\rho\vec{f}\cdot\vec{v}+\nabla\cdot\left(\vec{v}\cdot\overline{\overline{\Phi}}\right) \tag{A.3.17}$$

which is the energy balance equation for a generic fluid.
From this differential equation can be seen that the total energy variation has several sources:

- work of pressure forces: $-\nabla\cdot(p\vec{v})$
- rate of volumetric heating: $\rho\ Q$
- thermal flow for conduction: $-\nabla\cdot\vec{q}$
- work of mass (volume) forces: $\rho\vec{f}\cdot\vec{v}$
- work of viscous forces: $\nabla\cdot\left(\vec{v}\cdot\overline{\overline{\Phi}}\right)$

Gathering the three final equations of conservation found in the paragraphs above, the equations of Navier-Stokes for continuum systems are obtained

$$\begin{aligned}
&\frac{\partial\rho}{\partial t}+\nabla\cdot(\rho\vec{v})=0\\
&\frac{\partial(\rho\vec{v})}{\partial t}+\nabla\cdot(\rho\vec{v}\cdot\vec{v})=-\nabla p+\rho\vec{f}+\nabla\cdot\overline{\overline{\Phi}}\\
&\frac{\partial}{\partial t}\left(\rho e+\rho\frac{v^2}{2}\right)+\nabla\cdot\left[\left(\rho e+\rho\frac{v^2}{2}\right)\cdot\vec{v}\right]=-\nabla\cdot(p\vec{v})+\rho\ Q-\nabla\cdot\vec{q}+\rho\vec{f}\cdot\vec{v}+\nabla\cdot\left(\vec{v}\cdot\overline{\overline{\Phi}}\right)
\end{aligned} \tag{A.3.18}$$

This system is made of 5 equations $(1+3+1)$ in conservative formulation for compressible flows in 7 unknowns (density, three components of the velocity, internal energy, pressure and temperature).
In the two-dimensional case of the present thesis the system is made of 4 $(1+2+1)$ equations with 6 unknowns (density, two components of the velocity, internal energy, pressure and temperature). Nevertheless, the energy equation can be expressed in terms of static enthalpy instead of the internal energy.
In the present case the volume forces and the volumetric heat exchange Q are neglected, and considering a stationary regime and splitting the system in its components it becomes:

$$
\begin{aligned}
&\frac{\partial(\rho u)}{\partial x}+\frac{\partial(\rho v)}{\partial y}=0\\
&\rho u\frac{\partial u}{\partial x}+\rho v\frac{\partial u}{\partial y}=-\frac{\partial p}{\partial x}+\frac{\partial \Phi_{ii}}{\partial x}+\frac{\partial \Phi_{ij}}{\partial y}\\
&\rho u\frac{\partial v}{\partial x}+\rho v\frac{\partial v}{\partial y}=-\frac{\partial p}{\partial y}+\frac{\partial \Phi_{ji}}{\partial x}+\frac{\partial \Phi_{jj}}{\partial y}\\
&\rho u\frac{\partial h}{\partial x}+\rho v\frac{\partial h}{\partial y}=u\frac{\partial p}{\partial x}+v\frac{\partial p}{\partial y}+\frac{\partial}{\partial x}\left(\frac{\mu}{Pr}\frac{\partial h}{\partial x}\right)+\frac{\partial}{\partial y}\left(\frac{\mu}{Pr}\frac{\partial h}{\partial y}\right)+\\
&\qquad\qquad+\Phi_{ii}\frac{\partial u}{\partial x}+\Phi_{ij}\frac{\partial u}{\partial y}+\Phi_{ji}\frac{\partial v}{\partial x}+\Phi_{jj}\frac{\partial v}{\partial y}
\end{aligned}
\tag{A.3.19}
$$

The system can be written in vectorial form in order to distinguish the several terms that make up the Navier-Stokes equations

$$
\frac{\partial \vec{U}}{\partial t}=-\frac{\partial \vec{F}_i(\vec{U})}{\partial x_i}+\frac{\partial \vec{F}_{vi}(\vec{U})}{\partial x_i}+\vec{S}(\vec{U}) \tag{A.3.20}
$$

where:

- $\vec{U}$: contains the conservative variables;
- $\vec{F}_i$: contains the convective fluxes;
- $\vec{F}_{vi}$: contains the viscous fluxes;
- $\vec{S}$: contains the source terms.

The left side of eq. (A.3.20) considers the temporal variation of the conservative properties of the flow, while the right side is made up by their spatial variation and the source terms. The first one of the latter is given by two contributes: a term concerning *convective* flux and a term concerning *diffusive* flux. The first one regards the transportation of the properties driven by pressure and velocity, such as the downstream flux imposed by the inlet Mach number, the second one concerns the transportation of the properties due to the natural thermodynamic evolution of the fluid, such as the normal-stream transportation of energy in the case of heated plate.

B Appendix - Boundary layer equations

Let's consider an incompressible stationary flow. This one can be described by the *Stokes equations*:

$$\begin{aligned}
&\frac{\partial u}{\partial x}+\frac{\partial v}{\partial y}=0\\
&u\frac{\partial u}{\partial x}+v\frac{\partial u}{\partial y}=-\frac{1}{\rho}\frac{\partial p}{\partial x}+\nu\left(\frac{\partial^2 u}{\partial x^2}+\frac{\partial^2 u}{\partial y^2}\right)\\
&u\frac{\partial v}{\partial x}+v\frac{\partial v}{\partial y}=-\frac{1}{\rho}\frac{\partial p}{\partial y}+\nu\left(\frac{\partial^2 v}{\partial x^2}+\frac{\partial^2 v}{\partial y^2}\right)\\
&\rho u\frac{\partial h}{\partial x}+\rho v\frac{\partial h}{\partial y}=u\frac{\partial p}{\partial x}+v\frac{\partial p}{\partial y}+\frac{\mu}{Pr}\left(\frac{\partial^2 h}{\partial x^2}+\frac{\partial^2 h}{\partial y^2}\right)+2\mu\left[\left(\frac{\partial u}{\partial x}\right)^2+\left(\frac{\partial v}{\partial y}\right)^2+\left(\frac{\partial u}{\partial y}+\frac{\partial v}{\partial x}\right)^2\right]
\end{aligned} \tag{B.0.1}$$

Where the last one is the energy equation written in terms of static enthalpy.
Introducing the *Reynolds Number*, these equations can be non-dimensionalized obtaining:

$$\begin{aligned}
&\frac{\partial u^*}{\partial x^*}+\frac{\partial v^*}{\partial y^*}=0\\
&u^*\frac{\partial u^*}{\partial x^*}+v^*\frac{\partial u^*}{\partial y^*}=-\frac{\partial p^*}{\partial x^*}+\frac{1}{Re}\left(\frac{\partial^2 u^*}{\partial x^{*2}}+\frac{\partial^2 u^*}{\partial y^{*2}}\right)\\
&u^*\frac{\partial v^*}{\partial x^*}+v^*\frac{\partial v^*}{\partial y^*}=-\frac{\partial p^*}{\partial y^*}+\frac{1}{Re}\left(\frac{\partial^2 v^*}{\partial x^{*2}}+\frac{\partial^2 v^*}{\partial y^{*2}}\right)\\
&u^*\frac{\partial h^*}{\partial x^*}+v^*\frac{\partial h^*}{\partial y^*}=u^*\frac{\partial p^*}{\partial x^*}+v^*\frac{\partial p^*}{\partial y^*}+\frac{1}{Pr\ Re}\left(\frac{\partial^2 h^*}{\partial x^{*2}}+\frac{\partial^2 h^*}{\partial y^{*2}}\right)+\frac{2}{Re}\left[\left(\frac{\partial u^*}{\partial x^*}\right)^2+\left(\frac{\partial v^*}{\partial y^*}\right)^2+\left(\frac{\partial u^*}{\partial y^*}+\frac{\partial v^*}{\partial x^*}\right)^2\right]
\end{aligned} \tag{B.0.2}$$

where apexes (*) denote the adimensional values.
Arising the need to study the very thin region of the boundary layer it is convenient to execute a change of variables in order to stretch the coordinates inside of it.

$$x'=x^* \quad (x \text{ variable doesn't change})$$

$$y'=\frac{y}{\delta}=\frac{y}{L}\frac{L}{\delta} \quad \text{but} \quad \frac{y}{L}\doteq y^* \quad \text{and} \quad \frac{L}{\delta}\approx\frac{1}{\sqrt{Re}} \quad \text{so}$$

$$y'=y^*\sqrt{Re}, \quad dy'=\sqrt{Re}\ dy^*, \quad dy^*=\frac{dy'}{\sqrt{Re}}$$

where apexes ($'$) denote variables determined inside the boundary layer.
Applying the coordinates transformation to the Laplace equation (B.0.2.a), results

$$\frac{\partial u^*}{\partial x'}+\sqrt{Re}\ \frac{\partial v^*}{\partial y'}=0$$

which, considering very large Reynolds Numbers, in order to be satisfied must give

$$\frac{\partial u^*}{\partial x'}=\frac{\partial y^*}{\partial y'}=0$$

That means that not only the spatial parameters must be varied but also the velocities:

$$\begin{cases} u' = u^* \\ v' = v^* \sqrt{Re} \end{cases}$$

that gives

$$\frac{\partial u'}{\partial x'} + \frac{\partial v'}{\partial y'} = 0$$

Let's apply the coordinates transformation to the momentum equation along y (B.0.2.c):

$$u' \frac{\partial}{\partial x'} \left(\frac{v'}{\sqrt{Re}} \right) + \left(\frac{v'}{\sqrt{Re}} \right) \sqrt{Re} \frac{\partial}{\partial y'} \left(\frac{v'}{\sqrt{Re}} \right) = -\sqrt{Re} \frac{\partial p^*}{\partial y'} + \frac{1}{Re} \frac{\partial^2}{\partial x'^2} \left(\frac{v'}{\sqrt{Re}} \right) + \frac{1}{Re} Re \frac{\partial^2}{\partial y'^2} \left(\frac{v'}{\sqrt{Re}} \right)$$

$$\frac{1}{\sqrt{Re}} \left(u' \frac{\partial v'}{\partial x'} + v' \frac{\partial v'}{\partial y'} \right) = -\sqrt{Re} \frac{\partial p^*}{\partial y'} + \frac{1}{Re^{3/2}} \frac{\partial^2 v'}{\partial x'^2} + \frac{1}{\sqrt{Re}} \frac{\partial^2 v'}{\partial y'^2}$$

let's divide all the equation for $\sqrt{Re}$ in order to have powers of Re only in the denominator:

$$\frac{1}{\sqrt{Re}} \left(u' \frac{\partial v'}{\partial x'} + \frac{v' \partial v'}{\partial y'} \right) = -\frac{\partial p^*}{\partial y'} + \frac{1}{Re^2} \frac{\partial^2 v'}{\partial x'^2} + \frac{1}{Re} \frac{\partial^2 v'}{\partial x'^2}$$

Now for $Re \to \infty$ all terms goes to zero except for the pressure one:

$$\frac{\partial p^*}{\partial y'} = 0 \tag{B.0.3}$$

that is, inside the boundary layer for large Reynolds Numbers the pressure is constant along y coordinate: $p^* = f(x')$.
The junction condition for the pressure is

$$\lim_{y' \to \infty} p_i(x') = \lim_{y \to 0} p_e\left(x^*, y\right) = p_e^0 \tag{B.0.4}$$

where the subscripts i and e mean respectively the internal and external values to the boundary layer and the apex ^{0} is used to refer to the value on the surface.
Now let's apply the coordinates transformation to the momentum equation along x (B.0.2.b):

$$u' \frac{\partial u'}{\partial x'} + \left(\frac{v'}{\sqrt{Re}} \right) \sqrt{Re} \frac{\partial u'}{\partial y'} = -\frac{\partial p^*}{\partial x'} + \frac{1}{Re} \frac{\partial^2 u'}{\partial x'^2} + \frac{1}{Re} \; Re \; \frac{\partial^2 u'}{\partial y'^2}$$

which for large Reynolds, and substituting (B.0.4) in it, becomes

$$u' \frac{\partial u'}{\partial x'} + v' \frac{\partial u'}{\partial y'} = -\frac{\mathrm{d} p_e^0}{\mathrm{d} x'} + \frac{\partial^2 u'}{\partial y'^2}$$

where the derivative of the pressure became total since it only depends by x'.
For the energy equation let's consider

$$h' = h^*$$

then, substituting the terms and taking into account the simplifications above, results

$$x' \frac{\partial h'}{\partial x'} + v' \frac{\partial h'}{\partial y'} = u' \frac{\partial p^*}{\partial x'} + \frac{1}{Pr} \frac{\partial^2 h'}{\partial y'^2} + \left(\frac{\partial u'}{\partial y'} \right)^2$$

That is, four equations that describe the behaviour of the boundary layer were found and they are called *boundary layer equations*:

$$\begin{aligned}
&\frac{\partial u'}{\partial x'} + \frac{\partial v'}{\partial y'} = 0 \\
&\frac{\partial p^*}{\partial y'} = 0 \\
&u' \frac{\partial u'}{\partial x'} + v' \frac{\partial u'}{\partial y'} = -\frac{\mathrm{d}p_e^0}{\mathrm{d}x'} + \frac{\partial^2 u'}{\partial y'^2} \\
&x' \frac{\partial h'}{\partial x'} + v' \frac{\partial h'}{\partial y'} = u' \frac{\partial p^*}{\partial x'} + \frac{1}{Pr} \frac{\partial^2 h'}{\partial y'^2} + \left(\frac{\partial u'}{\partial y'} \right)^2
\end{aligned} \tag{B.0.5}$$

These equations lend two boundary conditions for the u' component of the flow:

$$\begin{cases}
u'(x', y = 0) = 0 \quad \text{(adherence condition)} \\
\lim\limits_{y' \to \infty} u' = \lim\limits_{y \to 0} U_\infty \quad \text{(junction condition)}
\end{cases}$$

and one boundary condition for the v' component of the flow:

$$v'(x', y' \to 0) = 0 \quad \text{(impermeability condition)}$$

C Appendix - Rankine-Hugoniot equations

The Rankine-Hugoniot equations are relations that describe the variation of the properties of the flow when it crosses a shock wave.
These equations are valid for the normal shock wave but their validity can be extended to the oblique shock wave considering the components of the vectorial properties of the flow normal to it, i.e. the velocity and Mach Number.
Let's consider a stationary shock wave crossed normally by a flow having velocity $\vec{v_1} = \{u_1, 0, 0\}$, pressure p_1, density ρ_1, temperature T_1 and enthalpy h_1 as can be seen in figure 34.
The properties of the flow once it has crossed the shock wave are $\vec{v_2} = \{u_2, 0, 0\}$, p_2, ρ_2, T_2 and h_2. Let's take a closed control surface containing the shock wave.

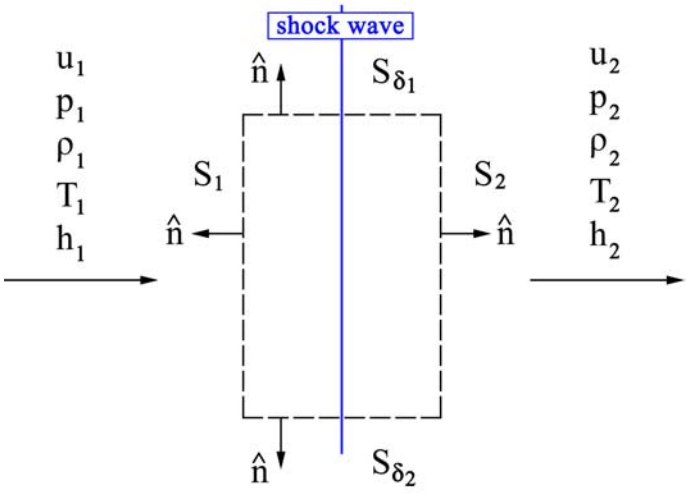

Figure 34: Scheme for the variation of the flow properties across a normal shock wave. $\widehat{n}$ is the vector pointing out of the closed control surface.

Consider the process adiabatic, stationary and the viscous effects to be negligible on the surfaces S_1, S_2 and S_δ.
Then let's integrate the motion equations (2.1.4) on the control surface.

$$\int_V \nabla \cdot (\rho \vec{v}) \, \mathrm{d}V = \int_{S_1 \cup S_2 \cup S_\delta} \rho \, (\vec{v} \cdot \vec{n}) \, \mathrm{d}S \tag{C.0.1}$$

where V is the volume contained in the closed control surface and n is the normal versor of the local surface considered.
Solving the integral results in

$$-\rho_1 u_1 S_1 + \rho_2 u_2 S_2 + 0 = 0 \tag{C.0.2}$$

but $S_1 = S_2$ so

$$\rho_1 u_1 = \rho_2 u_2 \tag{C.0.3}$$

Let's take into account the momentum equation which can be written as

$$\nabla \cdot (\rho \vec{v} \cdot \vec{v}) = -\nabla \cdot \left(p \overline{\overline{I}}\right) + \nabla \cdot \overline{\overline{\Phi}} \tag{C.0.4}$$

integrated becomes

$$\int_{S_1 \cup S_2 \cup S_\delta} \rho \vec{v} \left(\vec{v} \cdot \vec{n} \right) \mathrm{d}S + \int_{S_1 \cup S_2 \cup S_\delta} p \overline{\overline{I}} \cdot \vec{n} \, \mathrm{d}S = \int_{S_1 \cup S_2 \cup S_\delta} \overline{\overline{\Phi}} \cdot \vec{n} \, \mathrm{d}S \tag{C.0.5}$$

where the right side of the equal can be neglected and the equation becomes

$$\rho_1 u_1 \left(-u_1 \right) S_1 + \rho_2 u_2 u_2 s_2 - p_1 S_1 + p_2 S_2 = 0 \tag{C.0.6}$$

which leads to

$$\rho_1 u_1^2 + p_1 = \rho_2 u_2^2 + p_2 \tag{C.0.7}$$

Finally since the flow is adiabatic, the conservation of the total enthalpy is valid

$$h_{0,1} = h_{0,2} \tag{C.0.8}$$

$$h_1 + \frac{u_1^2}{2} = h_2 + \frac{u_2^2}{2} \tag{C.0.9}$$

Equations (C.0.3), (C.0.7) and (C.0.9) are the *Rankine-Hugoniot equations* or *jump equations* of a normal shock wave.
Using this formulation some useful relations can be obtained in order to explicitly describe the properties downstream of the shock wave.
These equations are

$$\frac{\rho_2}{\rho_1} = \frac{\left(\gamma + 1 \right) M_1^2}{2 + \left(\gamma - 1 \right) M_1^2} \tag{C.0.10}$$

$$\frac{p_2}{p_1} = 1 + \frac{2\gamma}{\gamma + 1} \left(M_1^2 - 1 \right) \tag{C.0.11}$$

$$\frac{T_2}{T_1} = \left[1 + \frac{2\gamma}{\gamma + 1} \left(M_1^2 - 1 \right) \right] \frac{2 + \left(\gamma - 1 \right) M_1^2}{\left(\gamma + 1 \right) M_1^2} \tag{C.0.12}$$

$$\frac{M_2}{M_1} = \frac{1}{M_1} \left[\frac{2 + \left(\gamma - 1 \right) M_1^2}{2\gamma M_1^2 - \left(\gamma - 1 \right)} \right]^{1/2} \tag{C.0.13}$$

Equations (C.0.3), (C.0.7) and (C.0.9) become valid for an oblique shock when the parallel component of the velocity to the shock wave gets considered.
Its equation is

$$w_1 = w_2 \tag{C.0.14}$$

The *normal Mach Number* to the shock wave is defined as

$$M_{n1} = \frac{u_1}{a_1} = \frac{\mid \vec{v_1} \mid sin\beta}{a_1} = M_1 sin\beta \tag{C.0.15}$$

where β is the angle between the shock wave and the direction of the flow.
By substituting M_{n1} instead of M_1 into the Rankine-Hugoniot equations, the system that describes the jump of the properties across the oblique shock wave is obtained.

C.1 $\theta - \beta - M$ relation

An important relationship regarding oblique shock waves is the $\theta - \beta - M$ relation. The components of this relation are:

- θ: the angle of the oblique shock generator (wedge)
- β: the angle of the oblique shock wave
- *Mach*: the incident Mach Number

and it allows to determine one of the three components knowing the other two of them. Using equation (C.0.15) the equation that can be obtained is

$$\tan\theta = 2\ \mathrm{cotan}\beta \frac{M_1^2 \sin^2\beta - 1}{M_1^2\left[\gamma + \cos\left(2\beta\right)\right] + 2} \tag{C.1.1}$$

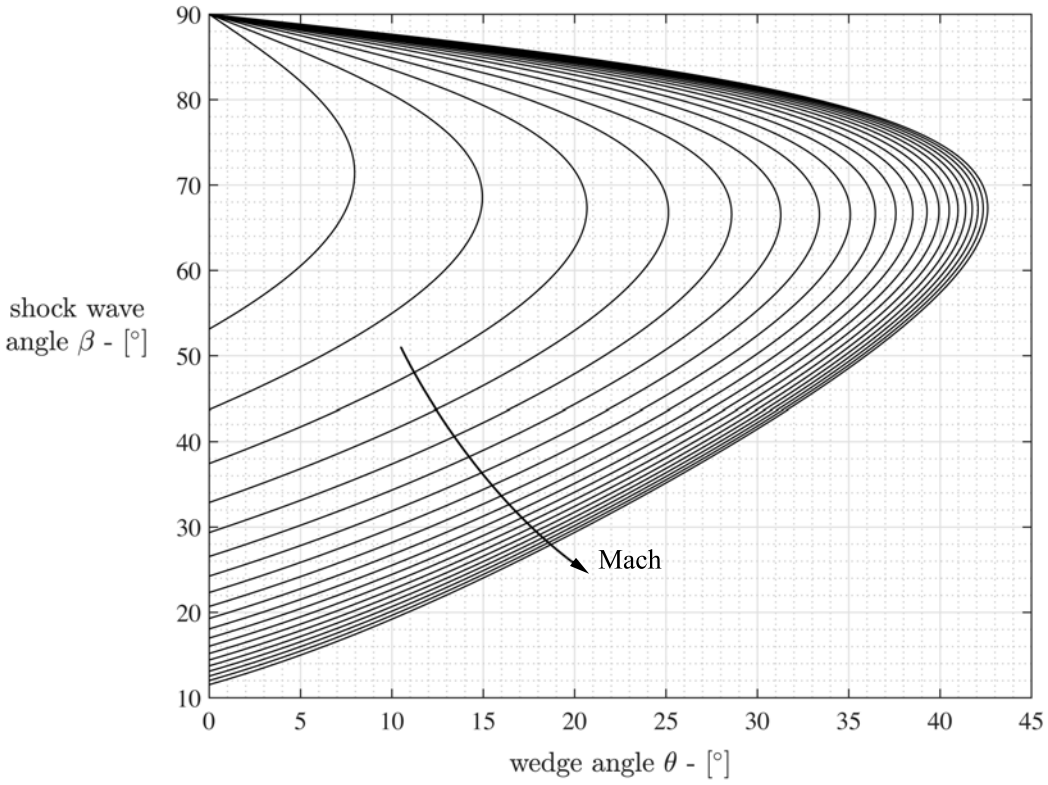

Figure 35: Curves for oblique shock wave angles, in function of the wedge angle, generated by different Mach numbers.

This graph shows that for a fixed Mach number and for a fixed wedge angle, β has two distinct solutions. The maximum value of θ for a fixed upstream Mach number is the one at which the shock wave is still oblique and a higher Mach number will make the shock wave to become a *detached bow shock*. In particular the shock wave having for solution a β angle above θ_{max} is conventionally considered a *strong shock wave*, the one having a solution below θ_{max} is considered a *weak shock wave*.
Generally flows evolve giving a weak solution as in the case of this thesis, so higher Mach numbers give weaker shock waves.

Bibliography

[1] J. D. Anderson. *Fundamentals of Aerodynamics — Fifth edition*, volume 116. 2012.

[2] D. M. Bushnell, A. M. Cary, and J. E. Harris. Calculation Methods for Compressible Turbulent Boundary Layers-1976. 2019.

[3] M. Castro, B. Costa, and W. S. Don. High order weighted essentially non-oscillatory WENO-Z schemes for hyperbolic conservation laws. *Journal of Computational Physics*, 230(5):1766–1792, 2011.

[4] D. R. Chapman and M. W. Rubesin. Temperature and Velocity Profiles in the Compressible Laminar Boundary Layer with Arbitrary Distribution of Surface Temperature. *Journal of the Aeronautical Sciences*, 16(9):547–565, 1949.

[5] Y. Cho and A. Aessopos. Similarity transformation methods in the analysis of the two dimensional steady compressible laminar boundary layer. *Compressible Fluid Dynamics*, (1), 2004.

[6] W. F. Cope and D. R. Hartree. The Laminar Boundary Layer in Compressible Flow. *Advances in Applied Mechanics*, 2(C):21–92, 1951.

[7] R. Courant, K. Friedrichs, and H. Lewy. Über die nichtlinearen Wellengleichungen der mathematischen Physik. *Mathematische Annalen*, 100(2):32–74, 1928.

[8] J. E. Danberg. Scientific and technical information. *Soviet Materials Science*, 11(1):124–126, 1976.

[9] N. De Tullio, P. Paredes, N. D. Sandham, and V. Theofilis. Laminar-turbulent transition induced by a discrete roughness element in a supersonic boundary layer. *Journal of Fluid Mechanics*, 735:613–646, 2013.

[10] F. De Vanna. *A high-resolution fully compressible Navier-Stokes solver for analysis of moving objects at high Mach numbers*. PhD thesis, Università degli Studi di Padova, 2019.

[11] G. Degrez, C. H. Boccadoro, and J. F. Wendt. The interaction of an oblique shock wave with a laminar boundary layer revisited. An experimental and numerical study. *Journal of Fluid Mechanics*, 177(4):247–263, 1987.

[12] S. Gottlieb and C. W. Shu. Total variation diminishing Runge-Kutta schemes. *Mathematics of Computation of the American Mathematical Society*, 67(221):73–85, 1998.

[13] I. Greber, R. J. Hakkinen, and L. Trilling. Laminar boundary layer oblique shock wave interaction on flat and curved plates. *ZAMP Zeitschrift für Angewandte Mathematik und Physik*, 9(5-6):312–331, 1958.

[14] A. Grébert, J. Bodart, S. Jamme, and L. Joly. Simulations of shock wave/turbulent boundary layer interaction with upstream micro vortex generators. *International Journal of Heat and Fluid Flow*, 72(March):73–85, 2018.

[15] E. Hairer and G. Wanner. Runge-Kutta Methods, Explicit, Implicit. *Encyclopedia of Applied and Computational Mathematics*, (January 2015), 2015.

[16] R. J. Hakkinen, I. Greber, L. Trilling, and S. S. Abarbanel. The Interaction of an Oblique Shock Wave with a Laminar Boundary Layer. Technical report, 1959.

[17] L. Howarth. On the Solution of the Laminar Boundary Layer Equations. *Journal of the Physical Society of Japan*, 4(3):149–154, 1949.

[18] P. G. Huang and G. N. Coleman. Van driest transformation and compressible wall-bounded flows. *AIAA Journal*, 32(10):2110–2113, 1994.

[19] E. Katzert. On the lengthscales of laminar shock/boundary-layer interaction. *Journal of Fluid Mechanics*, 206:477–496, 1989.

[20] C. A. Kennedy and A. Gruber. Reduced aliasing formulations of the convective terms within the Navier-Stokes equations for a compressible fluid. *Journal of Computational Physics*, 227(3):1676–1700, 2008.

[21] G. Kuerti. The Laminar Boundary Layer Equations. *The Mathematical Gazette*, 48(366):470, 1964.

[22] A. Lerat and C. Corre. A Residual-Based Compact Scheme for the Compressible Navier-Stokes Equations. *Journal of Computational Physics*, 170(2):642–675, 2001.

[23] C. Messe. A modified van Driest method for compressible and supersonic channel flows and pipe flows. *53rd AIAA/SAE/ASEE Joint Propulsion Conference, 2017*, (July), 2017.

[24] P. Orlandi, S. Pirozzoli, and M. Bernardini. DNS of laminar-turbulent boundary layer transition induced by solid obstacles. 2015.

[25] S. Parveen. Numerical solution of non linear differential equation by using shooting techniques. *International Journal of Mathematics And its Applications*, 4(1):93–100, 2016.

[26] V. Pasquariello, S. Hickel, and N. A. Adams. Unsteady effects of strong shock-wave/boundary-layer interaction at high Reynolds number. *Journal of Fluid Mechanics*, 823:617–657, 2017.

[27] S. Pirozzoli. Conservative hybrid compact-WENO schemes for shock-turbulence interaction. *Journal of Computational Physics*, 178(1):81–117, 2002.

[28] S. Pirozzoli. Generalized conservative approximations of split convective derivative operators. *Journal of Computational Physics*, 229(19):7180–7190, 2010.

[29] S. Pirozzoli. Numerical Methods for High-Speed Flows. *Annual Review of Fluid Mechanics*, 43(1):163–194, 2011.

[30] S. Pirozzoli and M. Bernardini. Direct Numerical Simulation Database for Impinging Shock Wave/Turbulent Boundary-Layer Interaction, 2011.

[31] S. Pirozzoli and M. Bernardini. Direct numerical simulation database for impinging shock wave/turbulent boundary-layer interaction. *AIAA Journal*, 49(6):1307–1312, 2011.

[32] S. Pirozzoli and M. Bernardini. Turbulence in supersonic boundary layers at moderate Reynolds number. *Journal of Fluid Mechanics*, 688:120–168, 2011.

[33] S. Pirozzoli, M. Bernardini, and F. Grasso. Direct numerical simulation of transonic shock-/boundary layer interaction under conditions of incipient separation. *Journal of Fluid Mechanics*, 657:361–393, 2010.

[34] S. Pirozzoli, F. Grasso, and T. B. Gatski. Direct numerical simulation and analysis of a spatially evolving supersonic turbulent boundary layer at M = 2.25. *Physics of Fluids*, 16(3):530–545, 2004.

[35] T. J. Poinsot and S. K. Lele. Boundary Conditions for Direct Simulations of Compressible Viscous Flows, 1992.

[36] R. F. Qiu, Y. C. You, C. X. Zhu, and R. Q. Chen. Lattice Boltzmann simulation for high-speed compressible viscous flows with a boundary layer. *Applied Mathematical Modelling*, 48:567–583, 2017.

[37] A. Quarteroni and A. Valli. *Numerical Approximation of Partial Differential Equations.*, volume 50. 1988.

[38] F. Salvadore, M. Bernardini, and M. Botti. GPU accelerated flow solver for direct numerical simulation of turbulent flows. *Journal of Computational Physics*, 235:129–142, 2013.

[39] J. Sivasubramanian and H. F. Fasel. Numerical investigation of shock-induced laminar separation bubble in supersonic flows. *45th AIAA Fluid Dynamics Conference*, pages 1–36, 2015.

[40] A. J. Smits. Viscous Flows and Turbulence. page 432, 2010.

[41] E. Süli. Numerical solution of ordinary differential equations using mathematical software. *Advances in Intelligent Systems and Computing*, 285:213–226, 2014.

[42] K. W. Thompson. Time dependent boundary conditions for hyperbolic systems. *Journal of Computational Physics*, 68(1):1–24, 1987.

[43] A. Trettel. *Velocity Transformation for Compressible Wall Turbulence with Heat Transfer*. PhD thesis, University of Maryland, 2015.

[44] E. R. Van Driest. Turbulent Boundary Layer in Compressible Fluids. *Journal of the Aeronautical Sciences*, 18(3):145–216, 1951.

[45] B. W. Van Oudheusden. Compressibility effects on the extended crocco relation and the thermal recovery factor in laminar boundary layer flow. *Journal of Fluids Engineering, Transactions of the ASME*, 126(1):32–41, 2004.

[46] P. S. Volpiani, J. Larsson, and M. Bernardini. Investigating the effects of non-adiabatic walls on shock/boundary-layer interaction at low reynolds number using direct numerical simulations. *AIAA Aerospace Sciences Meeting, 2018*, (210059):1–13, 2018.

[47] F. M. White. *Viscous Fluid Flow*, volume 14. McGraw-Hill, 2nd edition, 1991.

[48] Y. S. Zhang, W. T. Bi, F. Hussain, and Z. She. A generalized Reynolds analogy for compressible wall-bounded turbulent flows. *Journal of Fluid Mechanics*, 739:392–420, 2013.

Acknowledgements

Concerning the accomplishment of this thesis I thank my advisor for this opportunity and for the advises he gave me. Moreover I'd like to thank my co-advisor for his endurance and kindness in assisting me and supporting me all along this work. People talented and kindhearted like them are hard to be found.

The acknowledgements of a Master of Science thesis are not related only to the thesis itself, but they are also an occasion to thank all the people who contributed in the candidate's path.
Therefore I'd like to thank my father, *Stefano*, for always being there every time I needed support and my mother, *Elisa*, for her love and always being caring.
I thank my girlfriend, *Martina*, who sustained me in the hard moments and helped me to grow more than I ever did before.
I thank my university colleagues and friends, *Matteo*, *Annalisa*, *Marco Z.*, *Marco P.*, *Giorgia*, *Riccardo C.*, *Riccardo I.*, *Marinella* and *Andrea*, for gifting me with their sympathy and friendship and for accepting me in the best group ever.
Lastly I thank all the fantastic people I met during these years and the experiences that I shared with each of them.
I will keep all the memories of this adventure forever inside my mind, and heart.
L.S.